Tunable Morphology of Porous Polymers via Polymerization–Induced Microphase Separation

A DISSERTATION
SUBMITTED TO THE FACULTY OF
UNIVERSITY OF MINNESOTA
BY

Stacey Alexandra Saba

IN PARTIAL FULFILLMENT OF THE REQUIREMENTS
FOR THE DEGREE OF
DOCTOR OF PHILOSOPHY

Marc A. Hillmyer, Advisor

August, 2017

Acknowledgements

My time in graduate school and the work in this thesis has been greatly strengthened by many people who have generously shared their time, expertise, and friendship with me. First, I would like to thank my advisor, Marc Hillmyer, as this work would not have been possible without his patience, guidance, and scientific insight. Marc is an excellent professional, and his passion for science is evident. Working in his group has allowed me to grow as both a scientist and a person, and I appreciate having the freedom to pursue projects that have interested me.

I have had the opportunity to collaborate with some excellent researchers over the past few years, and I would like to thank them for all that they taught me. Professor Myungeun Seo and Jongmin Park provided new perspectives on porous polymers. Professor Phil Bühlmann, Dr. Maral Mousavi, and Evan Anderson instigated all of the electrochemical experiments and provided new directions and opportunities for applications of porous polymers.

The Polymer Group at the University of Minnesota is really a unique and wonderful culture of researchers and I've appreciated learning from many of you. There are a number of past and present Hillmyer group members that have supported and encouraged me over the years and have made working in the lab a truly enjoyable experience. I am thankful for your mentorship, patience training me in the lab, thoughtful research discussions, experimental assistance, or feedback on this thesis, and I'm happy to

additionally consider many of you as friends: Sujay Chopade, Guilhem De Hoe, Paula Delgado, David Goldfeld, Nick Hampu, Jon Hollinger, Bongjoon Lee, Mike Larsen, Dylan Loomis, Henry Martinez, Angelika Neitzel, Colin Peterson, Madalyn Radlauer, Debbie Schneiderman, Morgan Schulze, Ingrid Haugan Smidt, Alex Todd, Yihui Xie, Thomas Vidil, Annabelle Watts, and Yanzhao Wang. Our group softball team, first Soft Matter Batters and then Sexy and Sustainable, has been a great way to get to know the rest of the group outside of the lab and has been a lot of fun.

I'd also like to thank Julie Prince and Teresa Bredahl for keeping everything running smoothly, and the CEMS department for supporting Women's Group which has provided an indispensable support system over the years. I've made a number of good friends during my time here, and have enjoyed our camping trips, board games, or just hanging out: Cha-Jung Chen, Tom Fielitz, Seyoung Jung, Bob Lade, Camille Malonzo May, Alyssa McKenna, Nick Petkovich, Ami Zachar, Michael Zachar. Thanks for also being there when things were difficult.

I finally want to thank my parents and sister for their love, support, and encouragement. You have made all of this possible.

Dedication

To my family.

Abstract

Nanoporous polymers are useful materials for applications in separations, catalysis, and templating. The ability to synthesize nanoporous polymers with a good control over pore size and chemistry is highly desirable. This dissertation investigates routes to tuning the morphology and pore wall chemistry of nanoporous polymers produced via polymerization-induced microphase separation (PIMS) of a growing block polymer. The PIMS processes is a facile route to synthesizing a bicontinuous microphase-separated block polymer. Selective etching of one of the blocks renders the material mesoporous (pore size 2 – 50 nm). Chapter 1 gives an overview of this process, as well as an analogous process, polymerization-induced phase separation (PIPS), which is frequently used to produce macroporous polymers (pore size > 50 nm) via phase separation of a nonreactive component. Chapter 2 describes the experimental synthetic and characterization techniques that are relevant to nanoporous polymers. Chapter 3 describes the production of a hierarchically porous polymer, which has two discrete pore sizes, by combining the PIMS and PIPS processes. Importantly, a high degree of control over porosity is attained. Chapter 4 explores this idea more thoroughly, and shows how sample composition can be used to transition from a morphology that is controlled by PIMS to one that is controlled by PIPS. Chapter 5 focusses on PIMS, and demonstrates a new approach to the preparation of disordered tricontinuous polymers with two different pore wall functionalities.

Table of Contents

List of Tables

List of Figures

List of Abbreviations

α	$\alpha = M_{w,PLA\text{-}OH}/M_{w,PLA\text{-}CTA}$
AIBN	azobisisobutyronitrile
BET	Brunauer-Emmett-Teller
BHT	butylated hydroxy toluene
BJH	Barret, Joyner, and Halenda
$CDCl_3$	deuterated chloroform
CTA	chain-transfer agent
DBU	1,8-Diazabicyclo[5.4.0]undec-7-ene
DCM	dichloromethane
DMTA	dynamic mechanical thermal analysis
DSC	differential scanning calorimetry
DVB	divinylbenzene
emf	electromotive force
FTIR	Fourier transform infrared
HCl	hydrochloric acid
IPA	2-propanol
LS	light scattering
M	monomer
M_n	number-averaged molar mass
M_w	mass-averaged molar mass
NMR	nuclear magnetic resonance
PDMA	poly(dimethylacrylamide)
PDVB	poly(divinylbenzene)
PEO	poly(ethylene oxide)
PI	poly(isoprene)
PIMS	polymerization-induced microphase separation
PLA	poly(lactide)
PIPS	polymerization-induced phase separation
PS	poly(styrene)
QSDFT	quenched solid density functional theory
RAFT	reversible addition-fragmentation chain transfer
r_H	$r_H = w_{PLA\text{-}OH}/(w_{PLA\text{-}OH} + w_{PLA\text{-}CTA})$
RI	refractive index
ROMP	ring-opening metathesis polymerization
S	styrene
SAXS	small-angle X-ray scattering
SEC	size exclusion chromatography
SEM	scanning electron microscopy
TEM	transmission electron microscopy
TGA	thermal gravimetric analysis
THF	tetrahydrofuran
T_g	glass transition temperature

Chapter 1. Introduction

Many aspects of modern society rely on polymers. From applications in healthcare to packaging to transportation, polymers are ubiquitous. In addition to these more tangible applications, the self-assembly of polymers on the nanometer length scale allows implementation in nanotechnology. For example, many nanostructured materials can be rendered nanoporous and are used in separations,[1–4] catalysis,[5–7] templating,[8–11] and electrochemistry.[12] While there are a vast selection of materials and techniques to form nanoporous materials, the fabrication of nanoporous materials from a nanostructured block polymer precursor is particularly attractive because of the wide range of synthetically accessible chemical functionalities. Furthermore, the preparation of nanoporous materials derived from polymers permits processing at relatively low temperatures compared to inorganic materials, which is appealing due to the lower energy input requirements. At the same time, good control over pore size in nanoporous polymers is readily achieved.

Nanoporous polymers can be prepared in one of two geometries: thin films and monoliths. In the former, a thin layer of the polymer of interest lies on top of a mechanical support layer. Such materials are often applied in ultrafiltration separations.[3,13,14] The latter, which will be the focus of this thesis, is a rigid, free standing material which has the advantage of not requiring a secondary support layer. Monoliths are easily prepared from a phase separation process (Section 1.1)[15–18] or from a nanostructured block polymer precursor (Sections 1.2 and 1.3).[19–22] Both approaches have

advantages and limitations, and a combination of the two methods inspired the work presented in Chapters 3 and 4, whereas Chapter 5 focuses only on nanostructured block polymer precursors. The synthetic and characterization techniques that were used are common to all the work, and are described in Chapter 2.

1.1 Polymerization-Induced Phase Separation

Polymerization-induced phase separation (PIPS) is an attractive and well-established strategy for the preparation of nanoporous polymer monoliths from a variety of monomers. As the name suggests, the nanostructures produced via PIPS arise from the phase separation of a growing polymer chain from a nonreactive porogen or diluent.[15] The porogen is chosen such that it is a good solvent for the monomers but a non-solvent for the resulting cross-linked polymer.[16] Usually the porogen is a small molecule or solvent, but can also be a nonreactive polymer or surfactant.[23] Initially, the nonreactive porogen is dissolved in a multifunctional (cross-linkable) monomer mixture, forming a homogeneous solution. Copolymerization of the monomers, typically via a thermally initiated process, affords a cross-linked polymer which phase separates from the nonreactive porogen.[16] Importantly, both the cross-linked polymer and the porogen form continuous domains, yielding a cocontinuous structure, over a wide range of compositions.[24] Removal of the porogen, through washing or drying, results in a porous structure where the polymer phase is an inter-adhered globular morphology (Figure 1.1). The globules arise as insoluble nuclei that coalesce as the polymerization proceeds, and the regions between the globules form the pores. Thermodynamically, the driving force

for phase separation is dictated by the chemical identity and relative volume fractions of the components. Kinetically, the onset of gelation of the cross-linked network, which prevents further growth of the phase separated domains, dictates the characteristic length scale of the structure.[16]

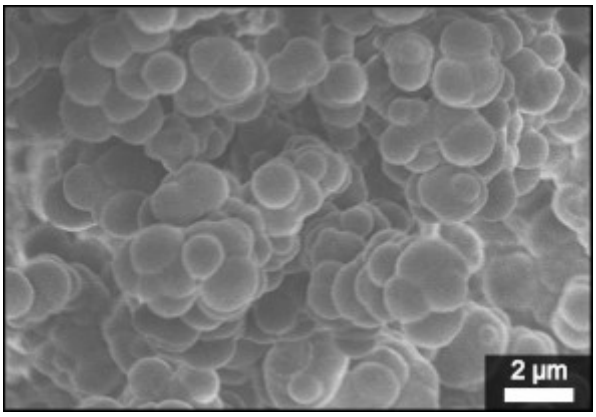

Figure 1.1. SEM micrograph of a cross-linked monolith prepared via PIPS. Styrene and divinylbenzene monomers were copolymerized in the presence of dodecanol as the porogen according to a literature procedure.[17]

Changing the identity of the porogen, cross-linker content, and reaction temperature allows for the tuning of porosity from microporous (pore size < 2 nm) to macroporous (pore size > 50 nm) in a straightforward route.[17] Notably, changing the porogen can result in profoundly different porous properties while maintaining the chemical composition of the resulting polymer monolith. This permits structure-property-performance studies that isolate the effects of pore size from monolith chemistry. Though the total pore volume of the monolith is dictated by the volume fraction of the porogen in the initial reaction mixture, and void fractions of 60 – 80 vol% are routinely obtained, the average pore size depends on the onset of phase separation of the polymer from the solvent. An earlier onset of phase separation results in larger pores, which was experimentally demonstrated

in systematic studies.[16,24,25] Increasing the monofunctional:multifunctional monomer ratio also leads to larger pore sizes.[17,25] With less cross-linker present the onset of phase separation is delayed, however during the initial stages of the polymerization the forming nuclei swell with monomer and coalesce, which ultimately produces larger insoluble globules and voids. Lastly, adjusting the polymerization temperature changes the polymerization kinetics and subsequent monolith morphology. At lower temperatures, the polymerization rate decreases which allows the monomers to preferentially segregate into the growing polymer phase.[26] This disparity in local monomer concentration facilitates polymerization in the forming polymer globules and results in larger pores.[17] The morphology of the polymer monoliths prepared via PIPS is characterized in the dry state by scanning electron microscopy (SEM), nitrogen sorption analysis (for pores < 100 nm), and mercury intrusion porosimetry (for pores sizes in the nanometer to tens of micrometer range).

Literature examples of monoliths prepared via PIPS largely focus on thermally initiated free radical polymerizations of a monofunctional vinyl monomer with a difunctional vinyl cross-linker and use a solvent as the nonreactive porogen.[27–30] Many of the commercially available monomers and porogens are summarized in a review,[16] and often divinylbenzene is the cross-linker for styrenic monomers while ethylene dimethacrylate is used as the cross-linker for acrylate- or methacrylate-based monomers. One major limitation of PIPS is inhomogeneity and broad pore size distributions that can occur, especially when free radical polymerizations are employed.[31,32] As an alternative to free

radical polymerizations, ring-opening metathesis polymerizations (ROMP)[18,33,34] and, more recently, controlled radical polymerizations[23,35–40] have been developed for the preparation of porous polymer monoliths. Importantly, many of the monomers that are used in controlled radical polymerizations have also been studied under free radical polymerizations, permitting a direct comparison of the monolith properties.

Technologically, including a few commercial examples, PIPS has been most widely employed to produce macroporous polymer monoliths for "flow-through" applications in solution where the solvent or mobile phase flows through the pores of the monolith.[41] This utilizes one major advantage of a monolith over the traditional packed bed: by flowing through the monolith – rather than around the beads – mass transport is generally faster because it is primarily convective.[42] Macroporous PIPS monoliths have been widely applied as the stationary phase in chromatography,[15,16,26] as reactors and supports for organic synthesis,[43–45] and in microfluidic devices.[46,47] In these applications, the monoliths impart the desired chemical selectivity or functionality. Further opportunities in this area include the development of synthetic techniques to better control the pore structure over multiple length scales, as well as precisely tune surface chemistry for more diverse technological applications.[40]

1.2 Ordered Etchable Block Polymers

Block polymers, which are comprised of two or more covalently connected, chemically distinct blocks, have been widely utilized as precursors for the generation of mesoporous

(pore size 2 – 50 nm) materials as they afford versatility in chemical functionality and ultimately produce materials with narrow pore size distributions. When the chemical identity and degree of polymerization of each block are appropriately chosen, the block polymer will microphase separate into ordered morphologies with compositional heterogeneities on the nanometer length scale. In the simplest case, that of an AB diblock, the thermodynamic equilibrium morphologies have been well described, and the identity of the dispersed and continuous (matrix) phases can be adjusted through changes in the relative volume fractions of the blocks.[48] In a typical case the principal domain spacing of the self-assembled block polymer structure is between 10 and 50 nm, which is a highly relevant length scale for applications in nanotechnology.

To produce nanoporous materials from a self-assembled block polymer precursor, the self-assembly must result in a morphology in which both blocks are accessible. In other words, the dispersed microphase must be continuous and susceptible to selective etching, whether via a chemical reagent or thermal or photodegradation process. In the case of the AB diblock, this requires that the obtained morphology is either gyroid or hexagonally packed cylinders with macroscopic alignment. Targeting a specific morphology often requires careful synthesis, as these morphologies are only observed over a limited range of compositions. Additionally, attaining long-range order of hexagonally packed cylinders, especially in monolithic form, often requires optimization of post-synthetic processing steps.[3,19] Without this, monoliths prepared from hexagonally packed cylinders suffer from dead end pores at grain boundaries which limits the utility of these materials.

Alternatively, networked structures have domains that percolate in three dimensions and are less likely to suffer from dead ends at grain boundaries. Beyond the simple diblock case, triblock polymers can form a number of multiply continuous structures, i.e. structures that have multiple domains that percolate continuously in space. A full description of the ordered multiply continuous network structures is outside the scope of this thesis, but these interesting materials may play a role in emerging technologies requiring orthogonal properties, e.g. mechanical toughness and mass transport, and are nicely summarized in a review.[49]

Another important consideration for the preparation of nanoporous materials from block polymers is the mechanical stability of the matrix after etching of the dispersed microphase. Ultimately, the elastic modulus of the matrix dictates the ability to retain porosity. If the modulus is too low, Laplace pressure-induced pore collapse typically occurs.[50] Although some porosity may be retained, this can decrease the specific density of the pores and limit the use of the nanoporous polymer in applications. Generally, pore collapse is circumvented by using a high glass transition ($T_g > T_{application}$) polymer as the matrix or through the introduction of cross-links, either post-polymerization or in situ.[51] Small-angle X-ray scattering (SAXS) is a crucial technique for structure determination of ordered block polymers, and comparison of SAXS patterns before and after etching can provide confirmation of matrix integrity.

Over the past few decades, several advances in polymer synthesis have been applied to produce ordered nanoporous polymers with a variety of chemical functionalities. Nanoporous materials with functional pore walls have been synthesized from blends of diblock polymers[52–54] as well as from multiblock polymers.[55–57] For the former, in the simplest case an AB diblock is blended with an AC diblock, where B and C are two miscible polymers that form a composite domain in a matrix of A. For the latter, in the case of an ABC triblock, B and C are chosen to form a core-shell structure in a matrix of A. In both cases, the blocks are chosen such that A provides mechanical stability, B provides functionality, and C is selectively etchable. Etching of C leaves B lining the pore walls of the matrix (Figure 1.2). In these materials, the pore size is readily tuned by changes in the molar mass of the etchable block and pore wall functionality is tailored through the chemistry of the matrix block. Furthermore, a variety of selective etching techniques for different polymers have been demonstrated in both thin film and bulk materials and there are many opportunities for varying the chemistry of both the matrix and pore walls.[58–63] A key aspect of selective etching is that the matrix block is unaffected; it cannot swell or dissolve if chemical etching is used and should remain below its T_g if thermal degradation is employed. Importantly, these synthetic and etching strategies are directly applicable to the preparation of nanoporous materials from disordered microphase-separated block polymer precursors.

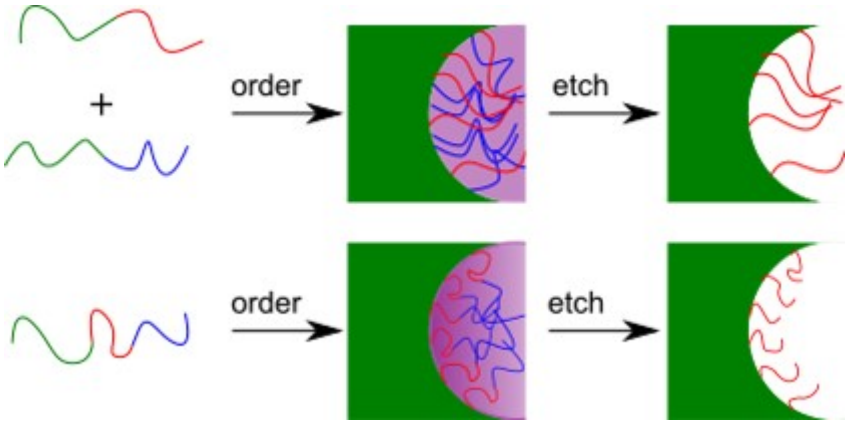

Figure 1.2. Cartoon of the preparation of nanoporous polymers with functional pore walls from polymer blends (top) and multiblocks (bottom).

1.3 Disordered Etchable Block Polymers and Polymerization-Induced Microphase Separation

Disordered microphase-separated block polymers offer the advantages of retaining orthogonal properties in a single material without the processing steps associated with obtaining an ordered microstructure. The domain spacing, and ultimately mesopore size and pore wall chemistry, is again tunable through variations in the composition of the block polymer. These disordered microphase-separated morphologies are typically bicontinuous, thus grain boundaries and dead end domains are not a concern, and selective etching of one domain results in a three-dimensional percolating mesopore network. Commonly, the bicontinuous morphology is attained in the solid state by cross-linking the matrix block which kinetically traps the disordered microphase-separated structure, preventing coarsening into an ordered microphase.[64] Cross-linking provides the additional advantage of improved thermal and mechanical stability compared to the non-cross-linked counterparts. It may also provide some chemical resistance, as cross-linked

networks only swell but do not dissolve in solvent; however, if the network swells appreciably the pores will still collapse upon drying.

One strategy to synthesize disordered nanoporous polymers uses reactive preformed block polymers that are cross-linked via post-polymerization modification. The block polymer architecture is chosen such that it microphase separates, and the block that will form the matrix contains cross-linkable moieties while the other block is selectively etchable. Importantly, the cross-linkable moieties must remain intact during the polymerization of the block polymer and the cross-linking reaction must not affect the block polymer morphology. There are a few examples of cross-linking and etching of disordered microphase-separated polymers and include direct cross-linking of the matrix monomer, e.g. poly(styrene) using UV radiation,[65] or the copolymerization of a mixture of monomers where one is cross-linked, e.g. poly(*p*-norbornenylethylstyrene-*stat*-styrene) using ROMP.[66,67] Common cross-linking strategies are nicely summarized in the literature, and typically include concentrated solution-based reactions in bulk materials or UV or ozone treatments for thin films.[64] While most of the post-polymerization cross-linking reactions described have been demonstrated on ordered microstructures, the approaches are also applicable to disordered microstructures.[64]

The production of disordered nanoporous polymers may be completed in fewer steps, with the polymerization-induced microphase separation (PIMS) process.[22] In PIMS, the cross-linking occurs concurrently with block polymer formation, unlike the post-

polymerization cross-linking described earlier. Specifically, PIMS uses a macro-chain transfer agent (macro-CTA) for the reversible addition-fragmentation chain transfer (RAFT) polymerization of multifunctional monomers. Initially, the macro-CTA is soluble in the monomers, forming a homogeneous solution. As the monomers copolymerize from the macro-CTA, the growing block polymer microphase separates and in situ cross-linking arrests the structure. By preventing structural coarsening into an ordered microphase, a bicontinuous morphology is obtained. In order to achieve this bicontinuous structure, relatively pure microphase-separated domains need to be formed prior to network gelation.

Over the past few years, PIMS has been optimized to produce both nanoporous[22,68–72] and dense bulk materials[73–76] with interesting properties. With few exceptions,[72] these works have made use of the thermal copolymerization of styrene (S) and divinylbenzene (DVB) from various macro-CTAs, that in a general sense result in a block polymer of the structure (macro-CTA)-*block*-poly(styrene-*co*-divinylbenzene), (macro-CTA)-*b*-P(S-*co*-DVB). For the preparation of nanoporous polymers, the use of poly(lactide)-CTA (PLA-CTA) is a natural choice for a macro-CTA as it readily undergoes hydrolytic etching in solutions of aqueous base while the P(S-*co*-DVB) block provides mechanical rigidity and is unaffected during etching. The first report of the PIMS process demonstrated the preparation of mesoporous polymers, an example of which is shown in Figure 1.3.[22] In the SEM micrograph, the dark regions correspond to the mesopores and the gray regions are the P(S-*co*-DVB) matrix. It is apparent that overall the structure is disordered, and the

length scale of the features (ca. 10 nm) is much smaller than in PIPS monolith (Figure 1.1, ca. 1 μm). In a later work, the effects of varying PIMS reaction mixture composition on bulk properties was thoroughly investigated.[71] In general, with all else constant, increasing PLA molar mass results in larger domains and larger pore sizes, where the mesopore size is tunable in the nanometer range. Similarly, increasing the S:DVB ratio allows for the formation of larger domains prior to network gelation and produces larger pore sizes after etching. These results were confirmed by SAXS and nitrogen sorption analysis, which provide complementary information on bulk structure.[22,71] The synthesis was further stream-lined to prepare both the PLA and P(S-*co*-DVB) blocks in one step from a heterofunctional initiator, however, unlike the earlier work this preparation requires a drybox and was not used for the preparation of materials in this thesis.[68]

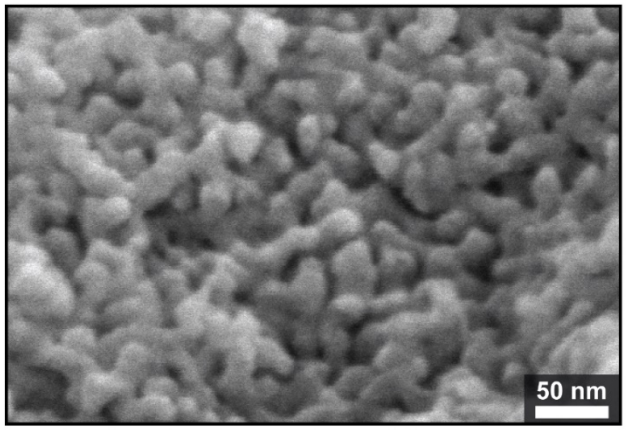

Figure 1.3. SEM micrograph of a mesoporous monolith prepared via PIMS after PLA etching showing the disordered nanostructure.

Many opportunities remain to further develop the PIMS process and broaden its scope, a few of which include: the control of porosity over multiple length scales, tuning of pore wall functionality, and process optimization for technological applications. The first

point, controlling porosity over multiple length scales, is of interest for technological applications when both high surface areas and rapid mass transport are desired.[77] Materials with two discrete pore size distributions, where the smaller pores reside in a framework of interconnected larger pores, are referred to as hierarchically porous. In these hierarchically porous structures, the smaller pores primarily contribute to the surface area of the material and may serve as the catalytic sites or selective sites, if the application is catalysis or separations, respectively. The larger pores provide enhanced mass transport through the monolith.[77] Previously, PIMS was combined with hypercross-linking to prepare hierarchically micro- and mesoporous polymers by replacing styrene with 4-vinylbenzyl chloride and, notably, good control over the mesopore size distributions was retained.[69] Furthermore, these materials exhibited accelerated nitrogen adsorption rates compared to the microporous analogues.[69] Another example of hierarchically micro- and mesoporous polymers, again with good control over mesoporosity, was demonstrated by replacing styrene with substituted styrenes in the PIMS process.[70] The bulky substituents resulted in intrinsic microporosity in the cross-linked matrix, while again the PLA domains controlled the mesoporosity.[70]

Although hierarchically micro- and mesoporous monoliths are useful for gas uptake or separations, for size exclusion aqueous separations where the monolith is the selective layer, hierarchical meso- and macroporosity is desirable.[28,78] However, conventionally, the monoliths used in these applications have been prepared by the PIPS process via free radical polymerizations, which leads to broad mesopore size distributions and ultimately

limits widespread application.[28,78] Good control over mesoporosity in a hierarchically meso- and macroporous material can be attained with a block polymer precursor, but examples have generally been limited to thin films.[79] Thus, opportunities remain to develop hierarchically meso- and macroporous polymer monoliths with good control over the mesopore structure, and in Chapters 3 and 4 we show how the PIMS process is developed to achieve these morphologies.

The second point, tuning pore wall functionality, has been well established in ordered nanoporous polymers (Section 1.2) where the presence of distinct functional groups on the pore walls has been used to target specific applications in aqueous solution, e.g. pH-responsive pore walls for drug delivery[80] or filtration.[4,81–83] Similarly, tuning the pore wall chemistry of monoliths prepared via PIMS is of interest as it could potentially broaden the scope of applications of the monoliths. In the materials described thus far, PLA etching results in a carboxylic acid on the pore wall.[22] The ability to tune pore wall chemistry could affect the monolith response to external stimuli, e.g. the introduction of pH responsive functional groups to the pore walls could be used to impart an additional level of chemical selectivity. Synthetic approaches to monoliths prepared by PIMS with different pore walls chemistries are discussed in Chapter 5 and Appendix A. The third point, process optimization could open many opportunities in technological applications. Processing has been well optimized for the macroporous monoliths prepared via PIPS for the flow-through applications described earlier. In PIMS, as the copolymerization of the monomers is done in the bulk and the resulting solids are insoluble, the monolith obtains

the shape of the vial or mold that the polymerization is conducted in. To fully take advantage of this, monoliths synthesized via PIMS should be prepared directly in the final form necessary for applications, much like the monoliths prepared via PIPS. This has not yet been fully demonstrated, as early works prepared bulk monoliths in glass vials and then sanded and milled the monoliths to the desired size (e.g. a disc) for testing.[22,73] More recently, monoliths have been prepared as thick films of several square centimeters area and tunable thickness (on the order of hundreds of micrometers), which eliminates the sanding step but still requires cutting to the desired geometry.[76] Progress towards process optimization and applications testing is described in Appendix B.

1.4 Thesis Overview

Because of its universal relevance herein, the next chapter (Chapter 2) details the experimental techniques, data processing, and data interpretation that is used throughout this thesis. Following this, the remaining chapters and the appendix cover the development of nanoporous materials via PIMS and PIPS, with an in depth study of the tunable porosity and morphology. The original motivation for this work was to prepare porous polymer monoliths with good control over porosity on multiple length scales for potential applications as the selective layer for separations of aqueous solutions. Chapter 3 describes the development of these hierarchically porous polymer monoliths, by combining controlled PIPS and PIMS. Next, Chapter 4 provides a thorough investigation into the morphology of the system, and identifies the transition from a structure that is dominated by PIMS to one that is dominated by PIPS. In Chapter 5 a new approach to

creating tricontinuous polymer monoliths via PIMS is described. Finally, the Appendix describes preliminary results of other syntheses and attempts toward technological applications of the nanoporous monoliths, as well as an outlook on ongoing work.

1.5 References

1) Phillip, W. A.; Dorin, R. M.; Werner, J.; Hoek, E. M. V; Wiesner, U.; Elimelech, M. Tuning Structure and Properties of Graded Triblock Terpolymer-Based Mesoporous and Hybrid Films. *Nano Lett.* **2011**, *11*, 2892–2900.

2) Morris, R. E.; Wheatley, P. S. Gas Storage in Nanoporous Materials. *Angew. Chemie - Int. Ed.* **2008**, *47*, 4966–4981.

3) Jackson, E. A.; Lee, Y.; Hillmyer, M. A. ABAC Tetrablock Terpolymers for Tough Nanoporous Filtration Membranes. *Macromolecules* **2013**, *46*, 1484–1491.

4) Xie, Y.; Moreno, N.; Calo, V. M.; Cheng, H.; Hong, P.-Y.; Sougrat, R.; Behzad, A. R.; Tayouo, R.; Nunes, S. P. Synthesis of Highly Porous Poly(*tert*-butyl acrylate)-*b*-polysulfone-*b*-poly(*tert*-butyl acrylate) Asymmetric Membranes. *Polym. Chem.* **2016**, *7*, 3076–3089.

5) Ottens, M.; Leene, G.; Beenackers, A. A. C. M.; Cameron, N.; Sherrington, D. C. PolyHipe: A New Polymeric Support for Heterogeneous Catalytic Reactions: Kinetics of Hydration of Cyclohexene in Two- and Three-Phase Systems over a Strongly Acidic Sulfonated PolyHipe. *Ind. Eng. Chem. Res.* **2000**, *39*, 259–266.

6) Bronstein, L. M.; Goerigk, G.; Kostylev, M.; Pink, M.; Khotina, I. A.; Valetsky, P. M.; Matveeva, V. G.; Sulman, E. M.; Sulman, M. G.; Bykov, A. V.; Lakina, N.V; Spontak, R.J. Structure and Catalytic Properties of Pt-Modified Hyper-Cross-Linked Polystyrene Exhibiting Hierarchical Porosity. *J. Phys. Chem. B* **2004**, *108*, 18234–18242.

7) Jalal, T.; Bettahalli, N. M. S.; Le, N. L.; Nunes, S. P. Hydrophobic Hyflon AD/PVDF Membranes for Butanol Dehydration via Pervaporation. *Ind. Eng. Chem. Res.* **2015**, *54*, 11180–11187.

8) Werner, J. G.; Scherer, M. R. J.; Steiner, U.; Wiesner, U. Gyroidal Mesoporous Multifunctional Nanocomposites via Atomic Layer Deposition. *Nanoscale* **2014**, *6*, 8736–8742.

9) Zhao, H.; Gu, W.; Sterner, E.; Russell, T. P.; Coughlin, E. B.; Theato, P. Highly Ordered Nanoporous Thin Films from Photocleavable Block Copolymers. *Macromolecules* **2011**, *44*, 6433–6440.

10) Jones, B. H.; Lodge, T. P. Nanocasting Nanoporous Inorganic and Organic Materials from Polymeric Bicontinuous Microemulsion Templates. *Polym. J.* **2012**, *44*, 131–146.

11) Olson, D. A.; Chen, L.; Hillmyer, M. A. Templating Nanoporous Polymers with Ordered Block Copolymers. *Chem. Mater.* **2008**, *20*, 869–890.

12) Mousavi, M. P. S.; Bühlmann, P. Reference Electrodes with Salt Bridges Contained in Nanoporous Glass: An Underappreciated Source of Error. *Anal. Chem.* **2013**, *85*, 8895–8901.

13) Phillip, W. A.; O'Neill, B.; Rodwogin, M.; Hillmyer, M. A.; Cussler, E. L. Self-Assembled Block Copolymer Thin Films as Water Filtration Membranes. *ACS Appl. Mater. Interfaces* **2010**, *2*, 847–853.

14) Yang, S. Y.; Ryu, I.; Kim, H. Y.; Kim, J. K.; Jang, S. K.; Russell, T. P. Nanoporous Membranes with Ultrahigh Selectivity and Flux for the Filtration of Viruses. *Adv. Mater.* **2006**, *18*, 709–712.

15) Svec, F.; Fréchet, J. M. J. Continuous Rods of Macroporous Polymer as High-Performance Liquid Chromatography Separation Media. *Anal. Chem.* **1992**, *64*, 820–822.

16) Svec, F. Porous Polymer Monoliths: Amazingly Wide Variety of Techniques Enabling Their Preparation. *J. Chromatogr. A* **2010**, *1217*, 902–924.

17) Viklund, C.; Svec, F.; Fréchet, J. M. J.; Irgum, K. Monolithic, "Molded", Porous Materials with High Flow Characteristics for Separations, Catalysis, or Solid-Phase Chemistry: Control of Porous Properties during Polymerization. *Chem. Mater.* **1996**, *8*, 744–750.

18) Sinner, F.; Buchmeiser, M. R. A New Class of Continuous Polymer Supports Prepared by Ring-Opening Metathesis Polymerization: A Straightforward Route to Functionalized Monoliths. *Macromolecules* **2000**, *33*, 5777–5786.

19) Chen, L.; Hillmyer, M. A. Mechanically and Thermally Robust Ordered Nanoporous Monoliths Using Norbornene-Functional Block Polymers. *Macromolecules* **2009**, *42*, 4237–4243.

20) Pitet, L. M.; Amendt, M. A.; Hillmyer, M. A. Nanoporous Linear Polyethylene from a Block Polymer Precursor. *J. Am. Chem. Soc.* **2010**, *132*, 8230–8231.

21) Mao, H.; Hillmyer, M. A. Macroscopic Samples of Polystyrene with Ordered Three-Dimensional Nanochannels. *Soft Matter* **2006**, *2*, 57–59.

22) Seo, M.; Hillmyer, M. A. Reticulated Nanoporous Polymers by Controlled Polymerization-Induced Microphase Separation. *Science.* **2012**, *336*, 1422–1425.

23) Kanamori, K.; Hasegawa, J.; Nakanishi, K.; Hanada, T. Facile Synthesis of Macroporous Cross-Linked Methacrylate Gels by Atom Transfer Radical Polymerization. *Macromolecules* **2008**, *41*, 7186–7193.

24) Peters, E. C.; Svec, F.; Fréchet, J. M. J.; Viklund, C.; Irgum, K. Control of Porous Properties and Surface Chemistry in "Molded" Porous Polymer Monoliths Prepared by Polymerization in the Presence of TEMPO. *Macromolecules* **1999**, *32*, 6377–6379.

25) Santora, B. P.; Gagne, M. R.; Moloy, K. G.; Radu, N. S. Porogen and Cross-Linking Effects on the Surface Area, Pore Volume Distribution, and Morphology of Macroporous Polymers Obtained by Bulk Polymerization. *Macromolecules* **2001**, *34*, 658–661.

26) Nischang, I.; Teasdale, I.; Brüggemann, O. Porous Polymer Monoliths for Small Molecule Separations: Advancements and Limitations. *Anal. Bioanal. Chem.* **2011**, *400*, 2289–2304.

27) Svec, F. Recent Developments in the Field of Monolithic Stationary Phases for Capillary Electrochromatography. *J. Sep. Sci.* **2005**, *28*, 729–745.

28) Urban, J.; Jandera, P.; Schoenmakers, P. Preparation of Monolithic Columns with Target Mesopore-Size Distribution for Potential Use in Size-Exclusion Chromatography. *J. Chromatogr. A* **2007**, *1150*, 279–289.

29) Peterson, D. S.; Rohr, T.; Svec, F.; Fréchet, J. M. J. Enzymatic Microreactor-on-a-Chip: Protein Mapping Using Trypsin Immobilized on Porous Polymer Monoliths Molded in Channels of Microfluidic Devices. *Anal. Chem.* **2002**, *74*, 4081–4088.

30) Svec, F.; Fréchet, J. M. J. Kinetic Control of Pore Formation in Macroporous Polymers. Formation of "Molded" Porous Materials with High Flow Characteristics for Separations or Catalysis. *Chem. Mater.* **1995**, *7*, 707–715.

31) Nischang, I.; Brüggemann, O. On the Separation of Small Molecules by Means of Nano-Liquid Chromatography with Methacrylate-Based Macroporous Polymer Monoliths. *J. Chromatogr. A* **2010**, *1217*, 5389–5397.

32) Laher, M.; Causon, T. J.; Buchberger, W.; Hild, S.; Nischang, I. Assessing the Nanoscale Structure and Mechanical Properties of Polymer Monoliths Used for Chromatography. *Anal. Chem.* **2013**, *85*, 5645–5649.

33) Eder, K.; Huber, C. G.; Buchmeiser, M. R. Surface-Functionalized, Ring-Opening Metathesis Polymerization-Derived Monoliths for Anion-Exchange Chromatography. *Macromol. Rapid Commun.* **2007**, *28*, 2029–2032.

34) Bandari, R.; Kuballa, J.; Buchmeiser, M. R. Ring-Opening Metathesis Polymerization-Derived, Lectin-Functionalized Monolithic Supports for Affinity Separation of Glycoproteins. *J. Sep. Sci.* **2013**, *36*, 1169–1175.

35) Saban, M. D.; Georges, M. K.; Veregin, R. P. N.; Hamer, G. K. H.; Kazmaier, P. M. Nitroxide-Mediated Free Radical Polymerization of Styrene. Absence of the Gel Effect. *Macromolecules* **1995**, *28*, 7032–7034.

36) Hawker, C. J. "Living" Free Radical Polymerization: A Unique Technique for the Preparation of Controlled Macromolecular Architectures. *Acc. Chem. Res.* **1997**, *4842*, 373–382.

37) Hasegawa, J.; Kanamori, K.; Nakanishi, K.; Hanada, T.; Yamago, S. Pore Formation in Poly(divinylbenzene) Networks Derived from Organotellurium-Mediated Living Radical Polymerization. *Macromolecules* **2009**, *42*, 1270–1277.

38) Turson, M.; Zhou, M.; Jiang, P.; Dong, X. Monolithic Poly(ethylhexyl methacrylate-*co*-ethylene dimethacrylate) Column with Restricted Access Layers Prepared via Reversible Addition-Fragmentation Chain Transfer Polymerization. *J. Sep. Sci.* **2011**, *34*, 127–134.

39) Li, X.; Zhou, M.; Turson, M.; Lin, S.; Jiang, P.; Dong, X. Preparation of Clenbuterol Imprinted Monolithic Polymer with Hydrophilic Outer Layers by Reversible Addition-Fragmentation Chain Transfer Polymerization and Its Application in the Clenbuterol Determination from Human Serum by On-Line Solid-Phase Extractio. *Analyst* **2013**, *138*, 3066–3074.

40) Barlow, K. J.; Hao, X.; Hughes, T. C.; Hutt, O. E.; Polyzos, A.; Turner, K. A.; Moad, G. Porous, Functional, Poly(styrene-*co*-divinylbenzene) Monoliths by RAFT Polymerization. *Polym. Chem.* **2014**, *5*, 722–732.

41) Hjertén, S.; Liao, J.-L.; Zhang, R. High-Performance Liquid Chromatography on Continuous Polymer Beds. *J. Chromatogr.* **1989**, *473*, 273–275.

42) Xie, S.; Allington, R. W.; Fréchet, J. M. J.; Svec, F. Porous Polymer Monoliths: An Alternative to Classical Beads. *Adv. Biochem. Eng. Biotechnol.* **2002**, *76*, 87–125.

43) Bayer, E. Towards the Chemical Synthesis of Proteins. *Angew. Chemie* **1991**, *30*, 113–129.

44) Brown, J. F.; Krajnc, P.; Cameron, N. R. PolyHIPE Supports in Batch and Flow-Through Suzuki Cross-Coupling Reactions. *Ind. Eng. Chem. Res.* **2005**, *44*, 8565–8572.

45) Petro, M.; Svec, F.; Fréchet, J. M. J. Immobilization of Trypsin onto "Molded" Macroporous Poly(glycidyl methacrylate-*co*-ethylene dimethacrylate) Rods and Use of the Conjugates as Bioreactors and for Affinity Chromatography. *Biotechnol. Bioeng.* **1996**, *49*, 355–363.

46) Gömann, A.; Deverell, J. A.; Munting, K. F.; Jones, R. C.; Rodemann, T.; Canty, A. J.; Smith, J. A.; Guijt, R. M. Palladium-Mediated Organic Synthesis Using Porous Polymer Monolith Formed In Situ as a Continuous Catalyst Support Structure for Application in Microfluidic Devices. *Tetrahedron* **2009**, *65*, 1450–1454.

47) Yu, C.; Davey, M. H.; Svec, F.; Fréchet, J. M. Monolithic Porous Polymer for On-Chip Solid-Phase Extraction and Preconcentration Prepared by Photoinitiated *in situ* Polymerization within a Microfluidic Device. *Anal. Chem.* **2001**, *73*, 5088–5096.

48) Bates, F. S.; Fredrickson, G. H. Block Copolymer Thermodynamics: Theory and Experiment. *Annu. Rev. Phys. Chem.* **1990**, *41*, 525–557.

49) Meuler, A. J.; Hillmyer, M. A.; Bates, F. S. Ordered Network Mesostructures in Block Polymer Materials. *Macromolecules* **2009**, *42*, 7221–7250.

50) Hillmyer, M. A. Nanoporous Materials from Block Copolymer Precursors. *Adv. Polym. Sci.* **2005**, *190*, 137–181.

51) Cavicchi, K. A.; Zalusky, A. S.; Hillmyer, M. A.; Lodge, T. P. An Ordered Nanoporous Monolith from an Elastomeric Crosslinked Block Copolymer Precursor. *Macromol. Rapid Commun.* **2004**, *25*, 704–709.

52) Mao, H.; Hillmyer, M. A. Morphological Behavior of Polystyrene-*block*-Polylactide/Polystyrene-*block*-Poly(ethylene oxide) Blends. *Macromol. Chem. Phys.* **2008**, *209*, 1647–1656.

53) Mao, H.; Arrechea, P. L.; Bailey, T. S.; Johnson, B. J. S.; Hillmyer, M. A. Control of Pore Hydrophilicity in Ordered Nanoporous Polystyrene Using an AB/AC Block Copolymer Blending Strategy. *Faraday Discuss.* **2005**, *128*, 149–162.

54) Kato, T.; Hillmyer, M. A. Functionalized Nanoporous Polyethylene Derived from Miscible Block Polymer Blends. *ACS Appl. Mater. Interfaces* **2013**, *5*, 291–300.

55) Rzayev, J.; Hillmyer, M. A. Nanoporous Polystyrene Containing Hydrophilic Pores from an ABC Triblock Copolymer Precursor. *Macromolecules* **2005**, *38*, 3–5.

56) Rzayev, J.; Hillmyer, M. A. Nanochannel Array Plastics with Tailored Surface Chemistry. *J. Am. Chem. Soc.* **2005**, *127*, 13373–13379.

57) Bailey, T. S.; Rzayev, J.; Hillmyer, M. A. Routes to Alkene and Epoxide Functionalized Nanoporous Materials from Poly(styrene-*b*-isoprene-*b*-lactide) Triblock Copolymers. *Macromolecules* **2006**, *39*, 8772–8781.

58) Chan, V. Z.; Hoffman, J.; Lee, V. Y.; Iatrou, H.; Avgeropoulos, A.; Hadjichristidis, N.; Miller, R. D.; Thomas, E. L. Ordered Bicontinuous Nanoporous and Nanorelief Ceramic Films from Self Assembling Polymer Precursors. *Science.* **1999**, *286*, 1716–1719.

59) Zalusky, A. S.; Olayo-Valles, R.; Wolf, J. H.; Hillmyer, M. A. Ordered Nanoporous Polymers from Polystyrene-Polylactide Block Copolymers. *J. Am. Chem. Soc.* **2002**, *124*, 12761–12773.

60) Ndoni, S.; Vigild, M. E.; Berg, R. H. Nanoporous Materials with Spherical and Gyroid Cavities Created by Quantitative Etching of Polydimethylsiloxane in Polystyrene–Polydimethylsiloxane Block Copolymers. *J. Am. Chem. Soc.* **2003**, *125*, 13366–13367.

61) Wolf, J. H.; Hillmyer, M. A. Ordered Nanoporous Poly(cyclohexylethylene). *Langmuir* **2003**, *19*, 6553–6560.

62) Mao, H.; Hillmyer, M. A. Nanoporous Polystyrene by Chemical Etching of Poly(ethylene oxide) from Ordered Block Copolymers. *Macromolecules* **2005**, *38*, 4038–4039.

63) Bertrand, A.; Hillmyer, M. A. Nanoporous Poly(lactide) by Olefin Metathesis Degradation. *J. Am. Chem. Soc.* **2013**, *135*, 10918–10921.

64) Seo, M. *Submicron Porous Materials*; Bettotti, P., Ed.; Springer: Cham, Switzerland, 2017; pp 59, 61, 62.

65) Kim, S.; Yoo, M.; Kang, N.; Moon, B.; Kim, B. J.; Choi, S.; Kim, J. U.; Bang, J. Nanoporous Bicontinuous Structures via Addition of Thermally-Stable Amphiphilic Nanoparticles within Block Copolymer Templates. *ACS Appl. Mater. Interfaces* **2013**, *5*, 5659–5666.

66) Chen, L.; Phillip, W. A.; Cussler, E. L.; Hillmyer, M. A. Robust Nanoporous Membranes Templated by a Doubly Reactive Block Copolymer. *J. Am. Chem. Soc.* **2007**, *129*, 13786–13787.

67) Amendt, M. A.; Roerdink, M.; Moench, S.; Phillip, W. A.; Cussler, E. L.; Hillmyer, M. A. Functionalized Nanoporous Membranes from Reactive Triblock Polymers. *Aust. J. Chem.* **2011**, *64*, 1074–1082.

68) Seo, M.; Murphy, C. J.; Hillmyer, M. A. One-Step Synthesis of Cross-Linked Block Polymer Precursor to a Nanoporous Thermoset. *ACS Macro Lett.* **2013**, *2*, 617–620.

69) Seo, M.; Kim, S.; Oh, J.; Kim, S.-J.; Hillmyer, M. A. Hierarchically Porous Polymers from Hyper-Cross-Linked Block Polymer Precursors. *J. Am. Chem. Soc.* **2015**, *137*, 600–603.

70) Larsen, M. B.; Horn, J. D. Van; Wu, F.; Hillmyer, M. A. Intrinsically Hierarchical Nanoporous Polymers via Polymerization-Induced Microphase Separation. *Macromolecules* **2017**, *50*, 4363-4371.

71) Schulze, M. W.; Hillmyer, M. A. Tuning Mesoporosity in Cross-Linked Nanostructured Thermosets via Polymerization-Induced Microphase Separation. *Macromolecules* **2017**, *50*, 997–1007.

72) Oh, J.; Seo, M. Photoinitiated Polymerization-Induced Microphase Separation for the Preparation of Nanoporous Polymer Films. *ACS Macro Lett.* **2015**, *4*, 1244–1248.

73) Schulze, M. W.; McIntosh, L. D.; Hillmyer, M. A.; Lodge, T. P. High-Modulus, High-Conductivity Nanostructured Polymer Electrolyte Membranes via Polymerization-Induced Phase Separation. *Nano Lett.* **2014**, *14*, 122–126.

74) McIntosh, L. D.; Schulze, M. W.; Irwin, M. T.; Hillmyer, M. A.; Lodge, T. P. Evolution of Morphology, Modulus, and Conductivity in Polymer Electrolytes Prepared via Polymerization-Induced Phase Separation. *Macromolecules* **2015**, *48*, 1418–1428.

75) Chopade, S. A.; So, S.; Hillmyer, M. A.; Lodge, T. P. Anhydrous Proton Conducting Polymer Electrolyte Membranes via Polymerization-Induced Microphase Separation. *ACS Appl. Mater. Interfaces* **2016**, *8*, 6200–6210.

76) Chopade, S. A.; Au, J. G.; Li, Z.; Schmidt, P. W.; Hillmyer, M. A.; Lodge, T. P. Robust Polymer Electrolyte Membranes with High Ambient-Temperature Lithium-Ion Conductivity via Polymerization-Induced Microphase Separation. *ACS Appl. Mater. Interfaces* **2017**, *9*, 14561–14565.

77) Yang, X.-Y.; Chen, L.-H.; Li, Y.; Rooke, J. C.; Sanchez, C.; Su, B.-L. Hierarchically Porous Materials: Synthesis Strategies and Structure Design. *Chem. Soc. Rev.* **2017**, *46*, 481–558.

78) Li, Y.; Tolley, H. D.; Lee, M. L. Size-Exclusion Separation of Proteins Using a Biocompatible Polymeric Monolithic Capillary Column with Mesoporosity. *J. Chromatogr. A* **2010**, *1217*, 8181–8185.

79) Sai, H.; Tan, K. W.; Hur, K.; Asenath-Smith, E.; Hovden, R.; Jiang, Y.; Riccio, M.; Muller, D. A.; Elser, V.; Estroff, L. A.; Gruner, S. M.; Wiesner, U. Hierarchical Porous Polymer Scaffolds from Block Copolymers. *Science* **2013**, *341*, 530–534.

80) Gruber, M. F.; Schulte, L.; Ndoni, S. Nanoporous Materials Modified with Biodegradable Polymers as Models for Drug Delivery Applications. *J. Colloid Interface Sci.* **2013**, *395*, 58–63.

81) Weidman, J. L.; Mulvenna, R. A.; Boudouris, B. W.; Phillip, W. A. Unusually Stable Hysteresis in the pH-Response of Poly(acrylic acid) Brushes Confined within Nanoporous Block Polymer Thin Films. *J. Am. Chem. Soc.* **2016**, *138*, 7030–7039

82) Ahn, H.; Park, S.; Kim, S.; Yoo, P. J.; Ryu, D. Y.; Russell, T. P. Nanoporous Block Copolymer Membranes for Ultrafiltration: A Simple Approach to Size Tunability. *ACS Nano* **2014**, *8*, 11745–11752.

83) Yan, N.; Wang, Y. Reversible Switch between the Nanoporous and Nonporous State of Amphiphilic Block Copolymer Films Regulated by Selective Swelling. *Soft Matter* **2015**, *11*, 6927–6937.

Chapter 2. Experimental Techniques and Data Processing

Unless otherwise noted, all chemicals were purchased from Sigma Aldrich and used as received.

2.1 Polymerization Methods

2.1.1 Synthesis of Macro-Chain Transfer Agent

The chain transfer agent (CTA) (*S*)-1-dodecyl-(*S′*)-(*α*,*α′*-dimethyl-*α″*-acetic acid) trithiocarbonate was synthesized following a procedure modified from literature.[1] 1-dodecanethiol (10 g, 0.049 mol), acetone (102 mL), carbon disulfide (4.1 g, 0.054 mol), and chloroform (14.5 mL) were mixed under argon. The solution was cooled to 0 °C, and 25 mL of a 50 wt% potassium hydroxide solution was added dropwise. The reaction was stirred for 16 h at room temperature. The mixture was then diluted with 20 mL of water, acidified with 10 mL of concentrated HCl, and stirred for 16 h at room temperature. The volatiles were removed on a rotary evaporator and the solid product was filtered and rinsed with water. The solid was then dissolved in IPA and the byproduct *S,S'*-bis(1-dodecyl)trithiocarbonate crystallized and was removed via filtration. The IPA solution was then evaporated to dryness and the resulting solid was recrystallized from hexanes to afford 13 g of yellow crystalline solid.

2.1.1.1 Synthesis of PLA-OH

Hydroxyl terminated poly(lactide) (PLA-OH) was synthesized in a nitrogen atmosphere drybox through the ring-opening polymerization of D,L-lactide (kindly provided by

Altasorb) using anhydrous benzyl alcohol as the initiator. Prior to use, the D,L-lactide was recrystallized twice from dry toluene and stored in a nitrogen atmosphere drybox. Either triethylaluminum (1 M solution in hexanes)[2] or 1,8-Diazabicyclo[5.4.0]undec-7-ene (DBU)[3] were used as catalysts. For the former, benzyl alcohol and triethylaluminum (2:1 molar) were stirred for 16 h in toluene (7 mL toluene per 1 g D,L-lactide) in a pressure vessel. D,L-lactide was then added and the pressure vessel was sealed and placed in a pre-heated 90 °C oil bath. After 4 h, the polymerization was exposed to air, a drop of solution was removed and diluted in $CDCl_3$ to obtain a NMR of the crude reaction mixture (Figure 2.1), and the reaction was quenched using 1.0 M HCl (ca. 5 mL HCl per 100 mL toluene). In the crude NMR, the peaks at 5.20 ppm correspond to the polymer methine groups, and the quartet at 4.94 ppm is assigned to the monomer methine protons. Monomer conversion was calculated by dividing the relative integration of the polymer by the relative integrations of the polymer plus monomer. In most cases, the reaction was intentionally stopped at conversions of 75 – 80 % to maintain a low dispersity (ca. 1.10). This reaction was typically conducted using 5 – 10 g D,L-lactide with less than half of the volume of the pressure vessel filled, resulting in PLA-OH with M_n between 10 and 35 kg mol^{-1}, depending on the initial D,L-lactide:benzyl alcohol loading. For the DBU catalyzed polymerizations, DBU and benzyl alcohol (1:1 molar) were stirred in dry DCM (10 mL DCM per 1 g D,L-lactide) for 5 min. D,L-lactide was then added and polymerized for 1.25 h at room temperature. After removing an aliquot for NMR analysis of the crude reaction mixture, the DBU was quenched with benzoic acid. Monomer conversion typically reached 90 – 95 %. In both cases, the polymer was purified by precipitation into

methanol, re-dissolving in minimal DCM, and reprecipitation into hexanes (if triethylaluminum was used) or methanol (for DBU). The polymer was then dried at 50 – 60 °C under reduced pressure for 16 h. A representative NMR spectrum of purified polymer is shown in Figure 2.2. M_n was calculated from end group analysis using the integrations of the terminal methine at 4.3 ppm and the methine protons in the polymer backbone at 5.2 ppm.

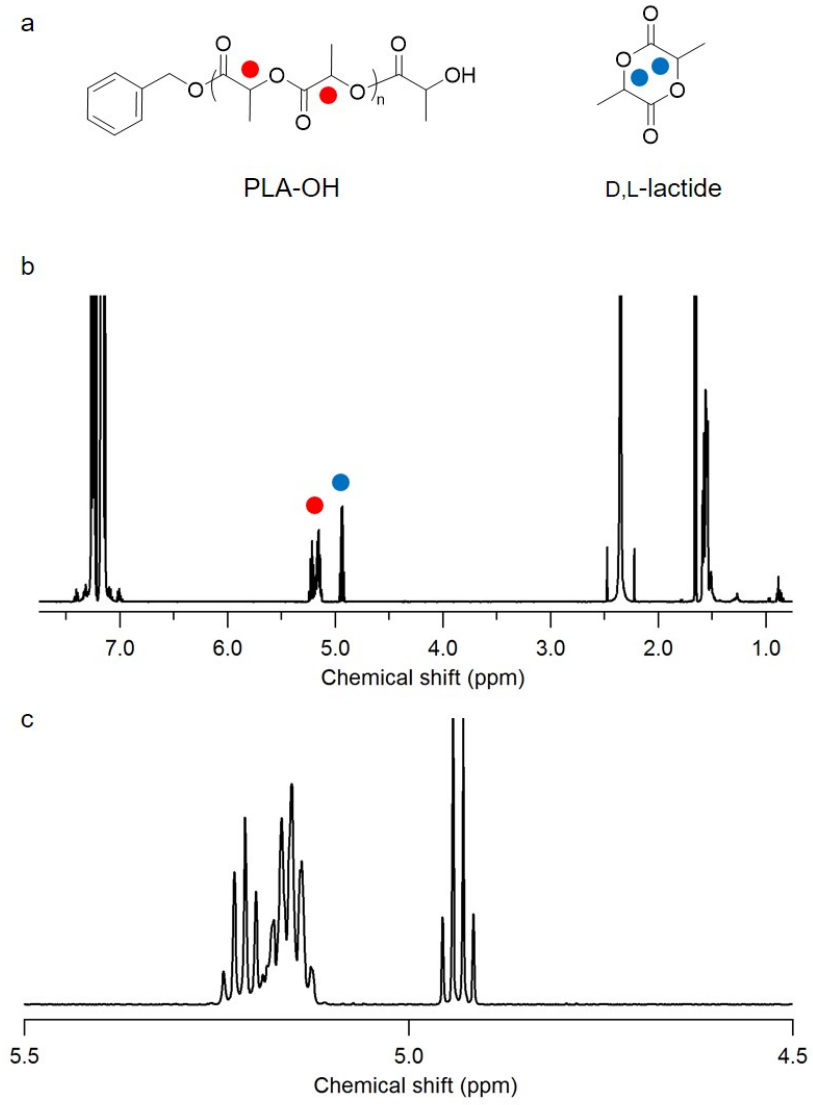

Figure 2.1. (a) Chemical structure of PLA-OH and D,L-lactide. (b) Crude ^{1}H NMR of PLA-OH prepared with triethylaluminum as a catalyst in toluene. (c) Expansion of the peaks used to calculate monomer conversion.

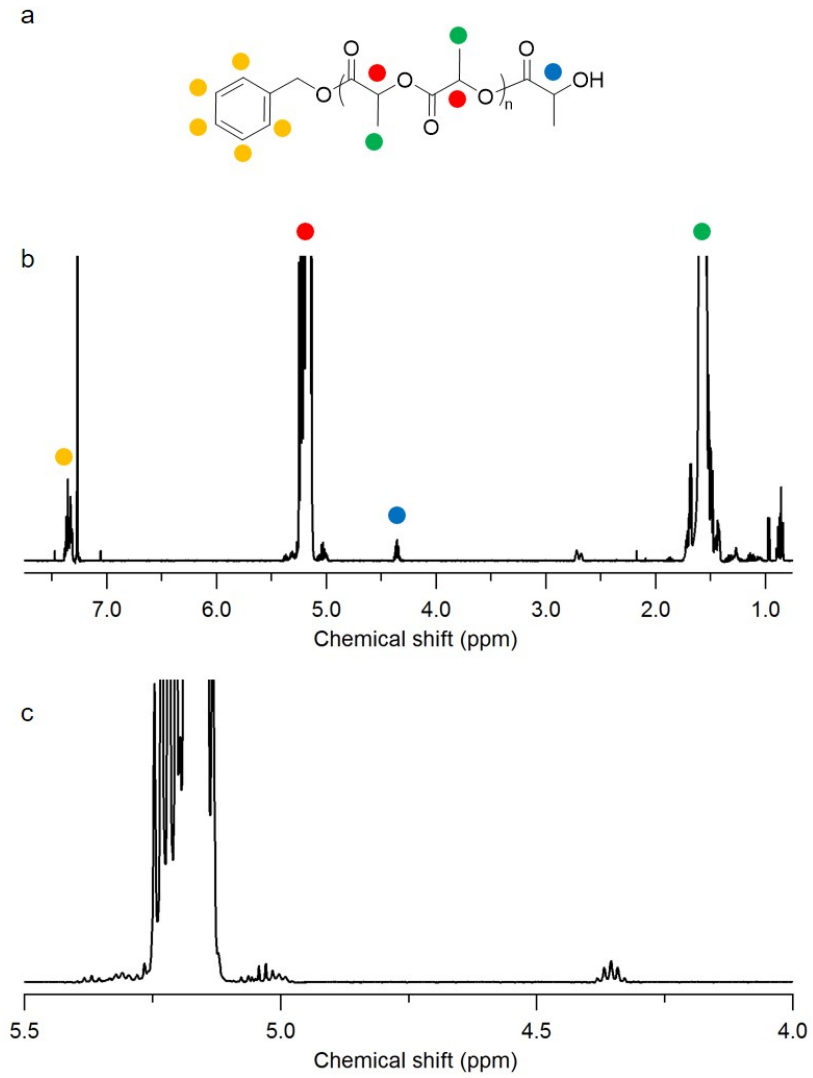

Figure 2.2. (a) Chemical structure PLA-OH with NMR peak assignments. (b) ^{1}H NMR of purified PLA-OH prepared with triethylaluminum as a catalyst in toluene. (c) Expansion of the peaks used to calculate M_n.

2.1.1.2 End Functionalization of Hydroxyl Terminated Polymers

The end functionalization of PLA-OH to PLA-CTA is described here. The same procedure was also used to prepare poly(ethylene oxide)-CTA (PEO-CTA) from hydroxyl-terminated PEO. The CTA was coupled to the hydroxyl terminus of PLA-OH via transesterification through an acid chloride intermediate.[2] Oxalyl chloride and the

CTA were mixed in dry DCM (15 mL per ~0.5 g CTA) under an argon atmosphere for 2 h until gas evolution stopped. The excess reagents were then removed under vacuum and the solid CTA acid chloride was redissolved in dry DCM (20 mL per ~0.5 g CTA). Any residual water was removed from PLA-OH by azeotropic drying from toluene at ca. 10 Torr and 40 °C. PLA-OH was then dissolved in dry DCM (10 mL per 1 g PLA), added to the CTA acid chloride, and stirred for 48 h at room temperature. A typical reaction used oxalyl chloride/CTA/PLA-OH at a 10/5/2 molar ratio with 2 – 10 g PLA-OH. The polymer was then twice precipitated into hexanes and dried under vacuum overnight at 50 – 60 °C. Complete functionalization was confirmed using quantitative ^{1}H NMR end group analysis (Figure 2.3) and by SEC analysis of linear PLA-*b*-PS block polymers synthesized using PLA-CTA as the macroinitiator. SEC chromatographs were monomodal and contained no residual PLA-CTA.

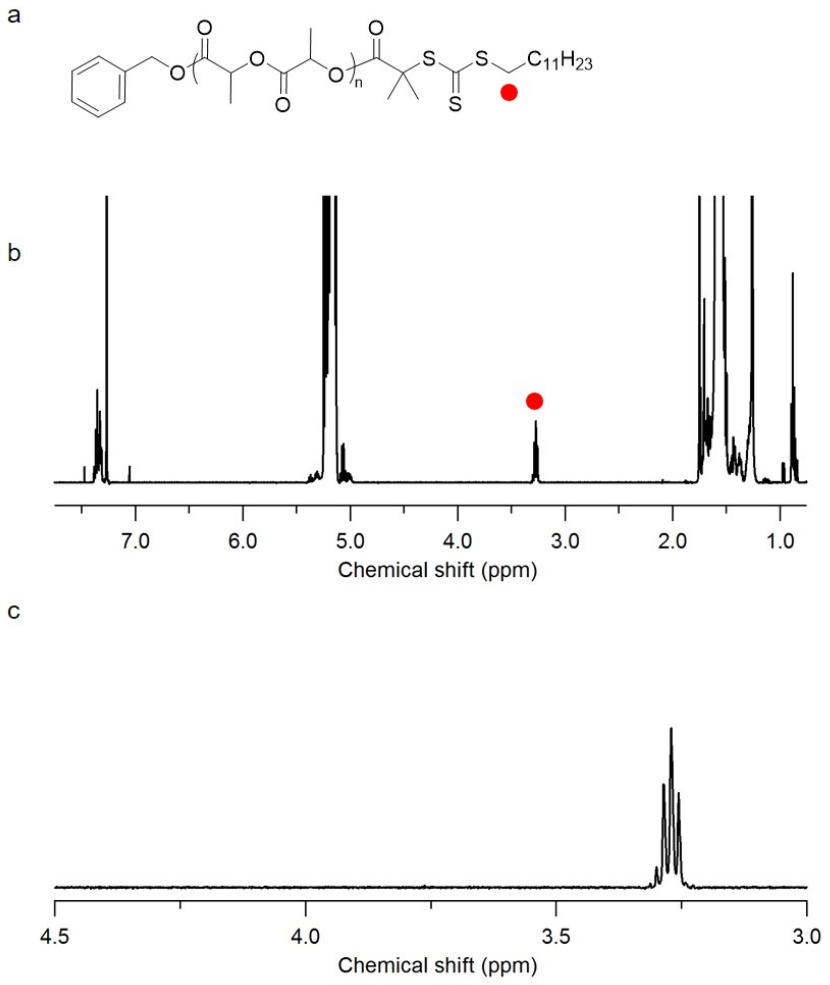

Figure 2.3. (a) Chemical structure of PLA-CTA with the end group identified for calculation of M_n. (b) ^{1}H NMR of purified PLA-CTA. (c) Expansion of the spectrum around the end group in PLA-CTA used to calculate M_n.

2.1.1.3 Synthesis of PI-CTA and PLA-*b*-PI-CTA

The reversible addition-fragmentation chain transfer (RAFT) polymerization of isoprene to yield PI-CTA followed the work of Germack and Wooley and is summarized here.[4,5] It should be noted that the polymerization temperature (125 °C) is significantly above the boiling point of isoprene (34 °C) therefore polymerizations were conducted in fume hoods with additional shielding, and in pressure vessels with at least half of the volume

unoccupied. Isoprene and *t*-butyl peroxide, the thermal radical initiator, were filtered over dried neutral alumina prior to use. In a typical polymerization, isoprene, *t*-butyl peroxide, and DDMAT (5/1 molar ratio CTA/initiator) were added to a dried sidearm pressure vessel with stir bar, degassed through three freeze-pump-thaw cycles, and backfilled with 3 psi of argon. The pressure vessel was then placed in a pre-heated oil bath at 125 °C for 21 – 25 h. The polymerization was stopped by cooling in liquid nitrogen; the mixture was then warmed to room temperature and excess isoprene was removed under vacuum. The polymer was then dissolved in minimal DCM, precipitated in methanol, and dried under vacuum at 50 – 60 °C yielding a viscous yellow oil. NMR analysis showed predominately 1,4-addition (92 – 96 %, Figure 2.4). The final polymers had low dispersities as measured with SEC, typically from 1.15 (based on LS detection) to 1.40 (based on RI detection), consistent with the RAFT mechanism (Figure 2.5). For molar masses less than ~10 kg mol^{-1}, monomer conversions of ~30 % were obtained (calculated using moles of isoprene monomer relative to CTA and the molar mass of the polymer based on ^{1}H NMR end group analysis, assuming each polymer chain contains a CTA end group), consistent with the work of Germack and Wooley.[4,5] For molar masses of 10 – 20 kg mol^{-1}, monomer conversions of ~10 % were obtained. In these cases, excess monomer was added to account for the lower conversion. Germack and Wooley do not report polymers in this size range, therefore no comparison can be made. Typical polymerizations used between 20 – 40 mL of isoprene monomer in an appropriately sized pressure vessel.

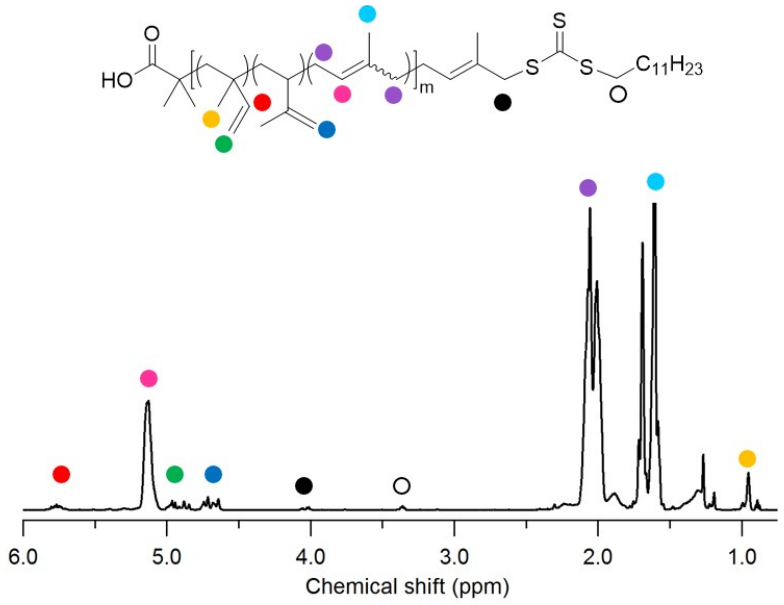

Figure 2.4. ^{1}H NMR spectrum with peak assignments for a representative PI-CTA.

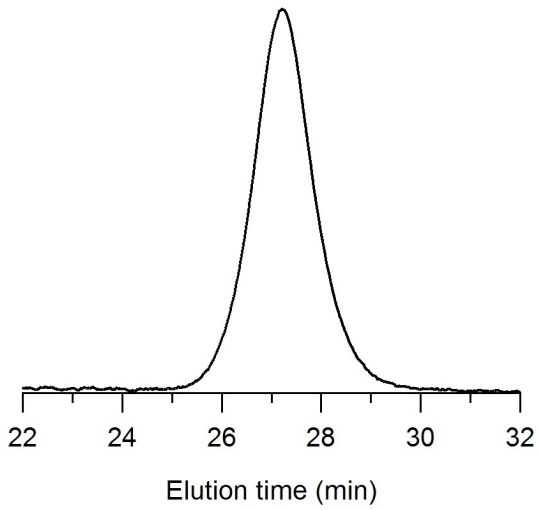

Figure 2.5. Representative SEC chromatograph of PI-CTA in THF with LS detection.

Germack and Wooley also describe the preparation of block polymers containing PI using RAFT.[4,5] These procedures were adapted to polymerize isoprene from PLA-CTA to yield PLA-*b*-PI-CTA. Isoprene, *t*-butyl peroxide, and dioxane were filtered over dried

neutral alumina prior to use. In a typical polymerization, PLA-CTA, isoprene, *t*-butyl peroxide (5/1 molar ratio CTA/initiator), and dioxane (ca. 4 mL dioxane per 1 g PLA-CTA) were vortexed in a 20 mL scintillation vial to afford a clear yellow solution. The reaction mixture was transferred to a dried sidearm pressure vessel equipped with a stir bar and degassed by three cycles of freeze-pump-thaw. After the third cycle, the vessel was backfilled with 3 psi of argon, sealed, and immersed in an oil bath at 125 °C for 21 h. The polymerization was quenched by immersion in liquid nitrogen. The solution was then warmed to room temperature and excess monomer was removed under vacuum. The remaining yellow solid was dissolved in minimal DCM and twice precipitated into cold methanol. The polymer was then dried under reduced pressure at 55 °C for 16 h. Yield: 0.72 g, M_n^{NMR} = 6.9 kg mol^{-1} (Figure 2.6). Overlays of SEC traces of PLA-CTA and PLA-*b*-PI-CTA showed a peak shift indicating growth of the PI block (Figure 2.7). The high molar mass shoulder is attributed to light cross-linking of the PI and the low molar mass peak is attributed to PI homopolymer formation.

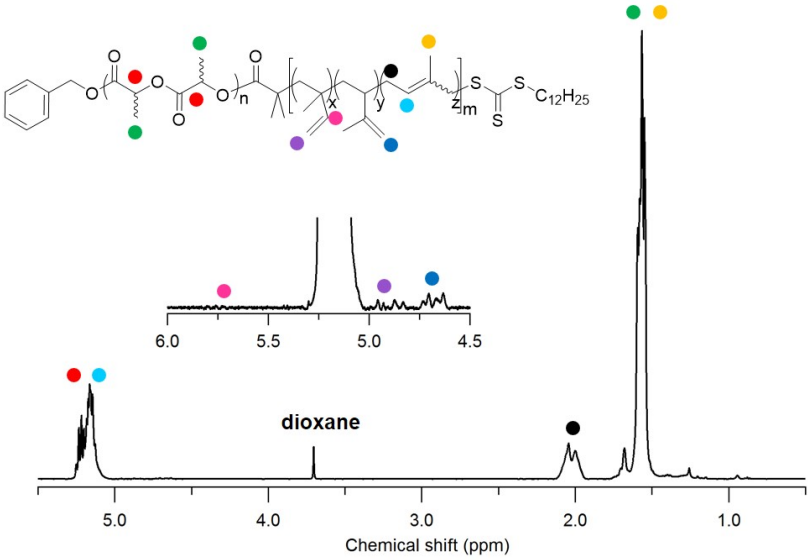

Figure 2.6. Representative ^{1}H NMR spectrum of PLA-*b*-PI-CTA macroinitiator in $CDCl_3$.

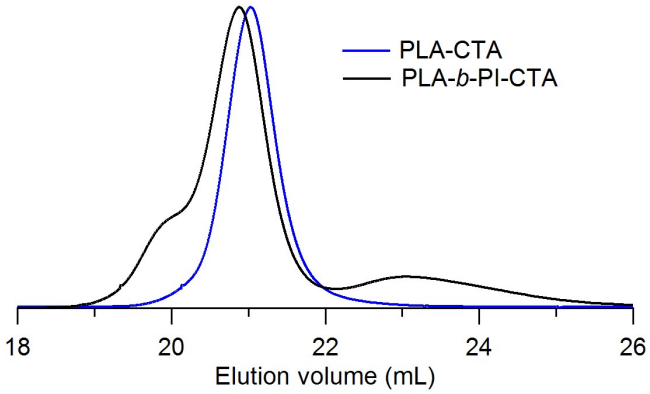

Figure 2.7. SEC traces (RI signal) in $CHCl_3$ of the PLA-CTA and PLA-*b*-PI-CTA macro-CTAs. The high molar mass shoulder is attributed to light cross-linking of the PI and the low molar mass peak is attributed to PI homopolymer formation.

Macro-CTAs containing PI showed an increase in dispersity when stored for a few months in the freezer, therefore later batches of these polymers were stabilized with butylated hydroxytoluene (BHT) for long term storage. First, the polymer was mixed with BHT (0.5 wt%) by codissolving in minimal benzene. The benzene was then

removed via freeze-drying and the stabilized polymers were stored in the freezer. BHT was removed from the polymer prior to use via precipitation of the polymer into methanol.

2.1.2 Synthesis of Polymer Monoliths

Styrene (99%) and divinylbenzene (technical grade, 80%) were filtered over basic alumina prior to use. Azobisisobutryonitrile (AIBN) (98%) was recrystallized from methanol and dried under reduced pressure for 16 h.

2.1.2.1 Monoliths Prepared with Nonreactive Porogens

Chapters 3 and 4 study the effect of nonreactive additives (PEO-OH or PLA-OH) on the morphology of nanoporous polymer monoliths. Reactions were performed in 1 dram vials, sealed with electrical tape, without degassing. PLA-CTA and the additive were dissolved in a 4/1 molar ratio mixture of S/DVB at the specified concentrations. The solution was well mixed, and then AIBN (2 wt% in toluene, 0.4 molar equivalents to PLA-CTA) was added. Polymerizations were run at 120 °C for 20 h. The resulting solid monoliths were dried under reduced pressure for 16 h. The appearance varied from translucent yellow (when a single length scale was present in the material) to opaque white (in the case of the hierarchically meso- and macroporous monoliths). Monoliths for electrochemical testing were prepared in two different ways. In one route, monoliths were polymerized in 1 dram vials and then sanded 3 mm thickness. Cylindrical plugs of diameter 3 mm were obtained using an end mill. In another route, the polymerization was

conducted in a sealed NMR tube to yield a 4 mm diameter cylindrical piece. This piece was then cut to several cylinders of height 3.5 mm.

2.1.2.2 Monoliths Prepared with PI-CTA

Chapter 5 describes the morphology of monoliths prepared from blends of PLA-CTA and PI-CTA. When dissolved in S and DVB, these macro-CTAs form yellow solutions. However, early attempts to copolymerize S and DVB from these blends using the previously described conditions yielded discolored monoliths, typically dark orange in color. It is plausible that some of the PI oxidized during the copolymerization, therefore all later polymerizations were conducted under argon atmosphere. In a typical reaction, PLA-CTA, PI-CTA, and AIBN (0.4 molar equiv. to macro-CTA) were dissolved in S and DVB in a 2 dram vial with a re-sealable cap at the specified concentrations. The solution was then sparged with argon for 1.5 min and sealed with electrical tape. At room temperature, these solutions were phase-separated, therefore the solutions were vortexed until turbid and then immediately placed in a preheated 120 °C oil bath for 20 h. The obtained solids were dried under reduced pressure for 16 h.

2.2 Etching Methods

2.2.1 Etching of PLA

PLA was primarily etched from the monoliths using solutions of aqueous base. The monolith was placed in a polypropylene vial containing a 0.5 M NaOH solution in 6/4 water/methanol (v/v). The vials were sealed with electrical tape and heated for 2 – 3 days

at 70 °C. Shorter etch times were sufficient for powders and submillimeter-sized pieces. The etched monoliths were then iteratively rinsed with water and methanol. For dry state characterization, the monoliths were dried under reduced pressure for 16 h. Complete removal of PLA was confirmed by FTIR and gravimetric analysis. For electrochemical testing, the monoliths were placed in fresh DI water, without vacuum drying, to maintain the wetting of the pores. When the etched monoliths were brittle, typically in the case of void fractions exceeding 50 vol%, the monoliths were cut to the desired shape prior to etching.

The above procedure resulted in some residual base in the pores of the monolith. When the monoliths contained PI, the residual base prevented the subsequent metathetic degradation of PI as it caused early decomposition of the metathesis catalyst. In these cases, the PLA was etched via hydrolysis with trifluoroacetic acid, in a procedure modified from the literature.[6] Monoliths were placed in 2 dram vials containing 1/1 v/v trifluoracetic acid/methanol for 4 days at 40 °C. The etched monoliths were washed in methanol and dried under vacuum for 16 h at room temperature which resulted in complete removal of the trifluoracetic acid.

2.2.2 Etching of PI

PI was etched using cross-metathesis with *trans*-4-octene as the cross metathesis counterpart. Monoliths were prepared as coarse powders and placed in 2 dram vials with Grubbs 2nd Generation catalyst (GII, 100/1 molar equiv. of PI repeat units/GII). The vial

was flushed with argon for 5 min. Prior to use, *trans*-4-octene and dry cyclohexane were degassed with an argon sparge. A solution of *trans*-4-octene (20/1 molar equiv. *trans*-4-octene/GII) and cyclohexane (0.2 – 1.3 mL for 0.050 g monolith) was prepared using an argon-filled syringe and was added to the vial containing the monolith. The reaction mixture was sparged for another 1 min and sealed with electrical tape. The reaction was left at room temperature for 4 days over which time the solution turned from pink to golden-brown. Cross-metathesis degradation byproducts were removed by soaking the monolith in pure cyclohexane for 1 day. The monolith was then dried under vacuum at room temperature for 16 h. Gravimetric analysis showed that approximately 82 wt% of the PI was removed regardless of the volume of cyclohexane.

2.3 Characterization Methods

^{1}H NMR Spectroscopy

Spectra were obtained on a Bruker Advance III HD 500 MHz spectrometer in $CDCl_3$. Chemical shifts are reported in ppm referenced to the protic impurities in $CDCl_3$. For determination of M_n by end group analysis, spectra are reported as the average of 64 scans with a 10 s delay. For determination of M_n of block polymers by comparing relative integrations of backbone protons, spectra are reported as the average of 64 scans with a 20 s delay.

SEC

SEC in THF was performed at 25 °C using an Agilent 1260 Infinity liquid chromatograph system equipped with three Waters Styragel columns in series, as well as a Wyatt DAWN Heleos II 18-angle laser light scattering detector and a Wyatt OPTILAB T-rEX refractive index detector. Absolute weight-average molar mass was determined using the light scattering detector with a dn/dc of 0.049 mL g^{-1} for PLA and 0.124 mL g^{-1} for PI.

SEC in $CHCl_3$ was performed on an Agilent 1100 liquid chromatograph system at 35 °C with a flow rate of 1 mL min^{-1} and a HP1047A refractive index detector. The separation was obtained on Varian PLgel Mixed C columns.

DSC

DSC analyses were performed on a TA Instruments Discovery DSC calibrated with indium using standard aluminum T-zero pans with hermetic lids. Scans were conducted under a nitrogen purge with an empty pan as a reference. Typically, 4 – 6 mg samples were heated to 75 °C at a rate of 10 °C min^{-1}, cooled to –90 °C at 2 °C min^{-1}, and reheated to 225 °C at 10 °C min^{-1}. For consistency, T_g was determined from the second heating ramp.

DMTA

DMTA was performed on a TA Instruments RSA-G2 Solids Analyzer. Rectangular bars, prepared following a literature procedure,[7] of dimensions 1.10 × 0.50 mm were loaded with an initial gap of 3.39 mm. The sample was heated under nitrogen at a ramp rate of 5 °C min^{-1} and oscillated at a frequency of 1 Hz.

TGA

TGA analyses were performed on a TA Instruments Q500 under house nitrogen or air at a heating rate of 10 °C min^{-1}.

FTIR

Spectra were obtained on a Bruker Alpha Platinum ATR spectrometer and are the average of 32 scans.

Elemental Analysis

Elemental analysis was performed at Atlantic Microlabs (Norcross, GA). Samples were dried under reduced pressure for a minimum of 16 h then sealed in glass vials with parafilm. The reported averages and standard deviations are from three separate samples.

SAXS

SAXS profiles were collected at the Advanced Photon Source (APS) at Argonne National Laboratories using the Sector 5-ID-D beamline, which is maintained by the DuPont-

Northwestern-Dow Collaborative Access Team. Monolithic pieces (~ 2 mm × 2 mm) were loaded into sample holders without further processing. When the monoliths were too brittle to be directly loaded, they were first prepared as powders and packed into the sample holder. Room temperature measurements were acquired by packing samples into washers using Kapton tape and then mounting on the sample stage. Variable temperature measurements were acquired by loading the polymer into a quartz capillary and mounting on a Linkham heating stage. The sample was heated at 10 °C min^{-1} and scattering profiles were collected at 5 °C intervals. In both cases, typical exposure times were 0.1 – 1 s. Scattering experiments were performed using X-rays of wavelength 0.76 Å and the scattering intensity was collected on a 2D Mar CCD detector at room temperature with a sample to detector distance of 850 cm. Intensity as a function of the wavevector, q, where $q = (4\pi/\lambda) \sin(\theta/2)$ (θ is the scattering angle and λ is the X-ray wavelength), was obtained by azimuthally integrating the 2D patterns.

SEM

SEM micrographs were obtained on a Hitachi S-4700 or SU-8230 cold FEG-SEM with an accelerating voltage of 3 kV and an upper secondary electron detector. Images were obtained on cryo-fractured samples after either sputter coating or staining, as noted. In the case of coatings, ca. 3 nm of Pt (using either a VCR Group IBS TM200S Ion Beam Sputterer or a Balzers Union MED 010) or ca. 1 nm of Ir (using a Leica EM ACE600) was deposited. For staining, samples were stained in the bulk with OsO_4 at 50 °C or RuO_4 at room temperature for 20 min (caution, very toxic).

TEM

TEM images were acquired using a FEI Tecnai G2 Spirit BioTWIN with a LaB_6 gun and an accelerating voltage of 120 kV in bright-field mode. Prior to electron imaging, samples were microsectioned at −120 °C using LEICA UC6 microtome and stained with OsO_4.

Nitrogen Sorption

Nitrogen sorption isotherms were obtained on a Quantachrome Autosorb iQ^2-MP at liquid nitrogen temperature (77 K). Prior to measurement, samples were degassed for 20 h at room temperature using a turbomolecular vacuum pump. BET specific surface areas were obtained from the adsorption branch from $P/P_0 = 0.05 – 0.35$.[8] Pore volumes were determined from the point $P/P_0 = 0.95$.

Mesopore size distributions were estimated using either a quenched solid density functional theory (QSDFT) kernel for the adsorption branch of nitrogen on carbon with a cylindrical pore model[9] or with the model of Barrett, Joyner, and Halenda (BJH) applied to the desorption branch[10] as noted in the text. Both models use fits of the experimentally measured isotherm to calculate pore size distributions. The underlying assumptions of the two models are different; the former uses statistical mechanics to describe the adsorption process while the latter is based on macroscopic thermodynamic quantities. This results in differences in the calculated pore size distributions when comparing the two models to each other. In particular, for pores < 10 nm BJH calculates pore size distributions that are centered at smaller values than the QSDFT calculation.[11] Each model has its own advantages, and the choice of the model for fitting of experimental data is situation dependent. Because the BJH model was developed much earlier, it allows for a comparison of new materials to well established literature examples. BJH also has the advantage of being able to estimate pore size distributions into the macropore range. The main limitation is that it assumes the measured data is in equilibrium. This assumption may not hold for soft materials that can swell with the adsorbate (usually nitrogen), small pore sizes, or networked structures where desorption can occur by multiple mechanisms.

QSDFT, on the other hand, has only recently become available. QSDFT accounts for surface heterogeneities in a material, a feature that the earlier non-local DFT theory does not address. In addition to the ability to model adsorption as a metastable process, it provides a nanoscale description of the process. Currently, the main limitation to QSDFT

is a limited number of reference materials have been established, and these references may differ in surface chemistry from the material under study. Since neither theory describes disordered pore structures, data processing in this thesis is done assuming independent cylindrical pores. Importantly, the models are self-consistent, i.e. the pore size distributions produced by one model can be compared within a series of materials, and are used in this manner to compare properties of the materials within each chapter.

Impedance Spectroscopy

Impedance spectroscopy measurements were performed using a 1255B frequency response analyzer and a SI 1287 electrochemical interface from Solartron with a two-electrode system. A free flow double-junction AgCl/Ag electrode with 1.0 M lithium acetate bridge electrolyte was used as one of the electrodes. The other electrode was prepared as follows: a cylindrical monolith and a glass tube (7 cm long, 3 or 4 mm diameter) were placed in a heat shrink tube, and heated with a heat gun for 30 s to attach the monolith to the glass tube. An AgCl/Ag wire was inserted into the glass tube from the open end, the tube was filled with 1.0 mM KCl (pH 6.8), and the top of the glass tube was sealed with a septum. The electrodes were then placed in 100 mL of 1.0 mM KCl at time 0 h and the impedance was monitored for 70 h. The electrode was kept in 1.0 mM KCl (pH 6.8) during the entire measurement. The resistance of the monolith was determined from the collected spectra. The resistance at the interfaces of the reference electrode/1.0 mM KCl and the AgCl/Ag wire/1.0 mM KCl were measured to be negligible (less than 10%) compared the resistance of the monolith. Resistances were

obtained by fitting of impedance spectra with ZPlot software (Scribner Associates) in the 10^2 to 10^5 Hz range, and determined from the diameter of the semicircle.

The flow rate of solution out of the electrode was measured by filling the 5 cm glass tube attached to the frits with 3 M KCl, generating a pressure of 5 x 10^{-3} bar. The reference electrodes were then stored in a sealed container for 30 days and the change in solution volume was reported.

Potential Measurements

Potential measurements were performed with a Lawson Labs EMF 16 channel potentiometer controlled with EMF Suite 1.02 software. All measurements were acquired in stirred solutions prepared from deionized purified water (18.2 MΩ cm specific resistance, EMD Millipore) at room temperature (25 °C). Electromotive force (emf) was measured relative to a Metler Toledo DX200 free-flow double-junction.[12] Measurements with solutions of KCl, $CaCl_2$, Na_2SO_4, and tetrabutylammonium chloride were carried out by successive dilution. For pH measurements, pH was measured with a half-cell electrode from Metler Toledo. Measurements of pH were carried out by additions of 10 M KOH to 0.01 M HCl (with 10 mM or 100 mM supporting electrolyte). Three identically prepared reference electrodes were used for each measurement. Activity coefficients were calculated using the extended Debye-Hückel equation.[13] Activity coefficients and mobilities were used to correct all emf values for liquid junction potentials with the Henderson equation.[14]

2.4 References

1) Lai, J. T.; Filla, D.; Shea, R. Functional Polymers from Novel Carboxyl-Terminated Trithiocarbonates as Highly Efficient RAFT Agents. *Macromolecules* **2002**, *35*, 6754–6756.

2) Rzayev, J.; Hillmyer, M. A. Nanochannel Array Plastics with Tailored Surface Chemistry. *J. Am. Chem. Soc.* **2005**, *127*, 13373–13379.

3) Lohmeijer, B. G. G.; Pratt, R. C.; Leibfarth, F.; Logan, J. W.; Long, D. A.; Dove, A. P.; Nederberg, F.; Choi, J.; Wade, C.; Waymouth, R. M.; Hedrick, J.L. Guanidine and Amidine Organocatalysts for Ring-Opening Polymerization of Cyclic Esters. *Macromolecules* **2006**, *39*, 8574–8583.

4) Germack, D. S.; Wooley, K. L. Isoprene Polymerization via Reversible Addition Fragmentation Chain Transfer Polymerization. *J. Polym. Sci. Part A-Polymer Chem.* **2007**, *45*, 4100–4108.

5) Germack, D. S.; Wooley, K. L. RAFT-Based Synthesis and Characterization of ABC versus ACB Triblock Copolymers Containing *tert*-Butyl Acrylate, Isoprene, and Styrene Blocks. *Macromol. Chem. Phys.* **2007**, *208*, 2481–2491.

6) Sarkar, A.; Stefik, M. Robust Porous Polymers Enabled by a Fast Trifluoroacetic Acid Etch with Improved Selectivity for Polylactide. *Mater. Chem. Front.* **2017** DOI:10.1039/c6qm00266h.

7) Chopade, S. A.; Au, J. G.; Li, Z.; Schmidt, P. W.; Hillmyer, M. A.; Lodge, T. P. Robust Polymer Electrolyte Membranes with High Ambient-Temperature Lithium-Ion Conductivity via Polymerization-Induced Microphase Separation. *ACS Appl. Mater. Interfaces* **2017**, *9*, 14561–14565.

8) Brunauer, S.; Emmett, P. H.; Teller, E. Adsorption of Gases in Multimolecular Layers. *J. Am. Chem. Soc.* **1938**, *60*, 309–319.

9) Gor, G. Y.; Thommes, M.; Cychosz, K. A.; Neimark, A. V. Quenched Solid Density Functional Theory Method for Characterization of Mesoporous Carbons by Nitrogen Adsorption. *Carbon* **2012**, *50*, 1583–1590.

10) Barrett, E. P.; Joyner, Leslie, G.; Halenda, Paul, P. The Determination of Pore Volume and Area Distributions in Porous Substances. I. Computations from Nitrogen Isotherms. *J. Am. Chem. Soc.* **1951**, *73*, 373–380.

11) Thommes, M.; Cychosz, K. A.; Neimark, A. V. *Advanced Physical Adsorption Characterization of Nanoporous Carbons*, 1st ed.; Tascón, J., Ed.; Elsevier, 2012.

12) Dohner, R. E.; Wegmann, D.; Morf, W. E.; Simon, W. Reference Electrode with Free-Flowing Free-Diffusion Liquid Junction. *Anal. Chem.* **1986**, *58*, 2585–2589.

13) Debye, P.; Hückel. On the Theory of Electrolytes I. Freezing Point Depression and Related Phenomena. *Phys. Z.* **1923**, *24*, 185-206.

14) Bard, A. J.; Faulkner, L. R. *Electrochemical Methods: Fundamentals and Applications*, 2nd ed.; John Wiley and Sons: New York, 2001.

Chapter 3. Hierarchically Porous Polymer Monoliths by Combining Controlled Macro- and Microphase Separation[1]

3.1 Introduction

Hierarchically porous monoliths with a percolating macroporous (> 50 nm) network[1,2] and accessible mesopores (2–50 nm) are useful materials for liquid separations,[3,4] catalysis,[5] and biomedical applications.[6] Furthermore, the ability to tune the mesopore size enables size-selective filtration applications.[7,8] There are examples of such hierarchically porous carbons[9-11] and other inorganic materials,[12,13] but the development of synthetic routes to controlled pore sizes in such hierarchically porous polymers has been limited.[14-17] Most reports of hierarchically porous polymers with both meso- and macropores have focused on uncontrolled free radical polymerizations[18,19] or thin layer membrane fabrication.[20-22] Here, we report the facile controlled synthesis of porous polymer monoliths, and the ability to tune the nanostructure of the monolith from mesoporous to hierarchically porous, with percolating macropores. The versatility of this technique allows for ready tailoring of the mesopore size distribution.

---

[1]Reproduced with permission from Saba, S. A.; Mousavi, M. P. S.; Bühlmann, P.; Hillmyer, M. A. Hierarchically Porous Polymer Monoliths by Combining Controlled Macro- and Microphase Separation. *J. Am. Chem. Soc.* **2015**, *137*, 8896–8899. Copyright 2015 American Chemical Society.

Previously, Seo and Hillmyer reported the use of polymerization-induced microphase separation to prepare nanostructured polymer monoliths with interconnected mesopores.[23] The structure was generated using reversible-addition fragmentation chain transfer (RAFT) copolymerization of styrene (S) and divinylbenzene (DVB) from a poly(lactide) macro-chain transfer agent (PLA-CTA), during which in situ cross-linking trapped the disordered bicontinuous structure. Successive hydrolysis of the PLA domains produced mesoporous P(S-*co*-DVB). Subsequent work demonstrated the versatility of this approach through the introduction of a nonreactive functional additive that selectively swells a single domain of the block polymer while retaining the microphase-separated morphology.[24,25] Polymerization-induced formation of macroporosity in related systems is also well established; in this approach a nonreactive additive, such as a small molecule[26,27] or polymer,[28] is dissolved in a multifunctional monomer mixture. The additive is chosen to be insoluble in the polymer, resulting in polymerization-induced macrophase separation of the polymer from the additive. Removal of the additive or porogen can produce an interconnected macroporous polymer monolith.

3.2 Experimental Methods

Here we report a new hybrid approach to prepare porous polymer monoliths via the copolymerization of S and DVB from PLA-CTA (M_w = 31 kg mol^{-1}, $Đ$ = 1.08) in the presence of a nonreactive poly(ethylene oxide) (PEO) additive, as depicted in Figure 3.1. PEO is soluble in S and DVB monomers, and its miscibility with PLA allows for the formation of PLA/PEO composite domains in linear blends of PS-*b*-PEO/PS-*b*-PLA.[29]

We show that by restricting domain size via in situ cross-linking, the PLA domains cannot accommodate all compositions of PEO. At high molar mass, the PEO macrophase separates from the in situ formed PLA-*b*-P(S-*co*-DVB), leading to macroscopic features on the order of hundreds of nanometers. For all compositions, soaking the monolith in water allows for selective extraction of the PEO, and treatment with aqueous solutions of base results in removal of both the PLA and the PEO, producing a hierarchically porous polymer monolith. A typical reaction mixture composed of 26 vol% PLA-CTA (31 kg mol^{-1}) dissolved in a 4/1 molar mixture of S/DVB was combined with PEOs (30–70 vol% overall) of varying molar mass (5, 20, and 35 kg mol^{-1}). Simply heating for 20 h at 120 °C produced nanostructured polymer monoliths. By varying the molar mass and volume fraction of the PEO additive, the monolith morphology was easily tuned from mesoporous, with adjustable mean pore size, to hierarchically porous.

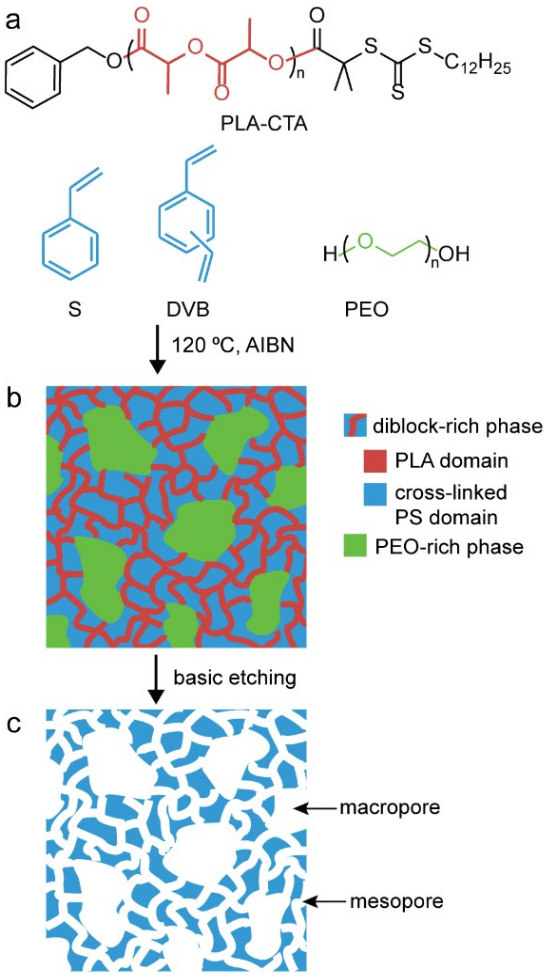

Figure 3.1. Preparation of hierarchically porous polymer monoliths. (a) The reaction mixture consists of PLA-CTA and PEO additive dissolved in S and DVB. (b) RAFT copolymerization is used to generate a PLA-*b*-P(S-*co*-DVB) diblock polymer. As a result of the copolymerization, the nonreactive PEO additive macrophase separates from the microphase-separated diblock polymer. (c) Etching in basic solution simultaneously degrades the PLA and dissolves the PEO, producing mesopores and macropores, respectively.

3.3 Results and Discussion

3.3.1 General Properties of Monoliths

Before removal of the PLA and PEO from the nanostructured monoliths, small-angle X-ray scattering (SAXS) indicated compositional heterogeneities on the order of 20-50 nm.

Broad principal scattering peaks in all samples are characteristic of a disordered microphase-separated block polymer. The shift of peak maxima towards low angle with increasing volume fraction of PEO is typical of blends of a diblock and homopolymer, indicating a shift towards macrophase separation (Figure 3.2).[30] In all the as-prepared monoliths, melting endotherms were observed upon heating by differential scanning calorimetry (DSC), consistent with incorporation of semi-crystalline PEO into the monoliths (Figure 3.3a). Subsequent removal of the PLA and the majority of the PEO was confirmed with Fourier transform infrared spectroscopy and by gravimetric analysis. In all cases, the characteristic carbonyl stretching band of the PLA (1755 cm^{-1}) was absent after the etching step (Figure 3.4). Furthermore, the nanostructural integrity was retained after etching, and resulted in nanoporous polymer monoliths, as evidenced by SAXS. Corresponding SAXS patterns for the porous monoliths exhibited no change in the position of the principal scattering peak when compared to the unetched precursors, and the increased scattering intensity is consistent with increased electron density contrast between the voids and the P(S-*co*-DVB) (Figure 3.2b). DSC thermograms of the etched monoliths showed a smaller melting endotherm, compared to the unetched precursors, due to low levels of trapped PEO in the cross-linked PS matrix (Figure 3.3b). Interestingly, the presence of residual PEO in the cross-linked PS matrix improved the wettability of the monolith, compared to monoliths prepared without any PEO additive. For example, monoliths with residual PEO were able to uptake water, as confirmed gravimetrically and by a dying experiment, while porous cross-linked PS were not (Figure 3.5).

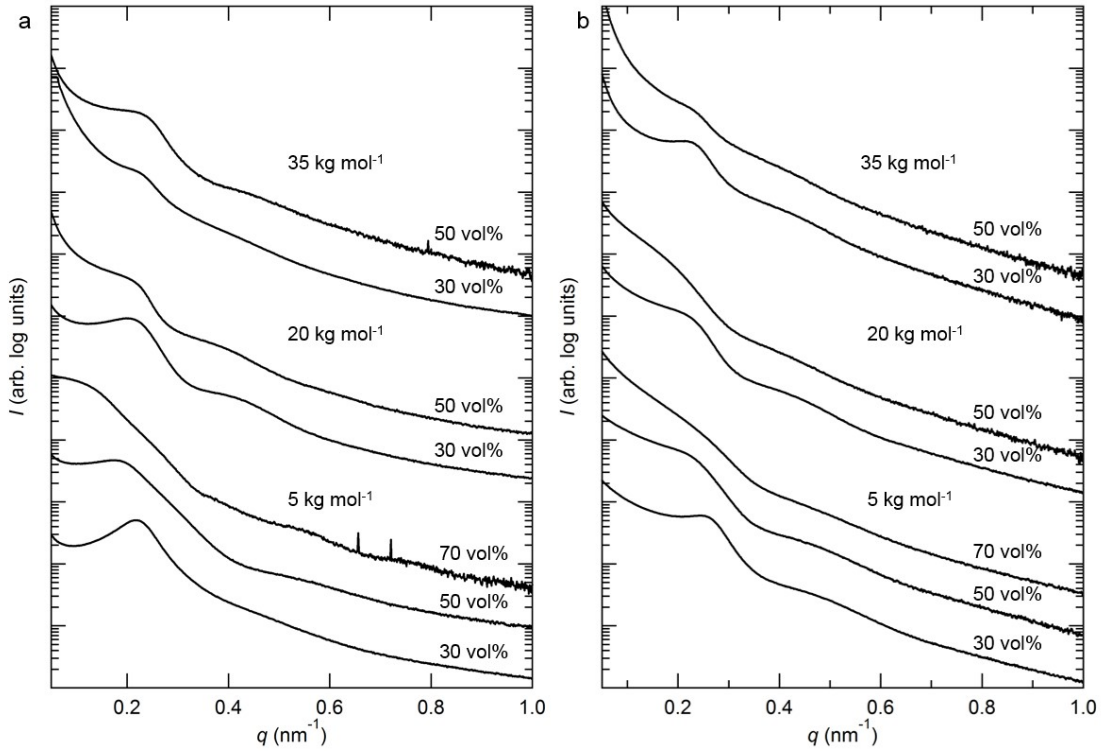

Figure 3.2. SAXS patterns of monoliths (a) before and (b) after etching of PLA and PEO. The increased scattering intensity after etching is consistent with the increased electron density contrast of the pores compared to the precursor block polymer.

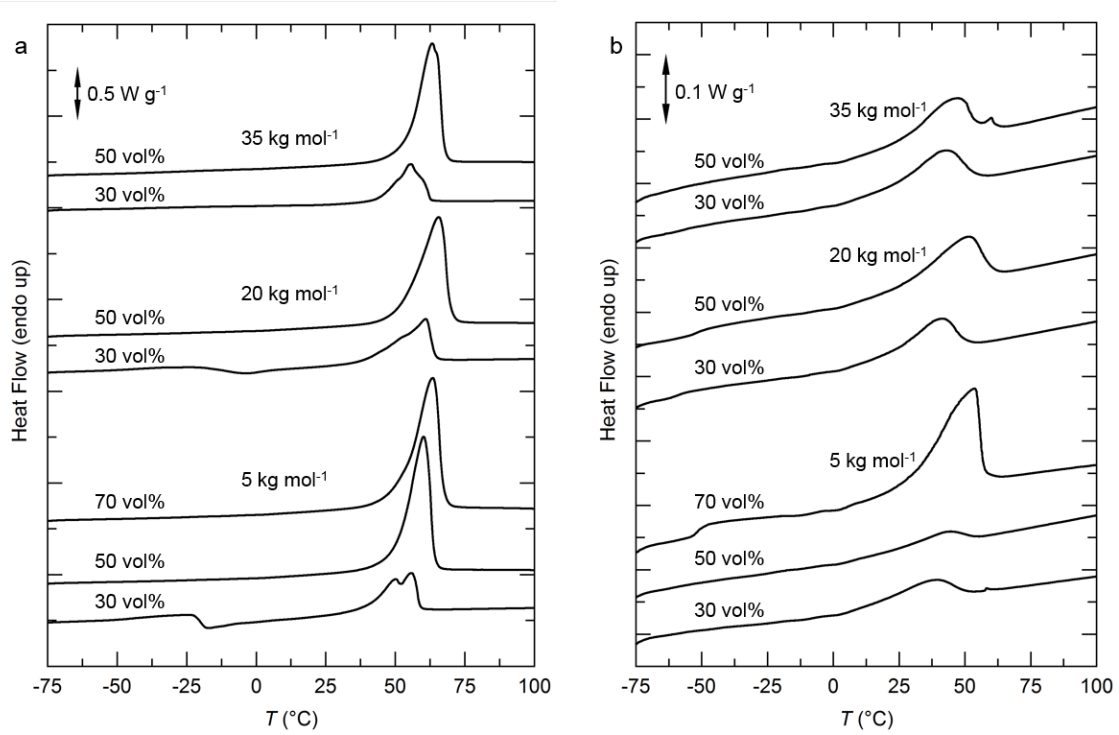

Figure 3.3. DSC thermograms of monoliths (a) before and (b) after etching in aqueous solution of base. The PLA glass transition is not observed due to its overlap with the temperature range of PEO melting. Thermograms shown are from the second heating at a rate of 10 °C min^{-1}.

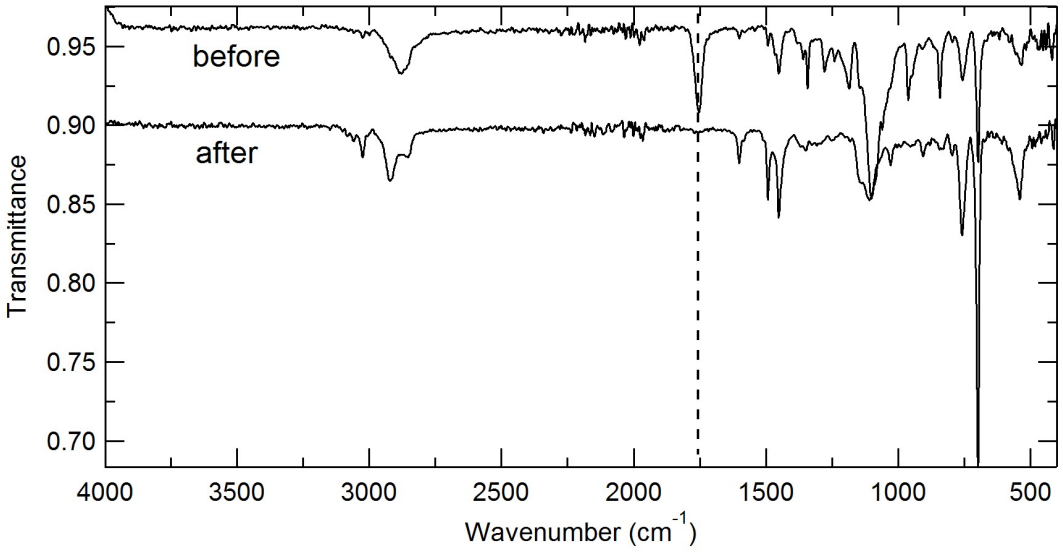

Figure 3.4. Representative FTIR spectra of a monolith before and after etching. The disappearance of the carbonyl stretching band of PLA at 1755 cm^{-1} (dashed line) corresponds to PLA removal.

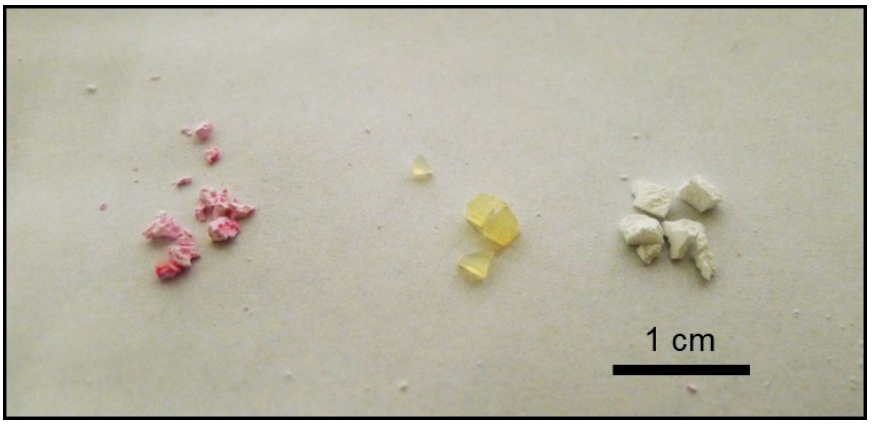

Figure 3.5. Photograph of a monolith prepared using 50 vol% 35 kg mol^{-1} PEO (left), a mesoporous P(S-*co*-DVB) monolith prepared without any PEO (middle), and a macroporous P(S-*co*-DVB) monolith prepared following a reported procedure using dodecanol as the porogen (right).[26] All monoliths were soaked in deionized H_2O with red dye for 24 h and then dried under reduced pressure.

3.3.2 Low Molar Mass PEO

The morphology of the porous monoliths was further characterized by scanning electron microscopy (SEM) and nitrogen sorption experiments. When varying amounts of 5 kg mol^{-1} PEO additive were introduced into the reaction mixture, the PEO swelled the PLA domains of the resulting cross-linked, nanostructured monolith. In these cases, SEM micrographs show that the resultant etched monoliths consist of a disordered mesoporous structure with no evidence of macrophase separation (Figures 3.6 and 3.7). Nitrogen sorption experiments gave type IV isotherms with H2 hysteresis, characteristic of disordered mesoporous materials (Figure 3.8).[31] These data are similar to that obtained in monoliths prepared without any PEO (Figure 3.9).[23] However, increasing the PEO content leads to increased swelling of the PLA domains, as evidenced by an increase in mean pore size for the corresponding etched samples. Mesopore size distributions were estimated based on a quenched solid density functional theory (QSDFT) kernel applied to the adsorption branch using a cylindrical pore model (Figure 3.6).[32] The average pore sizes are 7, 11, 14, and 17 nm, and the specific surface areas, based on Brunauer-Emmett-Teller (BET) analysis, are 220, 134, 120, and 88 m^2 g^{-1} for monoliths derived from 0, 30, 50, and 70 vol% PEO, respectively.[33] Independent of the amount of added 5 kg mol^{-1} PEO, the microphase-separated structure is trapped via in situ cross-linking. This affords control over mesopore size, and accesses pore sizes larger than those prepared without any additive using a single PLA-CTA,[23] which is desirable for applications requiring tailored size selectivity.[34]

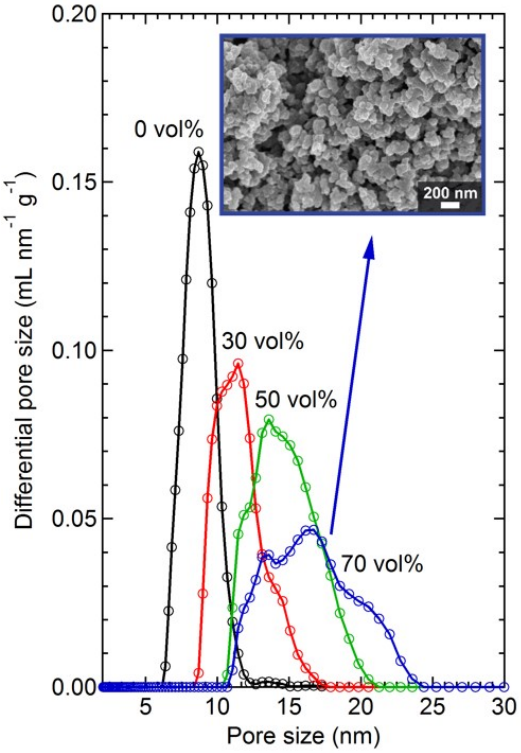

Figure 3.6. Mesopore size distributions based on QSDFT analysis of the adsorption branch for monoliths prepared with different volume fractions of 5 kg mol^{-1} PEO additive. Inset: SEM micrograph of an etched monolith prepared with 70 vol% of 5 kg mol^{-1} PEO additive. The sample was coated with ~3 nm of Pt prior to imaging.

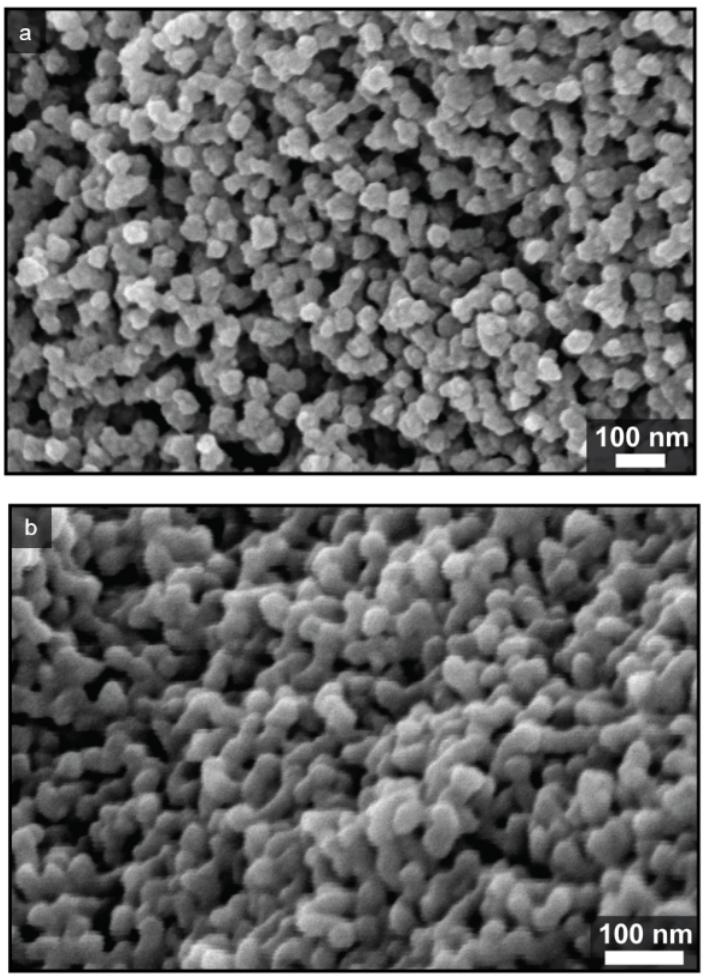

Figure 3.7 SEM micrographs of etched monoliths derived from (a) 30 and (b) 50 vol% of 5 kg mol^{-1} PEO additive.

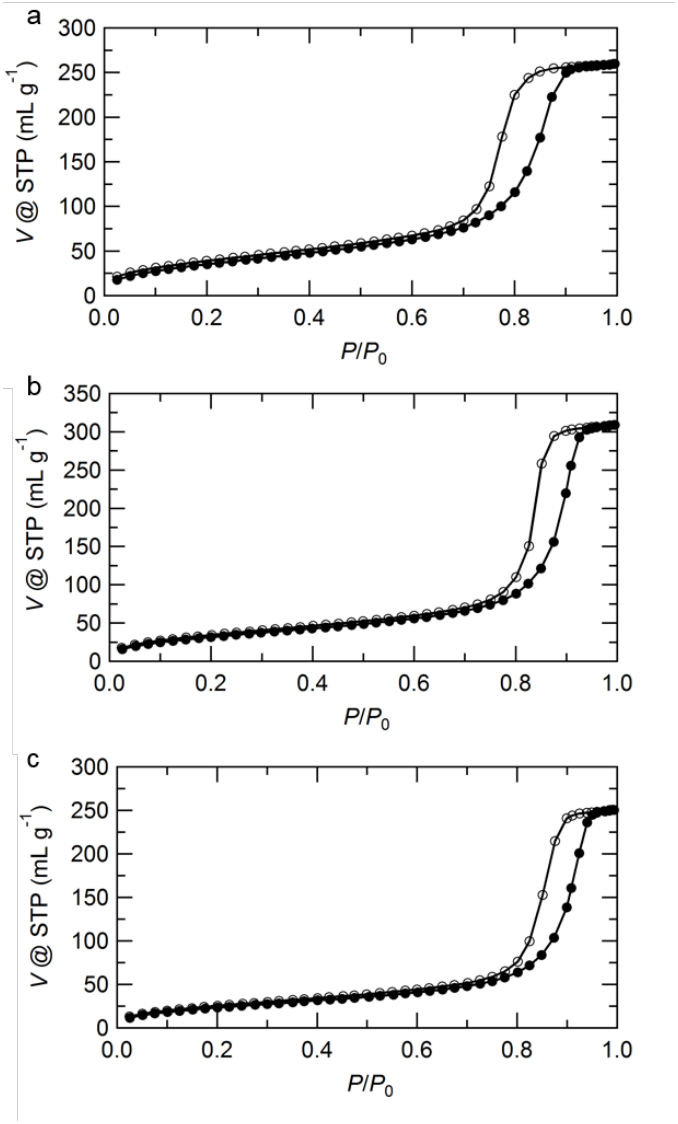

Figure 3.8. Nitrogen sorption isotherms for monoliths derived from 5 kg mol^{-1} PEO additive at (a) 30 (b) 50 and (c) 70 vol%. The BET specific surface areas are (a) 134, (b) 120, and (c) 88 $m^2 g^{-1}$. Filled circles indicate nitrogen adsorption and empty circles indicate desorption.

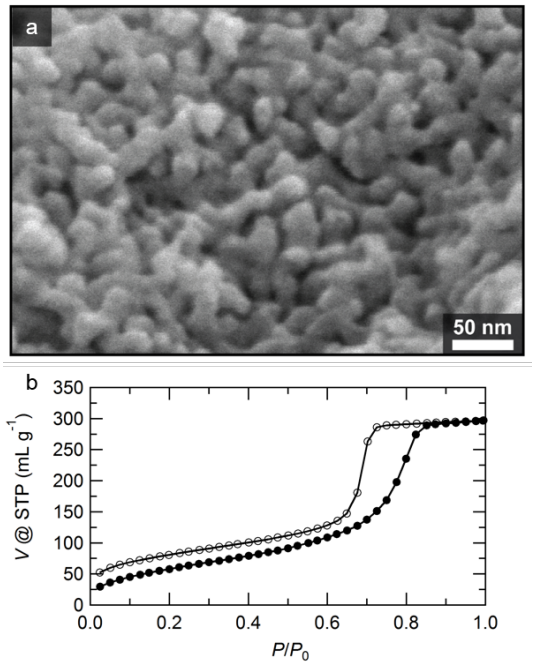

Figure 3.9. (a) SEM micrograph and (b) nitrogen sorption isotherm of an etched monolith prepared in the absence of PEO additive. The BET specific surface area is 220 m^2 g^{-1}. Filled circles indicate nitrogen adsorption and empty circles indicate desorption.

3.3.3 Moderate Molar Mass PEO

Increasing the molar mass of the PEO additive to 20 kg mol^{-1} at 30 vol% results in both macro- and microphase separation. SEM micrographs suggest that the structure contains isolated macropores that are accessible through a percolating mesoporous network (Figure 3.10a,b, and 3.11), which is consistent with the opaque white appearance of the sample due to the scattering of visible light. Hierarchical porosity was further confirmed by nitrogen sorption analysis (Figure 3.10c). The hysteresis step at P/P_0 = 0.75–0.90 is associated with capillary condensation and evaporation in the mesopores, and the step at P/P_0 > 0.98 indicates the filling of macropores. This monolith has a BET specific surface area of 115 m^2 g^{-1} and a QSDFT average pore size of 11 nm, consistent with other related

mesoporous polymeric materials.[23] Further increasing the 20 kg mol^{-1} PEO additive to 50 vol% resulted in an increase in the apparent connectivity of the macropores, which is consistent with the increase in volume fraction of the pore-forming component (Figure 3.12). The mesostructure was retained in this monolith as well, with a QSDFT average pore size of 11 nm and a BET specific surface area of 103 m^2 g^{-1}. The cross-linked polymer formed a globular structure with macropores composed of voids between the globules, and mesopores located within the globules. Interestingly, this globular morphology is often observed when the nonreactive additive is a small molecule.[35]

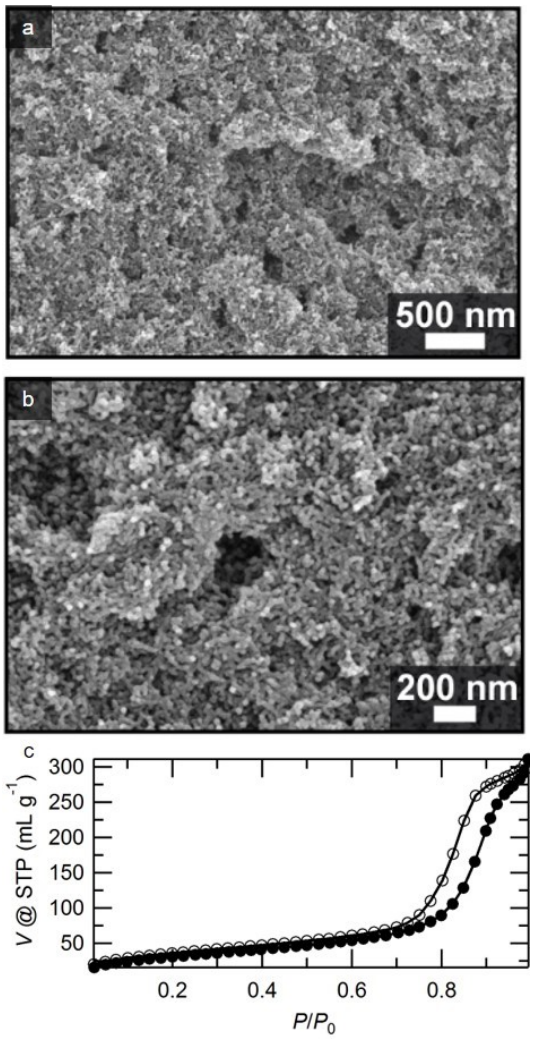

Figure 3.10. SEM micrographs at (a) 25,000× and (b) 50,000× magnification and (c) nitrogen sorption isotherm of an etched monolith prepared with 30 vol% of 20 kg mol^{-1} PEO additive. Filled circles indicate adsorption and empty circles indicate desorption.

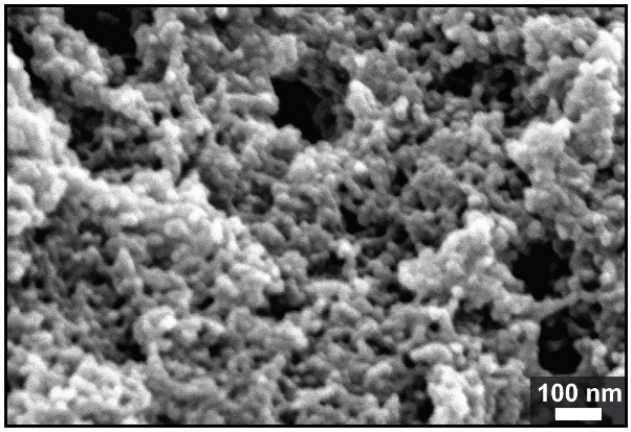

Figure 3.11. SEM micrograph of a monolith derived from 30 vol% 20 kg mol^{-1} PEO after soaking for 18 h in deionized water.

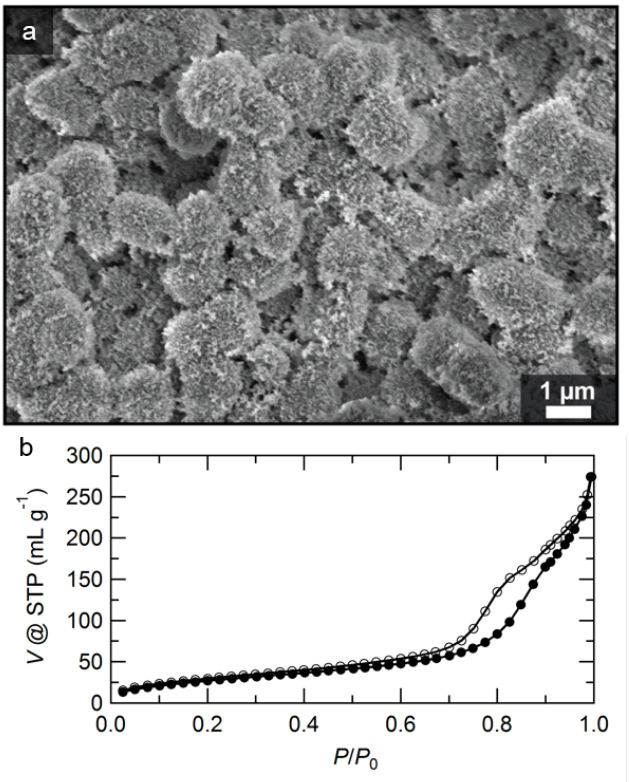

Figure 3.12. (a) SEM micrograph and (b) nitrogen sorption isotherm for an etched monolith derived from 50 vol% 20 kg mol^{-1} PEO additive. The monolith has a BET specific surface area of 102 m^2 g^{-1}. Filled circles indicate adsorption and empty circles indicate desorption.

3.3.4 High Molar Mass PEO

Further increasing the molar mass of the PEO additive to 35 kg mol^{-1} resulted in a dramatic morphological change. Macropores with sizes on the order 0.1–0.3 μm were observed along with mesopores in the macroporous framework (Figures 3.13, 3.14, 3.15). The BET specific surface areas are 93 and 77 m^2 g^{-1} for 30 and 50 vol% of 35 kg mol^{-1} PEO additive, respectively. Both monoliths have QSDFT average pore sizes of 10 nm. The residual PEO content in a monolith prepared in the presence of 50 vol% of 35 kg mol^{-1} PEO was determined by ^{1}H NMR spectroscopy after immersing the etched monolith in deuterated chloroform with an internal standard. This process extracted the residual 11 ± 1 wt% PEO (Figure 3.16). Additionally, macrophase separation of the PEO from the diblock was confirmed by soaking a monolith in deionized water without added base. This resulted in a monolith with only macropores and a much lower BET specific surface area of 23 m^2 g^{-1} (Figure 3.17).

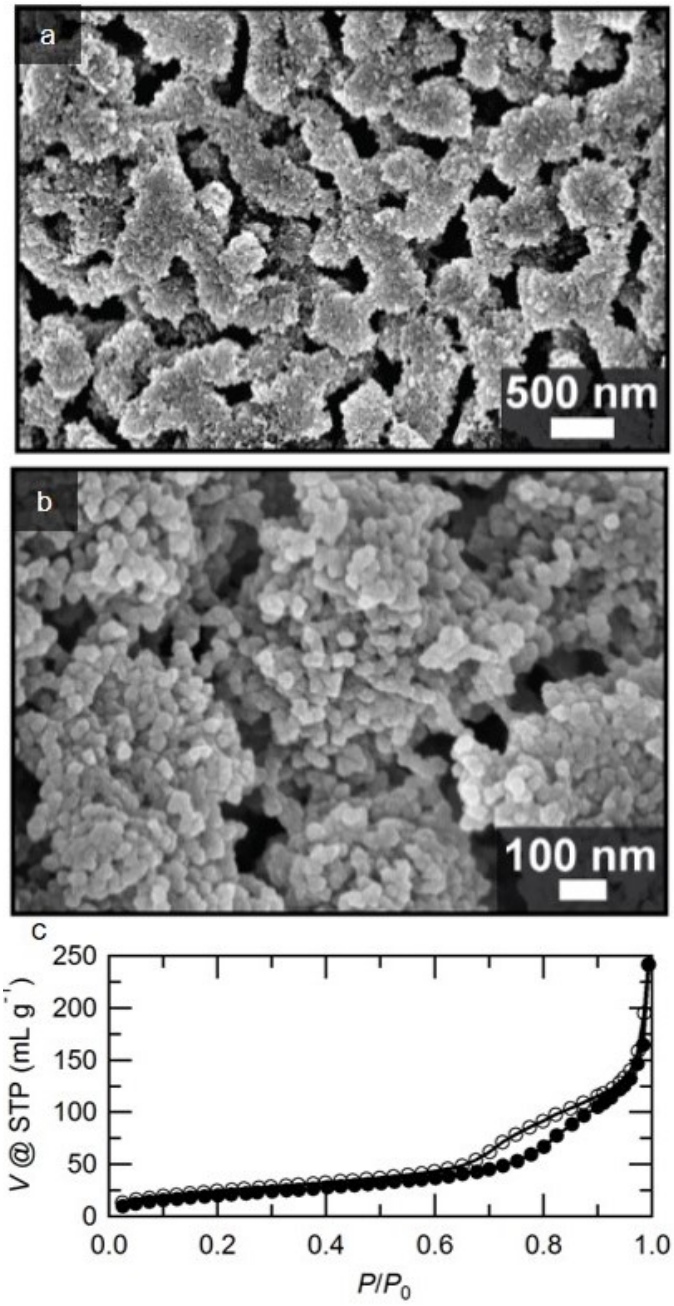

Figure 3.13. Morphology of a hierarchically porous polymer after etching, derived from a monolith prepared with 50 vol% of 35 kg mol^{-1} PEO additive. SEM micrographs at magnifications of (a) 25,000× and (b) 90,000×, and (c) the corresponding nitrogen sorption isotherm. The filled circles correspond to the adsorption branch, and the empty circles to the desorption branch.

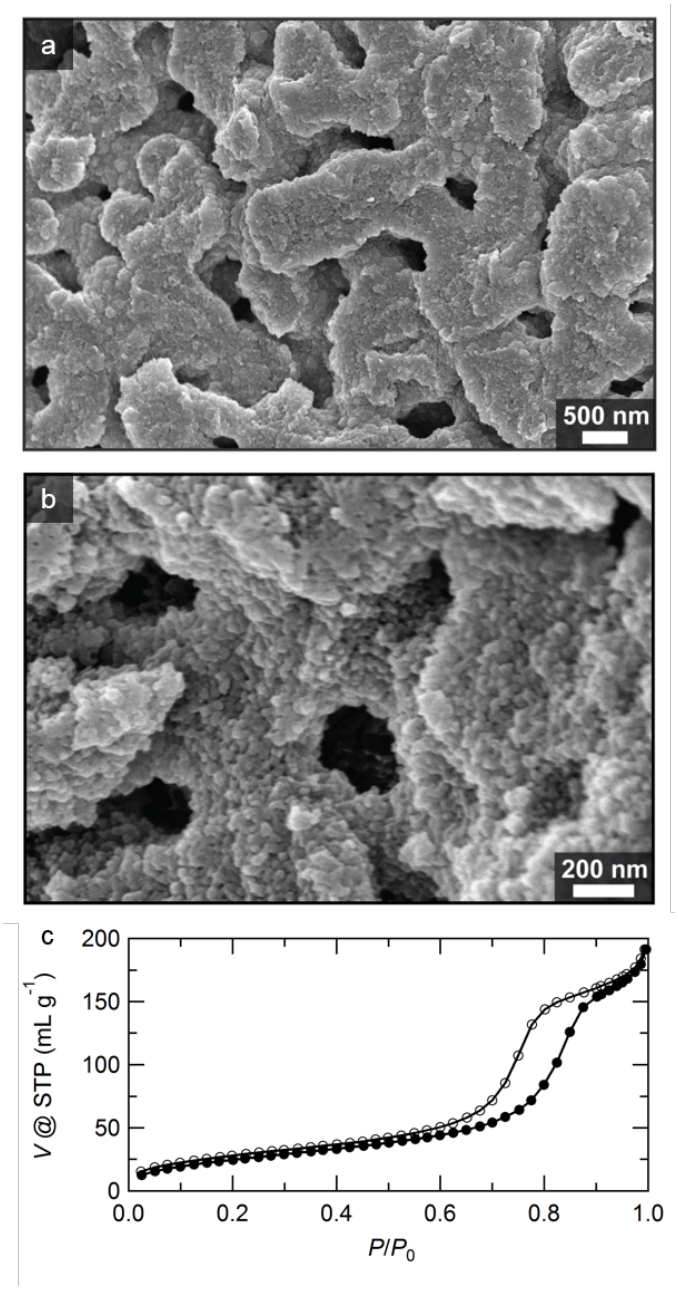

Figure 3.14. SEM micrographs at (a) 18,000× and (b) 60,000× magnification and (c) nitrogen sorption isotherm of an etched monolith derived from 30 vol% 35 kg mol^{-1} PEO additive. Filled circles indicate adsorption and empty circles indicate desorption.

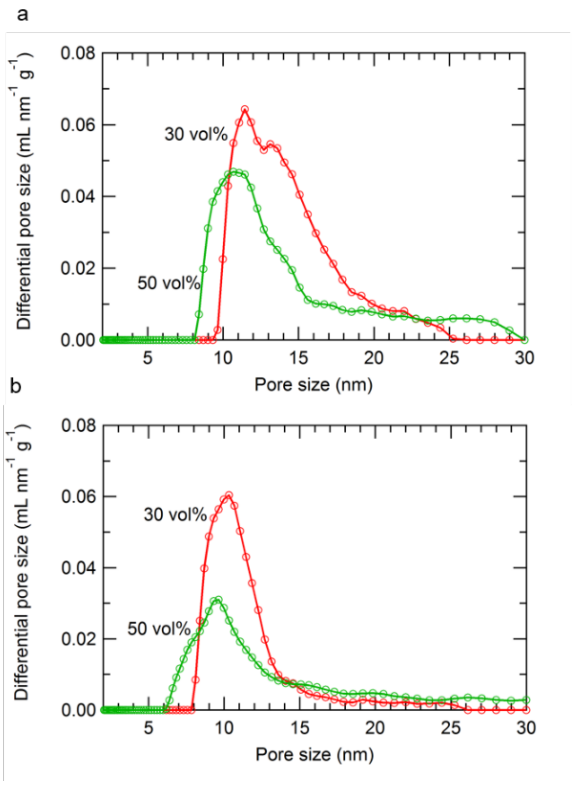

Figure 3.15. Mesopore size distributions based on QSDFT analysis of the adsorption branch for etched monoliths derived from (a) 20 kg mol^{-1} and (b) 35 kg mol^{-1} PEO additive.

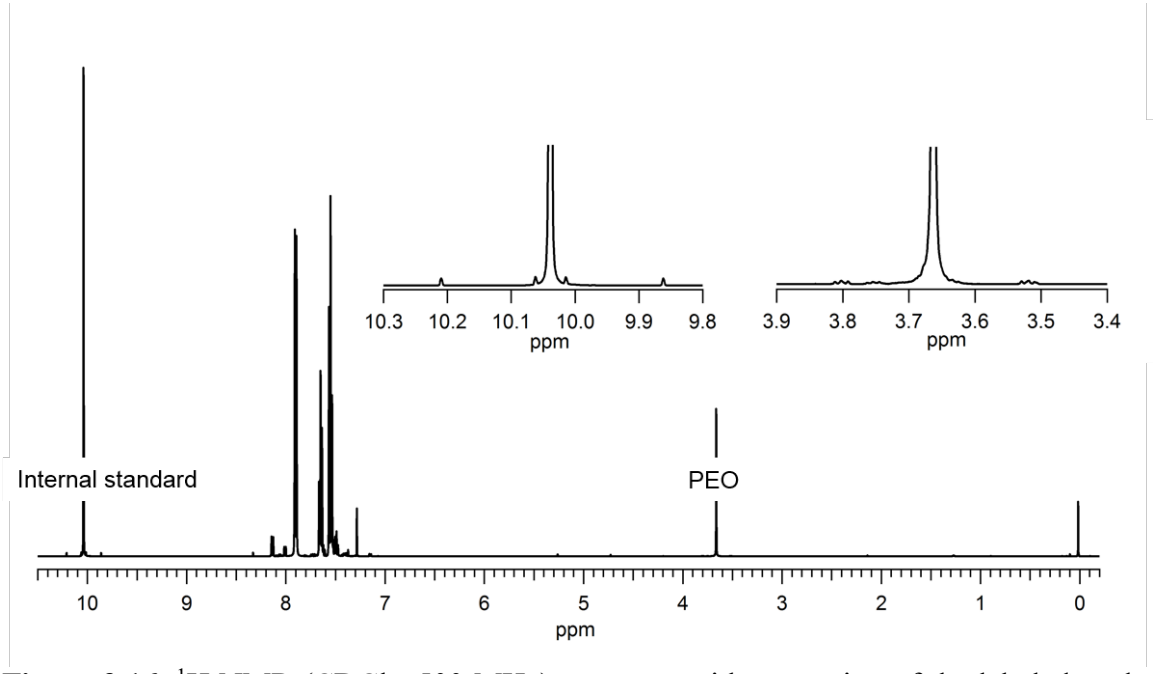

Figure 3.16. ^{1}H NMR ($CDCl_3$, 500 MHz) spectrum with expansion of the labeled peaks (insets) obtained by soaking a portion of an etched monolith (derived from 50 vol% 35 kg mol^{-1} PEO) in $CDCl_3$ for 16 h. The residual PEO content is 11 ± 1 wt%. Benzaldehyde was used as an internal standard.

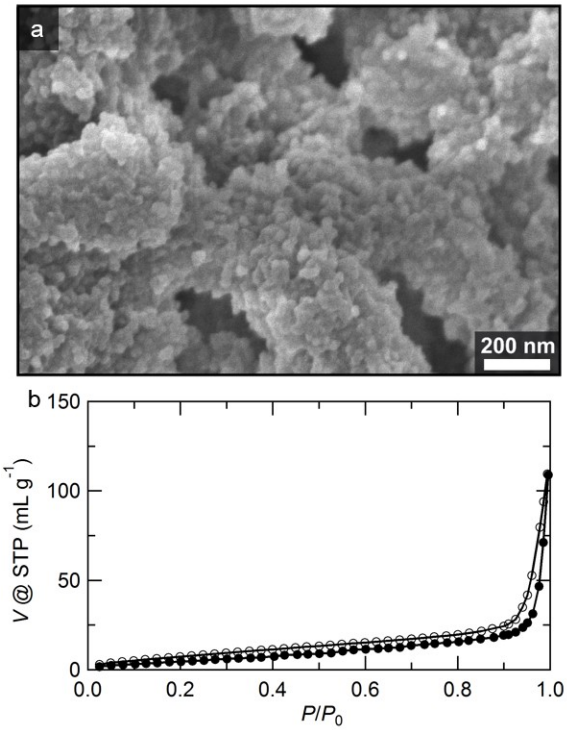

Figure 3.17. (a) SEM micrograph and (b) nitrogen sorption isotherm of a monolith derived from 50 vol% 35 kg mol^{-1} PEO after soaking for 18 h in deionized water. The monolith has a BET specific surface area of 23 m^2 g^{-1}. Filled circles indicate adsorption and empty circles indicate desorption.

We further analyzed a monolith derived from 50 vol% 35 kg mol^{-1} PEO to determine the continuity of the macropores. Based on gravimetric analysis, the majority of the PEO was removed during etching, which suggests that the majority of the macropores are accessible to water. The accessibility of the macropores was confirmed by time-resolved impedance spectroscopy (Figure 3.18). Bulk impedance measurements were made periodically over the course of 70 h on precursor monoliths exposed to 1.0 mM KCl aqueous solution. The data were then fit to obtain bulk resistance. The high initial resistance (> 1 MΩ) is due to the hindrance of electrical charge transfer across the dense nonporous monolith. Over time, the resistance drops as the PEO is extracted and the

macropores are formed, and reaches a constant value of 610 kΩ (reproducibility ± 14 kΩ) after approximately 8 h. The resistance of the monolith was comparable to that of a nanoporous glass plug with a percolating pore network and identical dimensions (372 kΩ when filled with 1.0 mM KCl).[36,37]

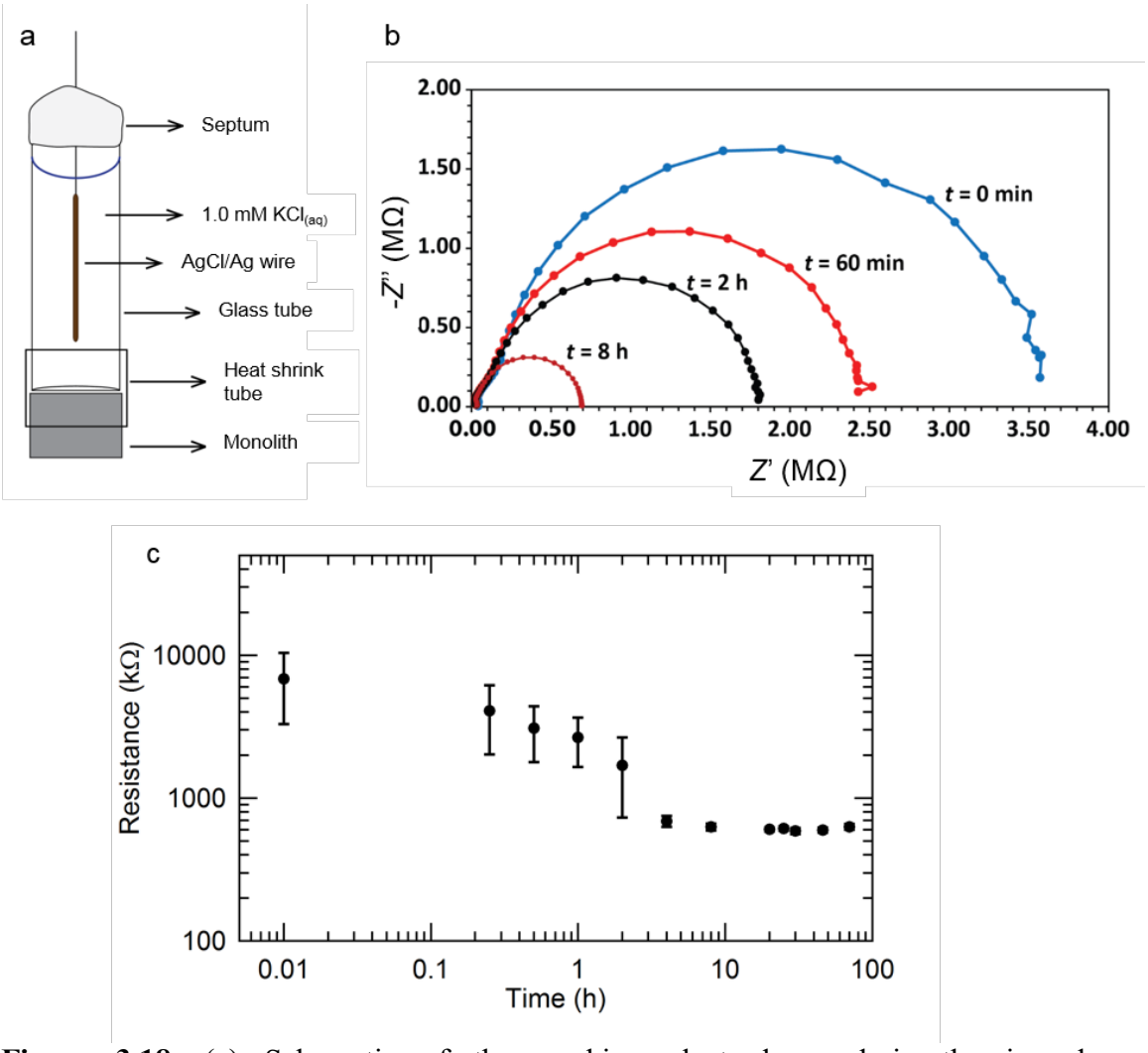

Figure 3.18. (a) Schematic of the working electrode used in the impedance measurements. (b) Representative impedance spectra of a precursor monolith at different time points of exposure to 1.0 mM KCl aqueous solution. (c) Resistance as a function of time, as obtained from the impedance measurements by fitting of the semicircle feature with a parallel R||C element. All measurements represent averages and standard deviations for three monoliths derived from 50 vol% 35 kg mol^{-1} PEO. The error bars for the last six data points are beneath the markers. The resistance decreases as the PEO is leaving the monolith and the macropores are formed.

3.4 Conclusions

In this work, we have discovered a route to mesoporous and hierarchically meso- and macroporous polymer monoliths with tunable morphology and controllable pore size by combining macro- and microphase separation. The nanostructures were characterized by SAXS, SEM, and nitrogen sorption, and the wettability of the monoliths is well suited for applications in aqueous solution. The starting materials are readily available, and the synthetic ease is advantageous. We have now attained a unique combination of control over pore size and synthetic simplicity in the production of hierarchically porous monoliths with large pores and high surface area. We envision that such structures could be useful in applications requiring both rapid mass transport and selectivity.

3.5 References

1) Hjertén, S.; Liao, J.-L.; Zhang, R. High-Performance Liquid Chromatography on Continuous Polymer Beds. *J. Chromatogr.* **1989**, *473*, 273–275.

2) Svec, F.; Fréchet, J. M. J. Continuous Rods of Macroporous Polymer as High-Performance Liquid Chromatography Separation Media. *Anal. Chem.* **1992**, *64*, 820–822.

3) Shintani, Y.; Zhou, X.; Furuno, M.; Minakuchi, H.; Nakanishi, K. Monolithic Silica Column for In-Tube Solid-Phase Microextraction Coupled to High-Performance Liquid Chromatography. *J. Chromatogr. A* **2003**, *985*, 351–357.

4) Sinner, F.; Buchmeiser, M. R. A New Class of Continuous Polymer Supports Prepared by Ring-Opening Metathesis Polymerization: A Straightforward Route to Functionalized Monoliths. *Macromolecules* **2000**, *33*, 5777–5786.

5) Bronstein, L. M.; Goerigk, G.; Kostylev, M.; Pink, M.; Khotina, I. A.; Valetsky, P. M.; Matveeva, V. G.; Sulman, E. M.; Sulman, M. G.; Bykov, A. V.; Lakina, N. V.; Spontak, R. J. Structure and Catalytic Properties of Pt-Modified Hyper-Cross-Linked Polystyrene Exhibiting Hierarchical Porosity. *J. Phys. Chem. B* **2004**, *108*, 18234–18242.

6) He, L.; Zhang, Y.; Zeng, C.; Ngiam, M.; Liao, S.; Quan, D.; Zeng, Y.; Lu, J.; Ramakrishna, S. Manufacture of PLGA Multiple-Channel Conduits with Precise Hierarchical Pore Architectures and In Vitro/Vivo Evaluation for Spinal Cord Injury. *Tissue Eng. Part C- Methods* **2009**, *15*, 243–255.

7) Mulvenna, R. A.; Weidman, J. L.; Jing, B.; Pople, J. A.; Zhu, Y.; Boudouris, B. W.; Phillip, W. A. Tunable Nanoporous Membranes with Chemically-Tailored Pore Walls from Triblock Polymer Templates. *J. Memb. Sci.* **2014**, *470*, 246–256.

8) Li, L.; Schulte, L.; Clausen, L. D.; Hansen, K. M.; Jonsson, G. E.; Ndoni, S. Gyroid Nanoporous Membranes with Tunable Permeability. *ACS Nano* **2011**, *5*, 7754–7766.

9) Taguchi, A.; Smätt, J. H.; Lindén, M. Carbon Monoliths Possessing a Hierarchical, Fully Interconnected Porosity. *Adv. Mater.* **2003**, *15*, 1209–1211.

10) Wang, Z.; Li, F.; Ergang, N. S.; Stein, A. Effects of Hierarchical Architecture on Electronic and Mechanical Properties of Nanocast Monolithic Porous Carbons and Carbon-Carbon Nanocomposites. *Chem. Mater.* **2006**, *18*, 5543–5553.

11) Liang, C.; Dai, S. Dual Phase Separation for Synthesis of Bimodal Meso-/Macroporous. *Chem. Mater.* **2009**, *21*, 2115–2124.

12) Minakuchi, H.; Nakanishi, K.; Soga, N.; Ishizuka, N.; Tanaka, N. Octadecylsilylated Porous Silica Rods as Separation Media for Reversed-Phase Liquid Chromatography. *Anal. Chem.* **1996**, *68*, 3498–3501.

13) Smått, J.-H.; Weidenthaler, C.; Rosenholm, J. B.; Linde, M. Hierarchically Porous Metal Oxide Monoliths Prepared by the Nanocasting Route. *Chem. Mater.* **2006**, *18*, 1443–1450.

14) Seo, M.; Kim, S. S.; Oh, J.; Kim, S. S.; Hillmyer, M. A. Hierarchically Porous Polymers from Hyper-Cross-Linked Block Polymer Precursors. *J. Am. Chem. Soc.* **2015**, *137*, 600–603.

15) Maya, F.; Svec, F. A New Approach to the Preparation of Large Surface Area Poly(styrene-*co*-divinylbenzene) Monoliths via Knitting of Loose Chains Using External Crosslinkers and Application of These Monolithic Columns for Separation of Small Molecules. *Polymer.* **2014**, *55*, 340–346.

16) Valkama, S.; Nykänen, A.; Kosonen, H.; Ramani, R.; Tuomisto, F.; Engelhardt, P.; Ten Brinke, G.; Ikkala, O.; Ruokolainen, J. Hierarchical Porosity in Self-Assembled Polymers: Post-Modification of Block Copolymer-Phenolic Resin Complexes by

Pyrolysis Allows the Control of Micro- and Mesoporosity. *Adv. Funct. Mater.* **2007**, *17*, 183–190.

17) Jones, B. H.; Lodge, T. P. Hierarchically Structured Materials from Block Polymer Confinement within Bicontinuous Microemulsion-Derived Nanoporous Polyethylene. *ACS Nano* **2011**, *5*, 8914–8927.

18) Li, Y.; Tolley, H. D.; Lee, M. L. Size-Exclusion Separation of Proteins Using a Biocompatible Polymeric Monolithic Capillary Column with Mesoporosity. *J. Chromatogr. A* **2010**, *1217*, 8181–8185.

19) Lubbad, S. H.; Buchmeiser, M. R. Highly Cross-Linked Polymeric Capillary Monoliths for the Separation of Low, Medium, and High Molecular Weight Analytes. *J. Sep. Sci.* **2009**, *32*, 2521–2529.

20) Sai, H.; Tan, K. W.; Hur, K.; Asenath-Smith, E.; Hovden, R.; Jiang, Y.; Riccio, M.; Muller, D. A.; Elser, V.; Estroff, L. A.; Gruner, S. M.; Wiesner, U. Hierarchical Porous Polymer Scaffolds from Block Copolymers. *Science* **2013**, *341*, 530–534.

21) Hess, S. C.; Kohll, A. X.; Raso, R. A.; Schumacher, C. M.; Grass, R. N.; Stark, W. J. Template-Particle Stabilized Bicontinuous Emulsion Yielding Controlled Assembly of Hierarchical High-Flux Filtration Membranes. *ACS Appl. Mater. Interfaces* **2015**, *7*, 611–617.

22) Bolton, J.; Bailey, T. S.; Rzayev, J. Large Pore Size Nanoporous Materials from the Self-Assembly of Asymmetric Bottlebrush Block Copolymers. *Nano Lett.* **2011**, *11*, 998–1001.

23) Seo, M.; Hillmyer, M. A. Reticulated Nanoporous Polymers by Controlled Polymerization-Induced Microphase Separation. *Science.* **2012**, *336*, 1422–1425.

24) Schulze, M. W.; McIntosh, L. D.; Hillmyer, M. A.; Lodge, T. P. High-Modulus, High-Conductivity Nanostructured Polymer Electrolyte Membranes via Polymerization-Induced Phase Separation. *Nano Lett.* **2014**, *14*, 122–126.

25) McIntosh, L. D.; Schulze, M. W.; Irwin, M. T.; Hillmyer, M. A; Lodge, T. P. Evolution of Morphology, Modulus, and Conductivity in Polymer Electrolytes Prepared via Polymerization-Induced Phase Separation. *Macromolecules* **2015**, *48*, 1418–1428.

26) Viklund, C.; Svec, F.; Fréchet, J. M. J.; Irgum, K. Monolithic, "Molded", Porous Materials with High Flow Characteristics for Separations, Catalysis, or Solid-Phase Chemistry: Control of Porous Properties during Polymerization. *Chem. Mater.* **1996**, *8*, 744–750.

27) Moravcová, D.; Jandera, P.; Planeta, J.; Urban, J.; Planeta, J. Characterization of Polymer Monolithic Stationary Phases for Capillary HPLC. *J. Sep. Sci.* **2003**, *26*, 1005–1016.

28) Kanamori, K.; Hasegawa, J.; Nakanishi, K.; Hanada, T. Facile Synthesis of Macroporous Cross-Linked Methacrylate Gels by Atom Transfer Radical Polymerization. *Macromolecules* **2008**, *41*, 7186–7193.

29) Mao, H.; Hillmyer, M. A. Morphological Behavior of Polystyrene-*block*-Polylactide/Polystyrene-*block*-Poly(ethylene oxide) Blends. *Macromol. Chem. Phys.* **2008**, *209*, 1647–1656.

30) Roe, R.J.; Nojima, S. Small-Angle X-Ray Scattering Study of Micro- and Macro-Phase Separations in Blends of Block Copolymer with Homopolymer. *Mater. Res. Soc. Symp. Proc.* **1987**, *79*, 151–158.

31) Lowell, S.; Shields, J. E.; Thomas, M. A.; Thommes, M. Characterization of Porous Solids and Powders: Surface Area, Pore Size and Density; Scarlett, B., Ed.; Kluwer Academic Publishers: Norwell, MA, **2004**; pp. 13, 44.

32) Gor, G. Y.; Thommes, M.; Cychosz, K. A.; Neimark, A. V. Quenched Solid Density Functional Theory Method for Characterization of Mesoporous Carbons by Nitrogen Adsorption. *Carbon* **2012**, *50*, 1583–1590.

33) Brunauer, S.; Emmett, P. H.; Teller, E. Adsorption of Gases in Multimolecular Layers. *J. Am. Chem. Soc.* **1938**, *60*, 309–319.

34) Viklund, C.; Nordström, A.; Irgum, K.; Svec, F.; Fréchet, J. M. J. Preparation of Porous Poly (styrene-*co*-divinylbenzene) Monoliths with Controlled Pore Size Distributions Initiated by Stable Free Radicals and Their Pore Surface Functionalization by Grafting. *Macromolecules* **2001**, *34*, 4361–4369.

35) Barlow (née Tan), K. J.; Hao, X.; Hughes, T. C.; Hutt, O. E.; Polyzos, A.; Turner, K. A.; Moad, G. Porous, Functional, Poly(styrene-*co*-divinylbenzene) Monoliths by RAFT Polymerization. *Polym. Chem.* **2014**, *5*, 722–732.

36) Mousavi, M. P. S.; Bühlmann, P. Reference Electrodes with Salt Bridges Contained in Nanoporous Glass: An Underappreciated Source of Error. *Anal. Chem.* **2013**, *85*, 8895–8901.

37) CoralPor Porous Glass Product Information. http://www.us.schott.com/SCHOTT. Accessed on May 8, 2015.

Chapter 4. Effect of Homopolymer in Polymerization-Induced Microphase Separation Process[2]

The work in this chapter was done in collaboration with Prof. Myungeun Seo and Jongmin Park at KAIST, South Korea.

4.1 Introduction

Bicontinuous polymeric nanostructures, which are comprised of two interpenetrating domains, are fascinating materials. Such nanostructured polymers can serve as versatile precursors, for example, in the generation of porous polymers possessing a three-dimensionally (3D) continuous pore structure by selective removal of one of the domains.[1–3] As exploiting the 3D continuous pore structure is beneficial for applications requiring mass transport, these nanostructured polymers have demonstrated utility in areas including filtration,[4] separation,[5] and templating.[6]

Microphase separation of block polymers provides a powerful methodology towards the formation of mesoporous (pore size of 10 – 50 nm) polymers.[6] Here, a covalent junction between the blocks prevents macrophase separation and the length scale of the resulting

---

[2]Reprinted from Park, J.; Saba, S. A.; Hillmyer, M. A.; Kang, D.-C.; Seo, M. Effect of Homopolymer in Polymerization-Induced Microphase Separation Process. *Polymer* **2017**, DOI:10.1016/j.polymer.2017.04.046. Copyright 2017, with permission from Elsevier.

microphase-separated structure is dictated by the molar mass of the blocks, which allows robust control over pore size. The gyroid phase is a well-known example of a bicontinuous structure appearing in the phase diagram of diblock copolymers. 3D continuous mesoporous polymers have been successfully derived from the selective etching of a microphase-separated gyroid precursor, however the narrow stability window of the gyroid phase often requires challenging syntheses.[7–10] Polymer-based bicontinuous structures can also be obtained by appropriately blending two homopolymers with the corresponding diblock copolymer, which produces a bicontinuous microemulsion.[11] The disordered bicontinuous structure can be rendered porous and used as a template, but the domain size falls in the macroporous regime (ca. 100 nm).[12]

Polymerization-induced microphase separation (PIMS) is an alternative and facile method to generate a cross-linked block polymer precursor with a disordered bicontinuous morphology, which is topologically comparable to the structures obtained via spinodal decomposition.[2] In this method, the bulk reversible addition-fragmentation chain transfer (RAFT) copolymerization of styrene (S) and divinylbenzene (DVB) in the presence of poly(lactide) macro-chain transfer agent (PLA-CTA) formed PLA-*b*-P(S-*co*-DVB), where in situ cross-linking arrested the emergent bicontinuous structure. Subsequent selective etching of PLA produced robust mesoporous P(S-*co*-DVB) with 3D continuous pore structure and tunable pore size from 4 to 8 nm (based on Barrett–Joyner–Halenda, BJH, analysis[13] of nitrogen sorption isotherms). The versatility of the

PIMS approach has been demonstrated with other block polymer systems[14–16] and combined with other nanostructuring methods to produce hierarchically porous structures.[17,18]

We note that PIMS can be considered an analogue of the widely studied polymerization-induced phase separation (PIPS) process in which copolymerization of a monomer with a cross-linker in the presence of a nonreactive porogen induces macrophase separation at a critical conversion.[19–22] The formation of 3D continuous pore structure via PIPS has been successfully demonstrated, in particular with controlled radical polymerizations.[23–30] The porogens can be small molecules or homopolymers that are miscible with the monomers but immiscible with the growing polymer. Again, removal of the porogen results in macroporous polymers. While both PIMS and PIPS offer synthetic simplicity for the generation of disordered bicontinuous morphologies, crucially, the in situ formation of a block polymer via RAFT mechanism in the PIMS process limits the length scale of the emergent structure to much smaller dimensions than are accessible via the macrophase separation process of PIPS.

Inspired by this, we explored the transition of PIMS to PIPS by copolymerization of S and DVB from PLA-CTA in the presence hydroxyl terminated PLA (PLA-OH) homopolymer which lacks the CTA moiety and serves as a nonreactive porogen during polymerization. The addition of an additive that selectively swells a single domain of a self-assembled block polymer may cause an increase in the domain size of the swollen

block.[31–33] This selective swelling strategy has been applied to PIMS materials as well.[14,15] If the amount of the additive is larger than that can be accommodated in the microdomain, macrophase separation can occur.[3] This is the case when PLA-miscible poly(ethylene oxide) (PEO) homopolymer is added to the polymerization mixture of S, DVB, and PLA-CTA. The molar mass of PEO greatly affects whether it selectively swells the PLA microdomain or induce simultaneous macro- and microphase separation.[18]

Here, by adjusting the ratio of PLA-CTA to PLA-OH, we show that we can indeed control the characteristic length scale of the cross-linked bicontinuous precursor and the corresponding porous polymer, spanning three orders of magnitude from nanometer to micrometer pore sizes. Our data suggests that at low loadings of PLA-OH, the PLA-OH tends to swell the PLA microdomain formed by PIMS opening a route to systematic control of pore size in the mesoporous regime by varying the ratio of PLA homopolymer to PLA-CTA. However, at higher loadings of PLA-OH macrophase separation occurs as the solubility limit of PLA-OH in the PLA microdomain is exceeded. We also show that maintaining a constant concentration of CTA, through the addition of molecular CTA that does not contain PLA into the polymerization mixture, drives the system towards PIPS due to formation of P(S-*co*-DVB) homopolymer in the early stages of polymerization. This allows for the formation of macroporous polymers with improved control over pore size in the macroporous regime while addition of PLA-OH without the molecular CTA offers more precise tuning in the mesoporous regime. While a similar

result could be achieved by continually increasing the molar mass of PLA-CTA to access larger pore sizes via the PIMS process, this method is not entirely practical due to synthetic difficulties and inherently high viscosities of such polymerization mixtures.[2] Instead, the methodology presented herein can provide a useful means of controlling pore sizes via PIMS. Finally, by increasing the molar mass and the overall volume fraction of PLA homopolymer in the polymerization mixture, we demonstrate that PIMS and PIPS can occur simultaneously resulting in a hierarchical structure which can be readily converted into a hierarchically meso- and macroporous polymer.

4.2 Experimental Methods

The chemical structures of the materials used in this study are depicted in Scheme 4.1 and the molecular characteristics of the polymers are summarized in Table 4.1. The polymerization mixtures consisting of PLA-CTA, PLA-OH, molecular CTA (CTA-1 or CTA-2), S and DVB ([S]:[DVB] = 4:1) were prepared over a range of compositions. In the first series of samples, the total weight fraction of PLA in the polymerization mixture (w_{PLA}, where $w_{PLA} = w_{PLA\text{-}OH} + w_{PLA\text{-}CTA}$) was fixed at 0.3 while the ratio of PLA-OH to PLA-CTA (r_H, where $r_H = w_{PLA\text{-}OH}/w_{PLA}$) was varied (Table 4.2 and Section 4.3.1). A second series of samples was prepared identical to the first series except that additional molecular CTA was added in order to maintain constant [CTA] = 0.021 M in the polymerization mixture (Table 4.3 and Section 4.3.2). A third series of samples was designed to access porous polymers with high void fractions or hierarchically porous polymers containing meso- and macropores (Table 4.4 and Section 4.3.3). This is

achieved by increasing w_{PLA} and by varying the molar mass ratio of PLA-CTA to PLA-OH in the polymerization mixture. The molar mass ratio was denoted as $\alpha = M_{w,PLA\text{-}OH}/M_{w,PLA\text{-}CTA}$ following the literature notation, where M_w denotes the absolute weight-average molar mass as determined by SEC with multi-angle laser light scattering detection. [34]

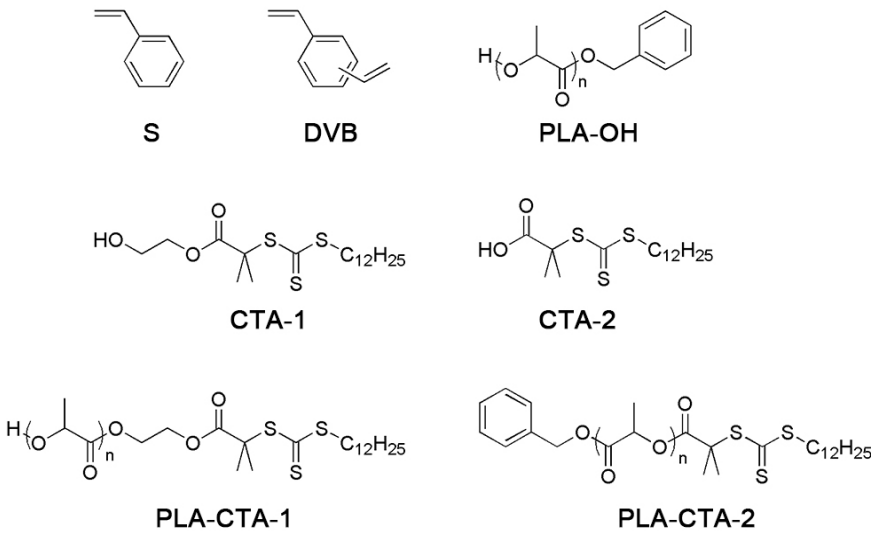

Scheme 4.1. Chemical structures of the materials used in this study.

Table 4.1. Characterization of PLA-OH and PLA-CTA

	$M_{n,NMR}$ (kg mol^{-1})[a]	$M_{w,SEC}$ (kg mol^{-1})[b]	$Đ$[b]
PLA-OH	16	18	1.08
	10	11	1.03
	29	32	1.04
	68.5	70	1.1
PLA-CTA-1	19	17	1.06
PLA-CTA-2	34	35	1.08

[a]Determined by ^{1}H NMR end group analysis. [b]M_w determined by THF-SEC analysis with light scattering detection using a dn/dc of 0.049 mL g^{-1}.

Table 4.2. Composition of the cross-linked precursors prepared in Series 1

r_H	PLA-CTA (wt%)[a]	PLA-OH (wt%)[b]	Mass yield (%)	Mass loss after PLA etching (%)
0	30	0	95.8	37.4
0.1	27	3	102.0	36.8
0.2	24	6	97.33	36.5
0.3	21	9	99.4	36.7
0.4	18	12	105.4	35.2
0.5	15	15	100.8	36.1
0.6	12	18	98.5	36.0
0.7	9	21	101.6	34.8
0.8	6	24	100.8	36.7
0.9	3	27	99.5	39.5
0.92	2.4	27.6	54.6	61.2
0.94	1.8	28.1	53.4	60.4
0.96	1.2	28.8	48.1	62.6
0.98	6	29.4	46.1	72.8
1	0	29.7	89.8	38.4

[a]$M_{w,PLA\text{-}CTA}$ = 17 kg mol^{-1}. [b]$M_{w,PLA\text{-}OH}$ = 18 kg mol^{-1}

Table 4.3. Composition of the cross-linked precursors prepared in Series 2

r_H	PLA-CTA (wt%)[a]	PLA-OH (wt%)[b]	x_{CTA-1} (mol%)	Mass yield (%)	Mass loss after PLA etching (%)
0.2	24	6	20	96.9	38.4
0.4	18	12	40	95.3	40.2
0.6	12	18	60	95.9	40.8
0.7	9	21	70	95.2	41.2
0.8	6	24	80	912	39.3
0.9	3	27	90	91.8	42.5
1	0	30	100	94.6	39.3

[a]$M_{w,PLA-CTA}$ = 17 kg mol^{-1}. [b]$M_{w,PLA-OH}$ = 20 kg mol^{-1}

Table 4.4. Composition of the cross-linked precursors prepared in Series 3

(r_H, α)	PLA-CTA (wt%)	PLA-OH (wt%)	Mass yield (%)	Mass loss after PLA etching (%)
(0.59, 0.3)	21	35	95.2	55.6
(0.78, 0.3)	14	56	91.8	70.3
(0.9, 0.3)	8	75	92.8	71.1
(0.59, 0.8)	21	35	92.3	57.4
(0.78, 0.8)	14	56	94.7	69.8
(0.59, 2)	21	35	75.1	54.1
(0.21, 2.5)	14	54	77.5	70.6
(0.24, 6.4)	22	68	89.1	51.1

Cross-linked precursors were prepared by heating the polymerization mixtures to 70 °C (Series 1 and 2) or 120 °C (Series 3) for 24 h in the presence of AIBN as a thermal radical initiator. In all cases the polymerization resulted in solid monoliths, that varied in appearance from transparent to opaque. This suggests a range of length scale from nanometer to micrometer exists in the cross-linked precursors. The PLA was then selectively etched via basic hydrolysis. The complete removal of PLA was confirmed by gravimetric analysis and the disappearance of a vibrational frequency corresponding to the carbonyl stretching in FTIR spectra. The resulting porous polymers were analyzed by means of SEM, nitrogen sorption experiments, and mercury intrusion porosimetry to

quantitatively characterize the meso- and macropore structure. SAXS was used to investigate the microphase-separated morphology of the precursors and the corresponding porous polymers.

4.3 Results

4.3.1 Variation in PLA-OH Concentration at Fixed (PLA-OH+PLA-CTA)

The first series was designed to investigate the ability to control the domain size of the bicontinuous structure from nanometers to micrometers through the addition of PLA-OH to the polymerization mixture, where $r_H = w_{PLA\text{-}OH}/(w_{PLA\text{-}OH} + w_{PLA\text{-}CTA})$ was varied from 0 to 1. In all cases, w_{PLA} was fixed at 0.3 in order to maintain an approximately constant void fraction in the porous polymer. PLA-CTA-1 with M_w = 17 kg mol^{-1} and PLA-OH with M_w = 18 kg mol^{-1} were used for the preparation of 15 polymerization mixtures. We note that increase in the fraction of PLA-OH not only increases r_H, but also [M (S + DVB)]:[PLA-CTA]. In most cases, the polymerization mainly proceeds via RAFT mechanism. However, when r_H = 1, the polymerization proceeds via normal free radical polymerization initiated by AIBN as no RAFT CTA is present in the polymerization mixture.

The mass yield was over 90 wt% when $r_H < 0.9$. The yields decreased to ca. 60 wt% for samples with $r_H \geq 0.92$ presumably due to incomplete conversion of the monomers within the given polymerization time. While the precursors with $r_H \leq 0.6$ were transparent, the

precursors with $r_H \geq 0.6$ were opaque which suggests the presence of larger length scale features (Figure 4.1).

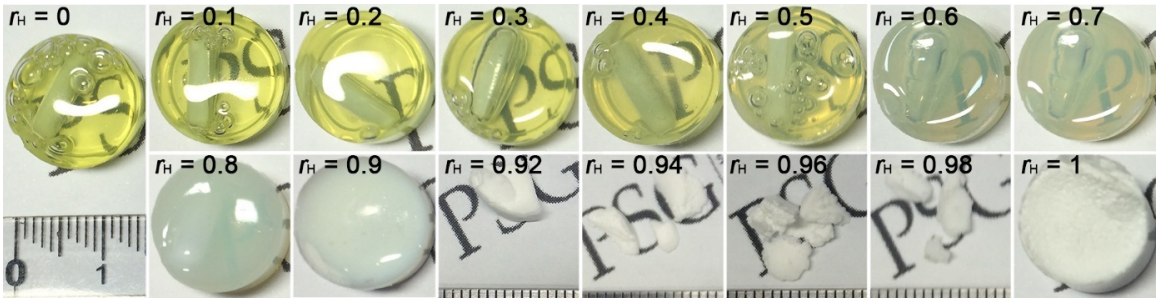

Figure 4.1. Images of the Series 1 precursors with $w_{PLA} = 0.3$ and various r_H, as indicated in each image.

Representative SAXS data of select Series 1 precursors is shown in Figure 4.2a as dotted lines. For $r_H \leq 0.6$, a broad principal scattering peak (at q^*) was accompanied by a broad shoulder at $2q^*$ consistent with a disordered bicontinuous morphology; this scattering feature is also observed in topologically similar morphologies formed by spinodal decomposition.[35] This characteristic feature is consistent with the PIMS mechanism, as previously reported.[2] As r_H increased, q^* gradually shifted to smaller q or larger domain spacing. It was not possible to identify q^* from samples with $r_H > 0.6$ as the characteristic structural length scale present in the precursor was greater than the instrument limit (up to 114 nm, 0.055 nm^{-1} in q, with the settings employed in this study). However, the appearance of the broad shoulder suggests that the bicontinuous morphology persists in the $r_H \leq 0.9$ regime.

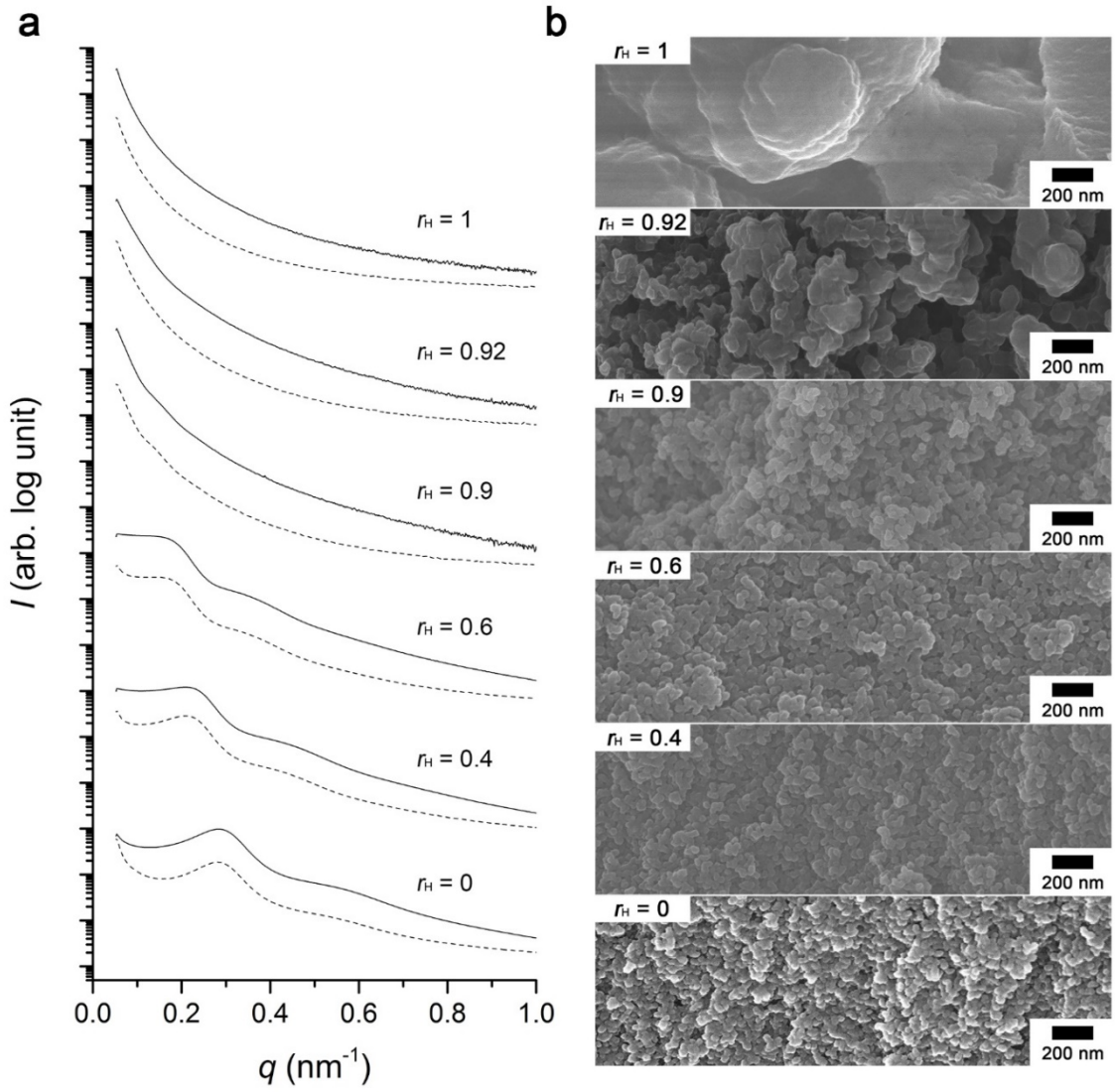

Figure 4.2. (a) Representative SAXS data of Series 1 precursors (dotted lines) and the corresponding porous polymers (solid lines). For clarity, the traces are arbitrarily shifted between samples, but the relative intensity before and after etching is maintained. (b) SEM images of the porous polymers after coating with Os.

Removal of PLA from the precursors resulted in a large increase in scattering intensity from all samples due to the large electron density contrast of the pores with the polymer matrix (solid lines in Figure 4.2a). The shape of the SAXS patterns was retained after PLA etching indicating that the bicontinuous structures were successfully converted into

3D continuous porous structures. Scanning electron microscopy (SEM) images of the porous polymers after coating with OsO_4 corroborated formation of the reticulated pores (Figure 4.2b). When r_H reached 0.92, the pore size drastically increased and macroporous materials were produced. SAXS profiles and SEM images for all compositions are shown in Figure 4.3 and 4.4, and the characteristics are summarized in Table 4.5.

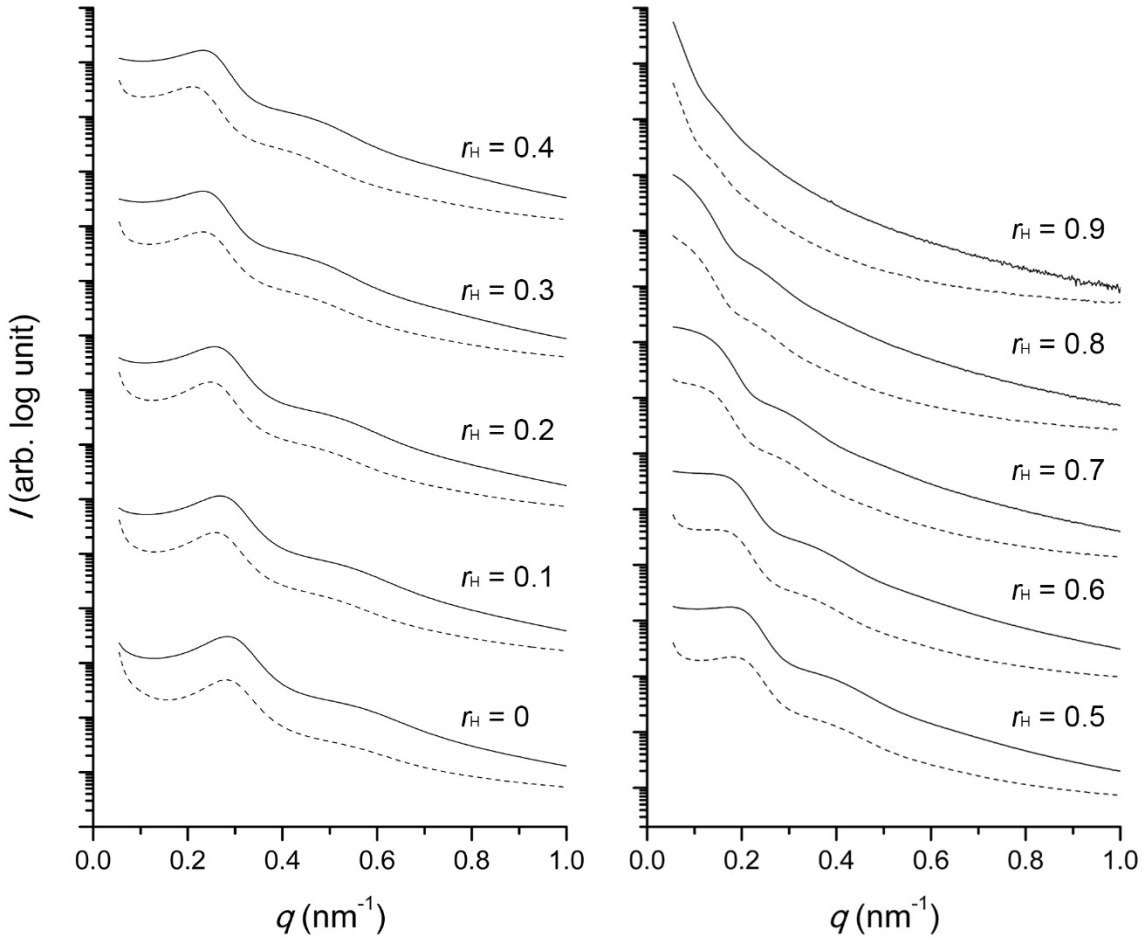

Figure 4.3. SAXS data of Series 1 precursors (dotted lines) and the corresponding porous polymers (solid lines). For clarity, the traces are arbitrarily shifted between samples, but the relative intensity before and after etching is maintained.

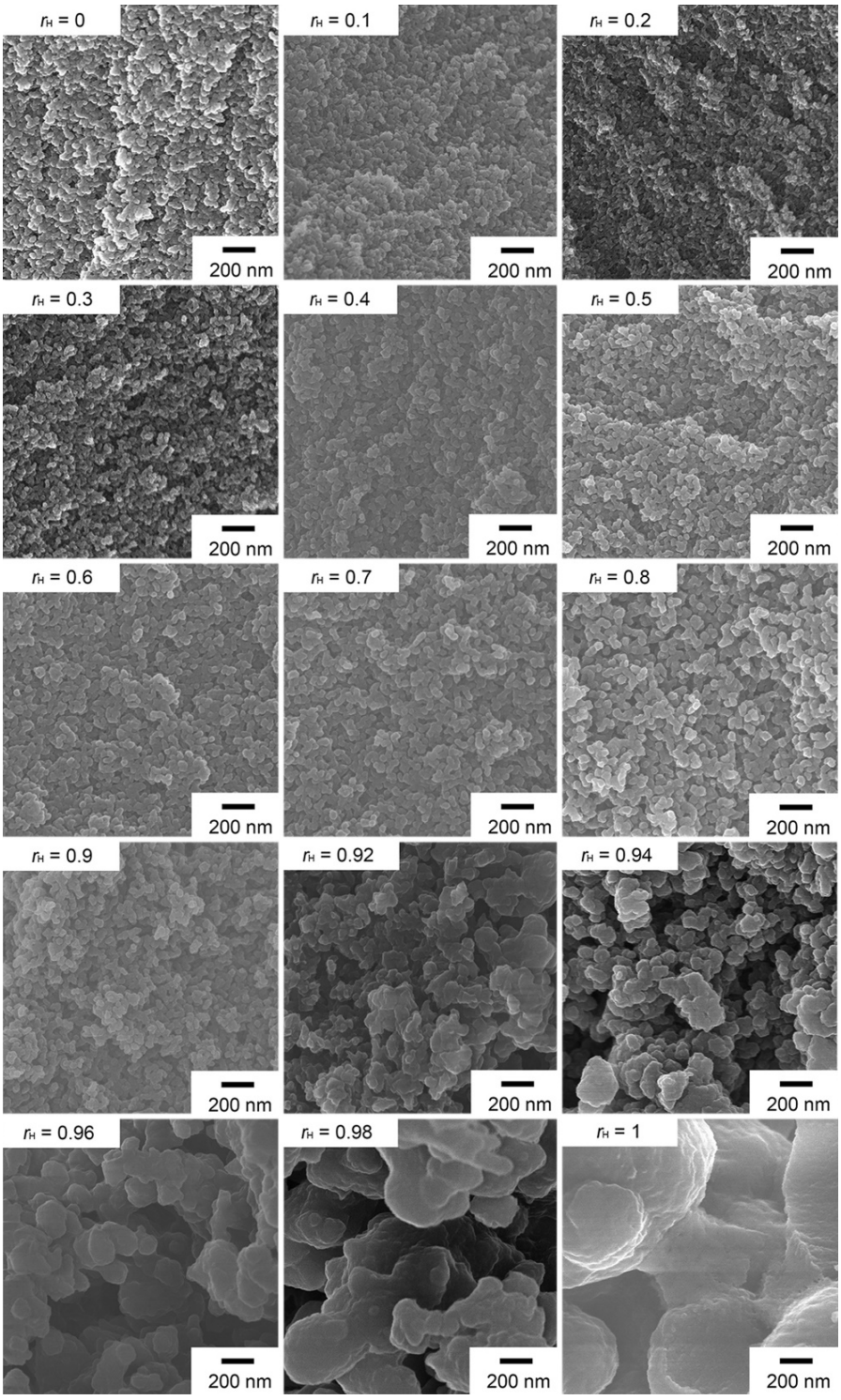

Figure 4.4. SEM image of porous polymers derived from Series 1 precursors. Samples were coated with Os prior to imaging.

Table 4.5. Pore characteristics of the Series 1 porous polymers

r_H	d (nm)	D_{N2} (nm)	S_{N2} (m^2 g^{-1})	V_{N2} (mL g^{-1})[a]	D_{Hg} (nm)	S_{Hg} (m^2 g^{-1})	V_{Hg} (mL g^{-1})[b]
0	22	6.0	198	0.33	13.7	109	0.29
0.1	24	6.3	162	0.30	15.6	101	0.28
0.2	25	6.8	174	0.34	15.6	117	0.31
0.3	27	7.7	139	0.29	15.7	111	0.29
0.4	30	8.2	138	0.30	16.2	122	0.33
0.5	34	9.3	120	0.30	16.7	123	0.33
0.6	42	10.7	118	0.34	18.9	132	0.41
0.7	-	13.6	86	0.29	13.2	130	0.31
0.8	-	19.1	74	0.29	-	-	-
0.9	-	39.0	48	0.14	24.1	144	0.46
0.92	-	-	-	-	1814	86	1.13
0.94	-	-	-	-	2704	49	1.69
0.96	-	-	-	-	2689	27	2.10
0.98	-	-	-	-	1961	12	2.42
1	-	-	-	-	585	20	0.77

[a]Pore volume calculated from the point P/P_0 = 0.95 in the nitrogen sorption isotherm. [b]Pore volume calculated by mercury intrusion porosimetry.

The porous monoliths were further characterized by nitrogen sorption measurements conducted at 77 K (Figure 4.5). For $r_H \leq 0.9$ Type IV isotherms with H2 hysteresis were obtained, consistent with the presence of a 3D connected mesoporous network (Figure 4.5a). The pore volume was 0.35 cm^3 g^{-1} for these samples, which is comparable to the volume fraction of PLA in the cross-linked precursor. Importantly, capillary condensation shifted to higher relative pressures as r_H increased, consistent with the relationship between the pore size and r_H observed in SAXS. Pore size distributions, estimated with BJH analysis applied the desorption branch of the isotherms (Figure 4.5b) indicated a gradual increase in the pore diameter (D) from 6 nm (r_H = 0) to 39 nm (r_H = 0.9). We note that the distributions broadened as r_H increased and that the step-like increase at relative pressures close to 1 is likely an instrumental artifact. Porous polymers obtained

with $r_H > 0.9$ could not be evaluated by the nitrogen sorption isotherm analysis due to the relatively large pore sizes in those samples.

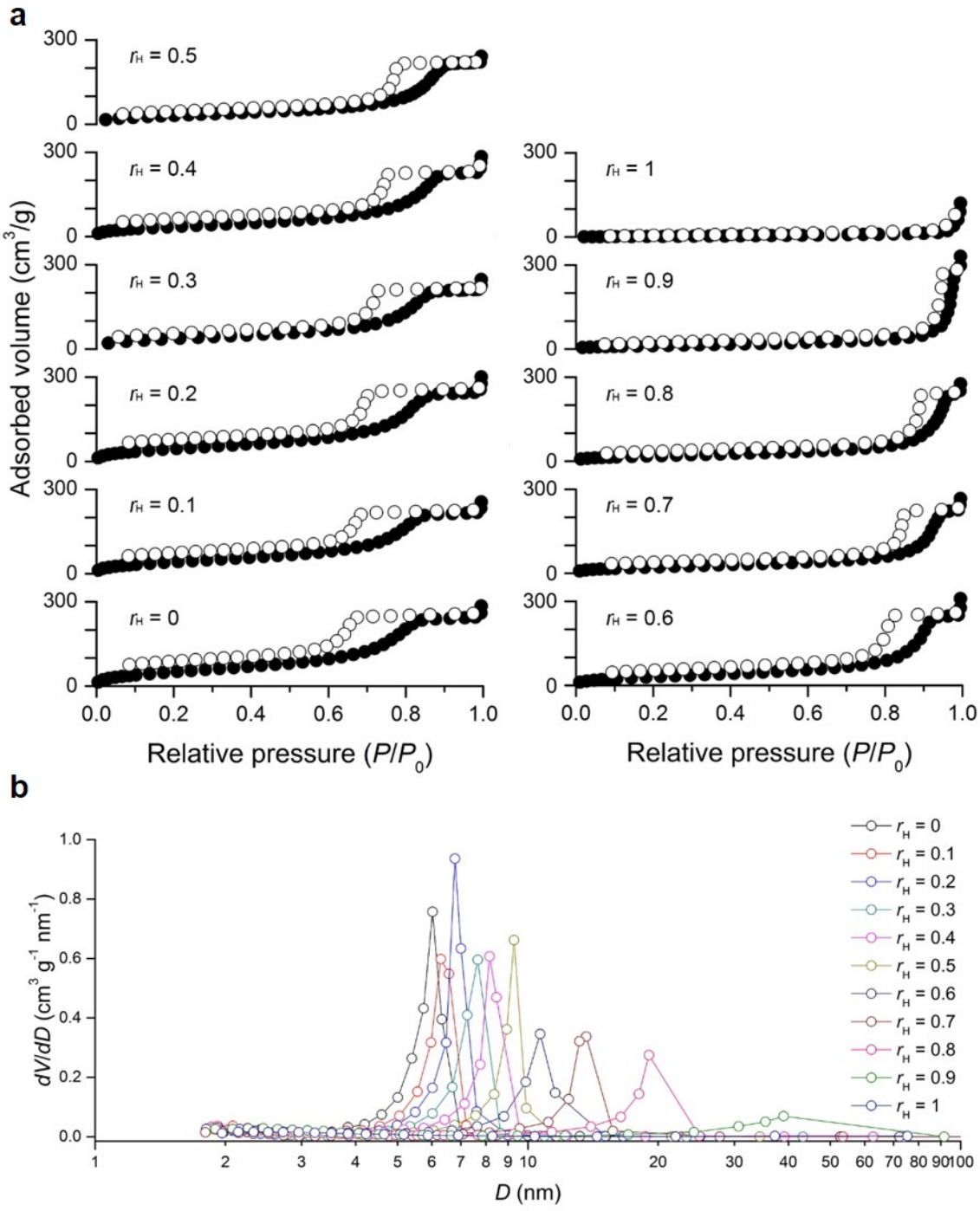

Figure 4.5. (a) Nitrogen sorption isotherms of the Series 1 porous polymers obtained at 77 K. Filled circles: adsorption branch; Open circles: desorption branch. (b) Pore size distribution as a function of pore diameter (*D*) based on BJH analysis of the desorption branch in (a).

A complementary technique, mercury intrusion porosimetry, was used to further probe the porous structure of the monoliths.[36] Representative mercury intrusion porosimetry data is shown in Figure 4.6a. Intrusion data was obtained over a range of pressures from 30 to 3.1 × 10^6 Torr (3.2 nm – 310 μm range in pore size) covering both the meso- and macroporous regimes. For monoliths with $r_H \leq 0.9$, a negligible amount of mercury was intruded into the samples in the pressure range corresponding to the macroporous regime indicating that only mesopores are present in these samples. When $r_H > 0.9$ the presence of macropores was evident by an increase in the cumulative pore volume in the range of D = 10 – 0.1 μm. Figure 4.6b shows pore size distributions derived from the intrusion data, which clearly depicts the development of macropores. However, the distributions are often not unimodal suggesting heterogeneity in the pore structure. We note that a similarly broad pore size distribution has been obtained from macroporous polymers produced via PIPS process.[37] We also observed a significant increase in the total pore volumes when $r_H > 0.9$. Figure 4.7 shows data for all r_H.

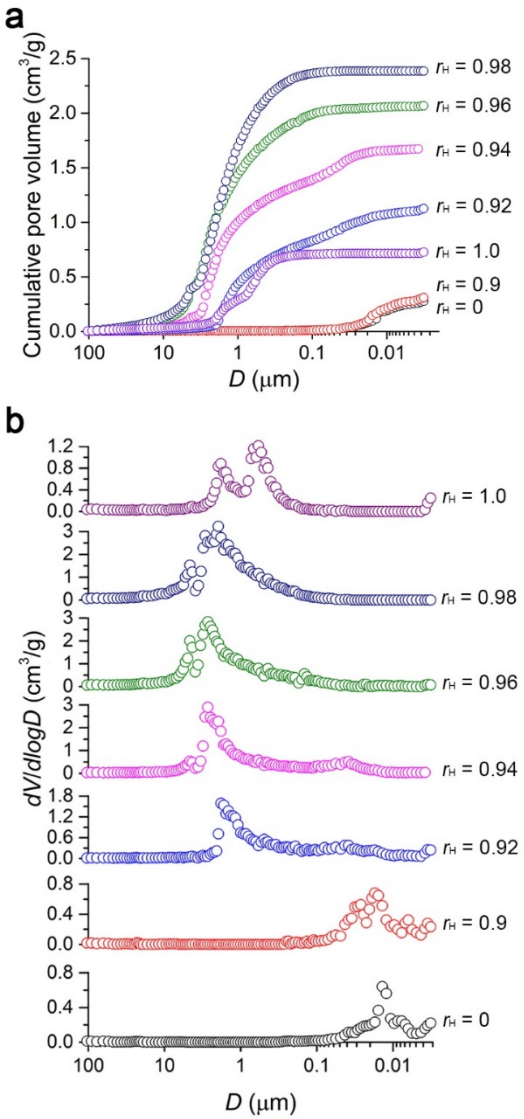

Figure 4.6. Representative mercury intrusion porosimetry data of Series 1. (a) Cumulative pore volume as a function of pore diameter (D). (b) Corresponding pore size distribution as a function of D derived from the cumulative volume (V) data.

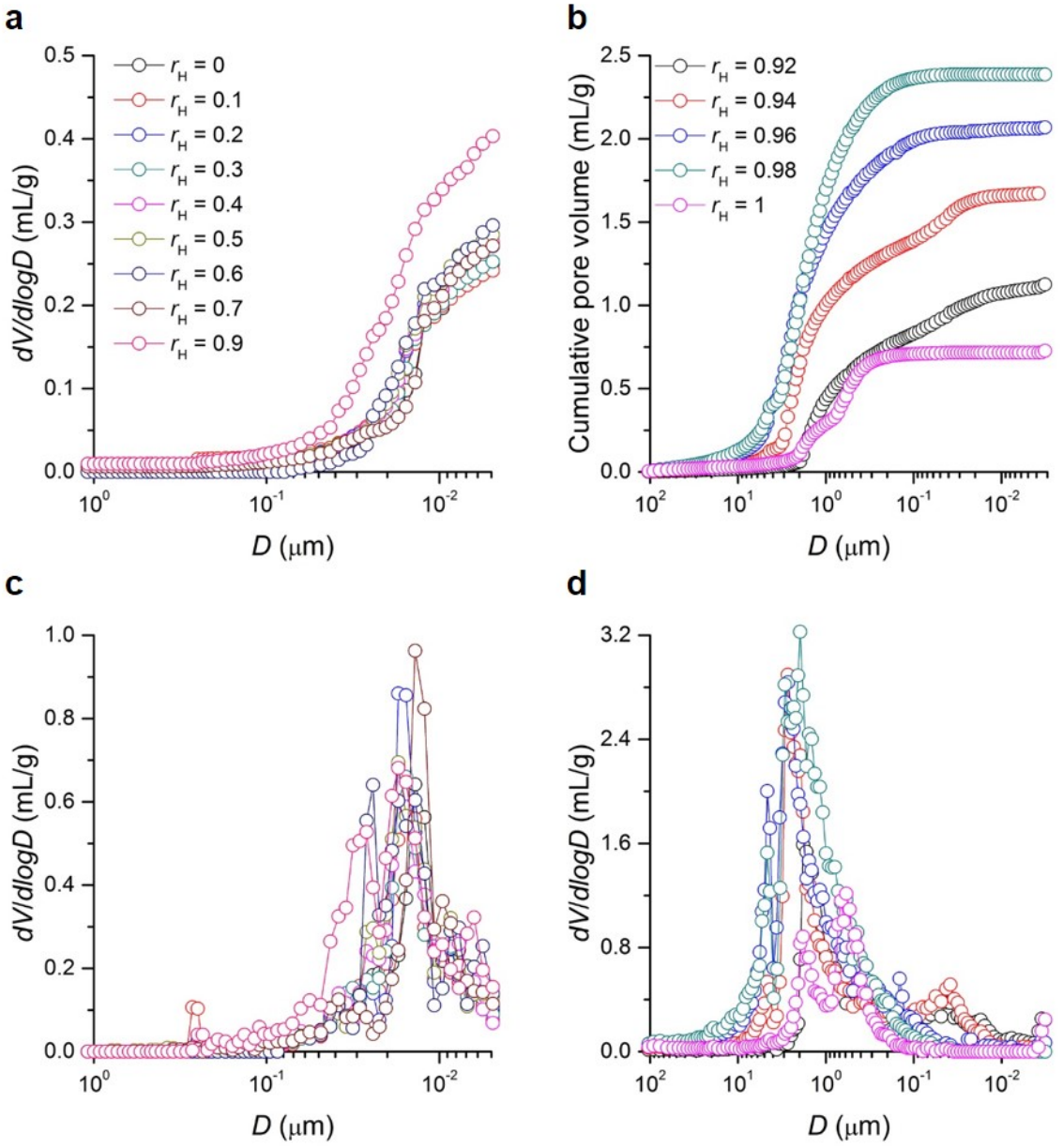

Figure 4.7. Mercury intrusion porosimetry data of the Series 1 porous polymers. Data of samples containing only mesopores are presented on left (a and c), and those containing both meso- and macropores were shown on right (b and d). (a, b) Cumulative pore volume as a function of pore diameter (*D*). (c, d) Pore size distribution as a function of *D* derived from the cumulative pore volume (*V*) data.

4.3.2 Variation in PLA-OH Concentration at Fixed M:CTA

The second series was designed to elucidate the effects of varying r_H while maintaining a constant [M]:[CTA] molar ratio by adding a molecular CTA (CTA-1) to the polymerization mixture. Specifically, the amount of CTA-1 was adjusted to have an equivalent molar concentration of trithiocarbonate groups in the polymerization mixture to the case of $r_H = 0$ in Series 1 (i.e. a mixture of PLA-CTA, S, and DVB with w_{PLA} fixed at 0.3). We expected that maintaining the concentration of the CTA would facilitate RAFT polymerization throughout Series 2, even at high r_H, and impart reliable control over pore structure of the resulting porous polymers.

11 polymerization mixtures containing PLA-CTA-1, PLA-OH, S, DVB, AIBN and CTA-1 with different r_H were prepared and polymerized following identical reaction conditions to Series 1. In contrast to Series 1 where low yields (ca. 60%) were observed at high r_H (> 0.9), all of the Series 2 precursors had yields > 90%. While the yellow color of the Series 2 precursors was more intense due to presence of more trithiocarbonate groups originating from CTA-1, their transparency decreased more rapidly as r_H increased indicating that the addition of CTA-1 led to an increase in the length scale of the nanostructures (Figure 4.8). Again, PLA etching produced the corresponding porous polymers.

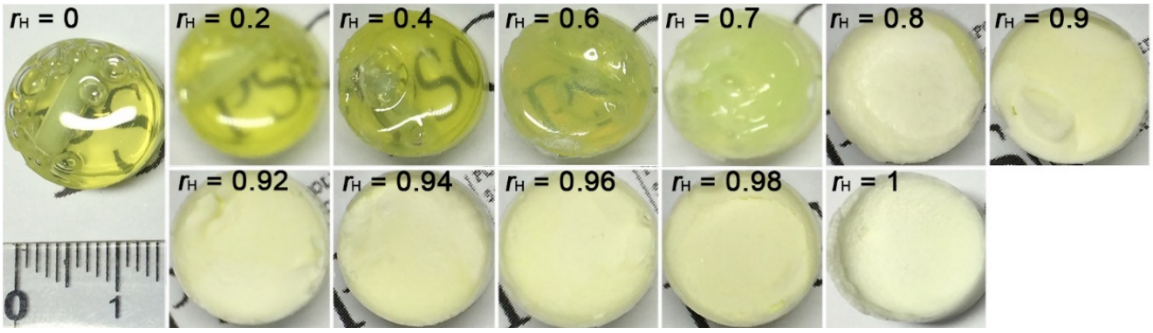

Figure 4.8. Images of the Series 2 precursors obtained from constant w_{PLA} (0.3) and [M]:[CTA] ratio with varied r_H as indicated in each image.

SAXS (Figure 4.9a, 4.10), SEM (Figure 4.9b, 4.11), and nitrogen sorption measurements (Figures 4.12) of the Series 2 precursors and the corresponding porous polymers are all consistent with a rapid increase in the length scale of the bicontinuous structure as r_H increases, and are summarized in Table 4.6. For example, domain spacing (d) of the Series 2 precursors estimated from SAXS data was 28 and 62 nm when r_H = 0.2 and 0.6, while the Series 1 precursors gave d = 25 and 42 nm at the same r_H. Due to the large domain spacing, it was not possible to determine q^* for $r_H > 0.6$. In the nitrogen sorption isotherms (Figure 4.12a), capillary condensation was not observed for $r_H > 0.7$, which suggests that the pore size falls in the macroporous regime. This meso- to macroporous transition was observed at r_H = 0.9 in the Series 1 porous polymers.

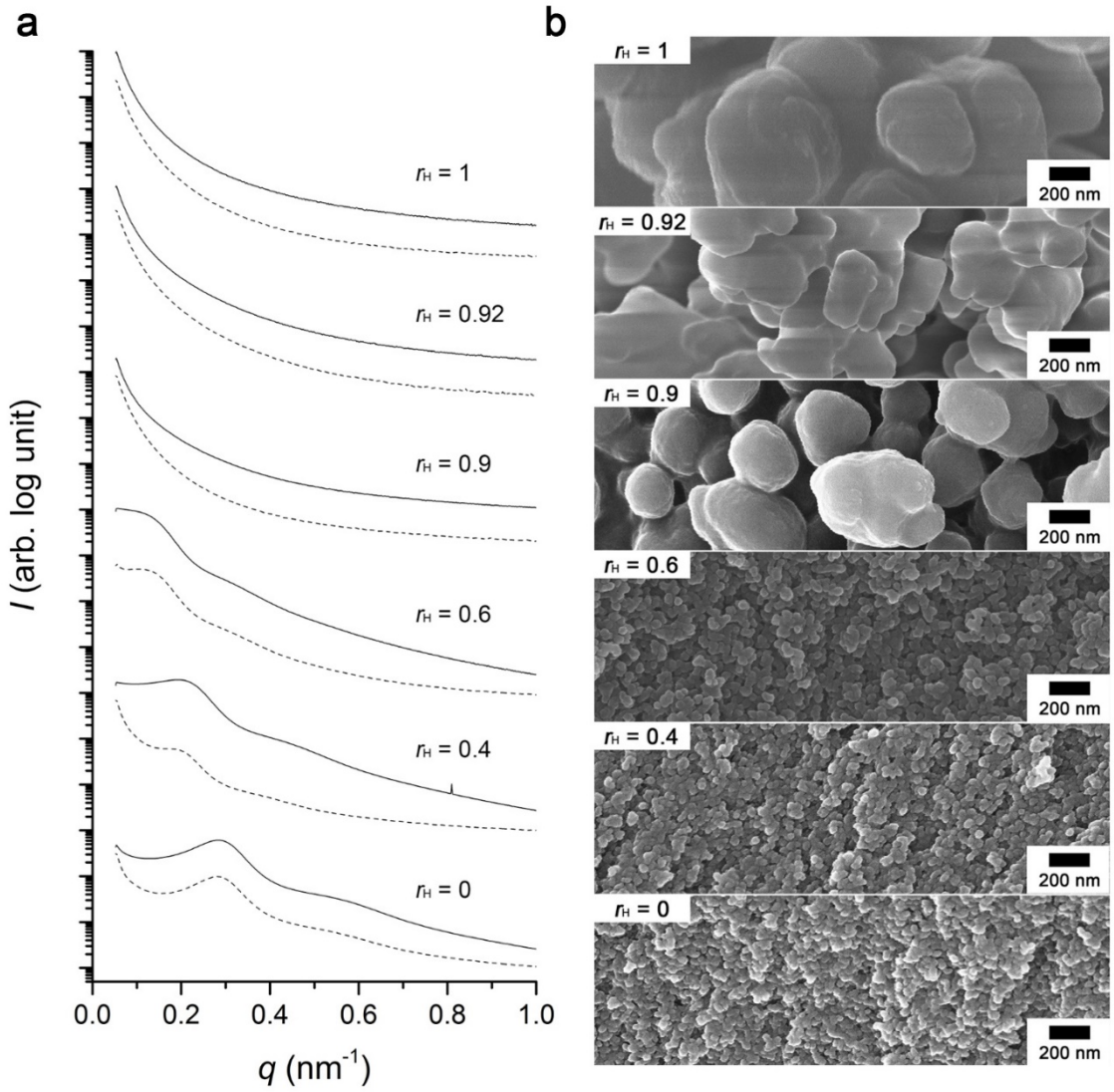

Figure 4.9. (a) Representative SAXS data of Series 2 precursors (dotted lines) and the corresponding porous polymers (solid line). The scattering profiles were arbitrarily shifted between samples, but the relative intensities before and after etching are maintained. (b) SEM images of the porous polymers.

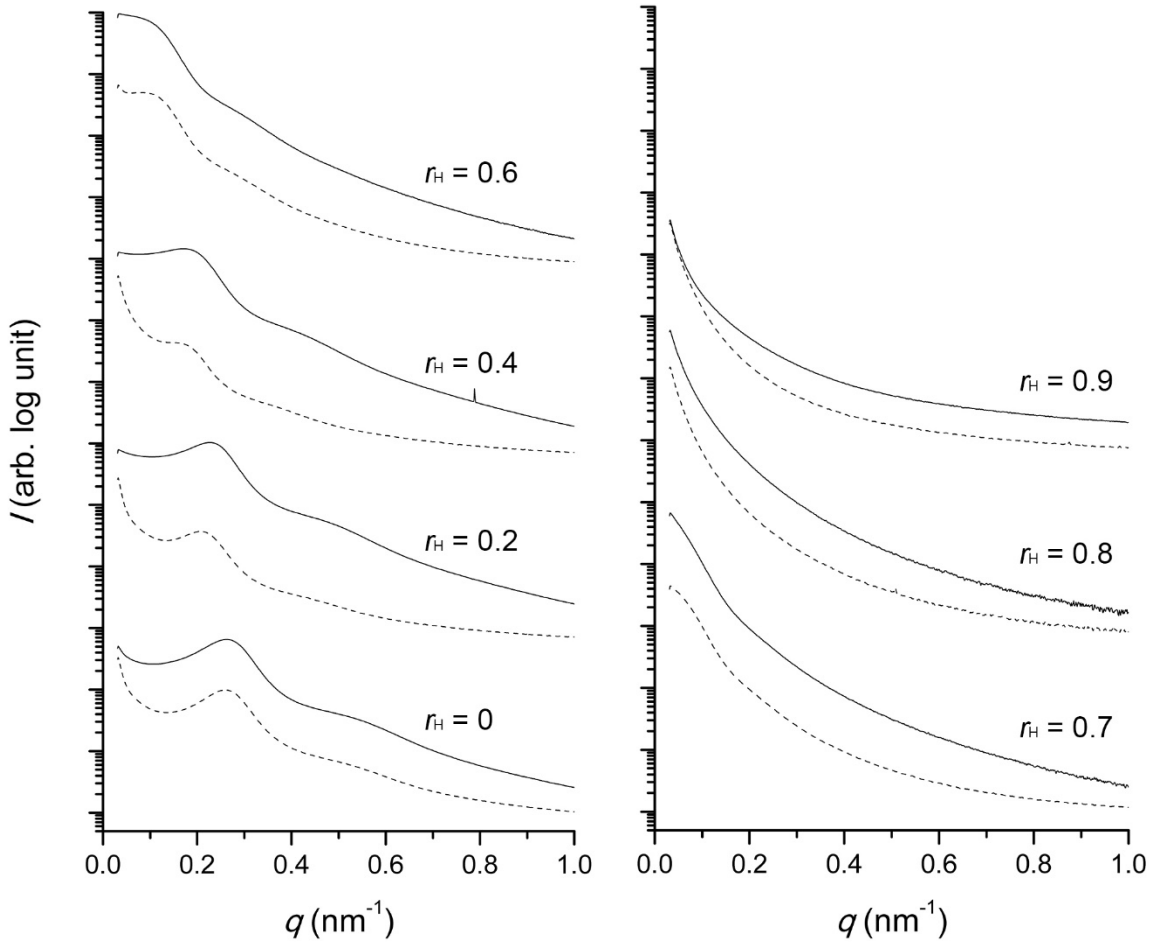

Figure 4.10. SAXS data of Series 2 precursors (dotted line) and the corresponding porous polymers (solid line). The data was arbitrarily shifted vertically for clarity.

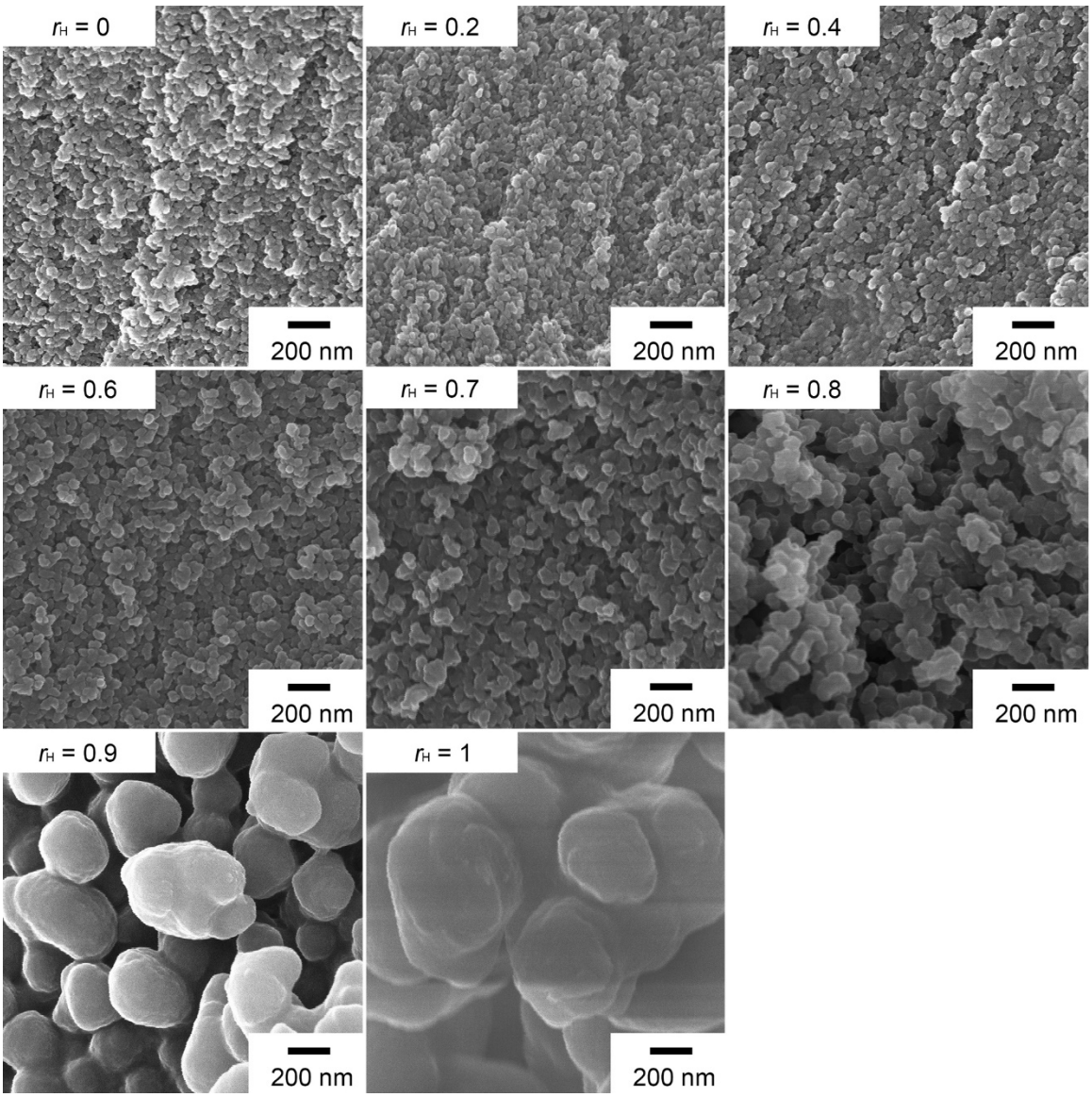

Figure 4.11. SEM image of porous polymers derived from Series 2 precursors as indicated within each image. Sample were coated with Os prior to imaging.

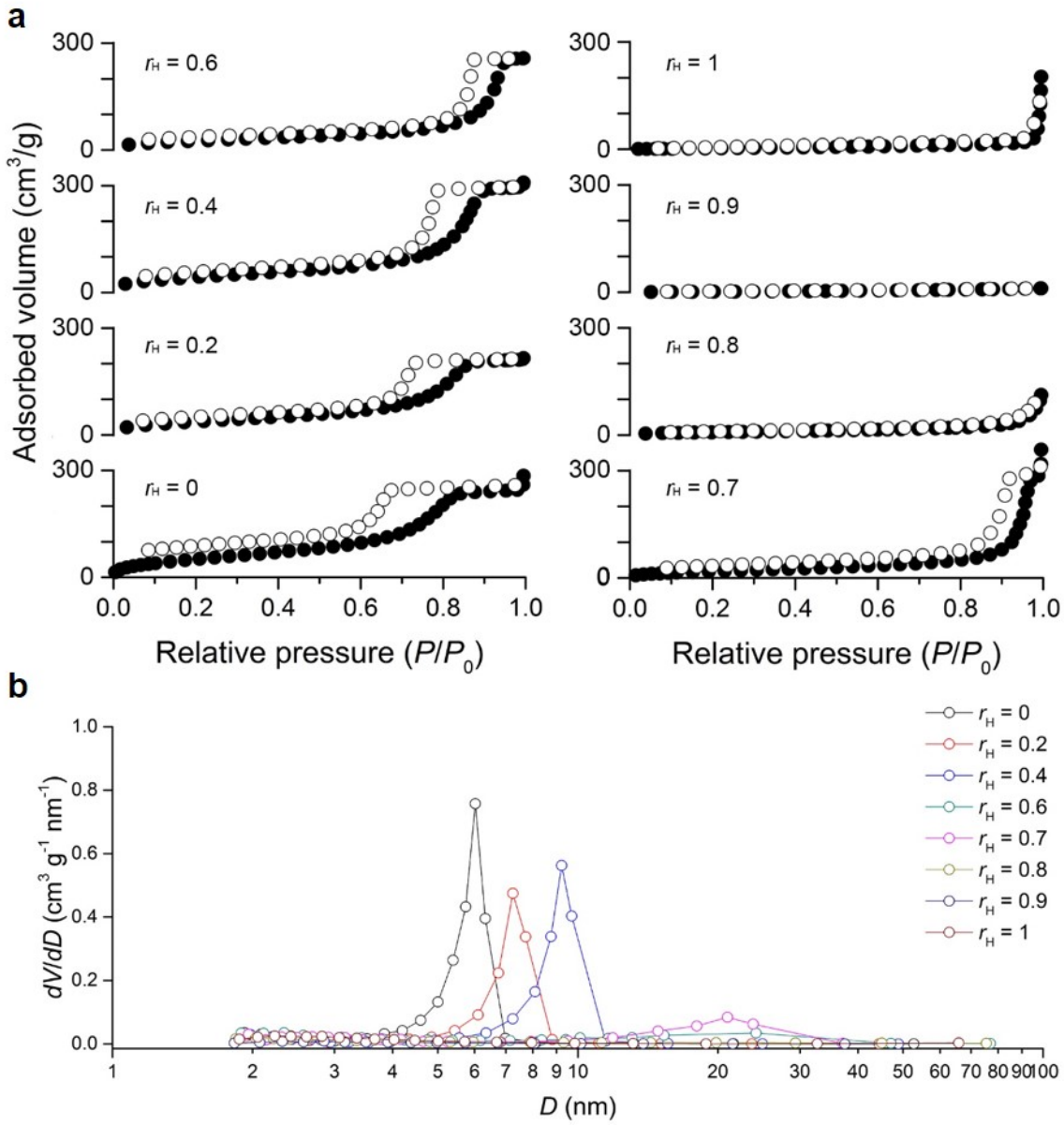

Figure 4.12. (a) Nitrogen sorption isotherms of the Series 2 porous polymers obtained at 77.3 K. Filled circles: adsorption branch; open circles: desorption branch. (b) Pore size distribution as a function of pore diameter (*D*) based on BJH analysis of the desorption branch in (a).

Table 4.6. Pore characteristics of the Series 2 porous polymers

r_H	d (nm)	D_{N2} (nm)	S_{N2} (m^2 g^{-1})	V_{N2} (mL g^{-1})[a]	D_{Hg} (nm)	S_{Hg} (m^2 g^{-1})	V_{Hg} (mL g^{-1})[b]
0.2	22	6.0	198	0.33	13.7	109	0.29
0.4	28	7.2	142	0.29	-	-	-
0.6	37	9.2	162	0.41	-	-	-
0.7	62	24.1	99	0.33	-	-	-
0.8	-	21.0	72	0.24	25	114	0.41
0.9	-	-	-	-	71	41	0.47
1	-	-	-	-	1000	3.4	0.7

[a]Pore volume calculated from the point $P/P_0 = 0.95$ in the nitrogen sorption isotherm.
[b]Pore volume calculated by mercury intrusion porosimetry.

We analyzed several porous polymers with $r_H \geq 0.7$ using mercury intrusion porosimetry (Figure 4.13). The intruded volume of mercury when $D > 1.3$ μm is attributed to the interstitial voids between polymer globules. While only mesopores were observed when $r_H = 0.7$, consistent with nitrogen sorption measurements, the porous polymer with $r_H = 0.8$ mostly contained macropores as indicated in the pore size distribution shown in Figure 4.13b. Importantly, a macroporous polymer with average $D = 1.0$ μm and unimodal pore size distribution was successfully obtained at $r_H = 0.9$. Compared with the mercury intrusion porosimetry data of the Series 1 porous polymers, these data suggest that macroporous polymers with relatively more uniform pore size distributions are produced in Series 2 by adjusting the [M]:[CTA] ratio.

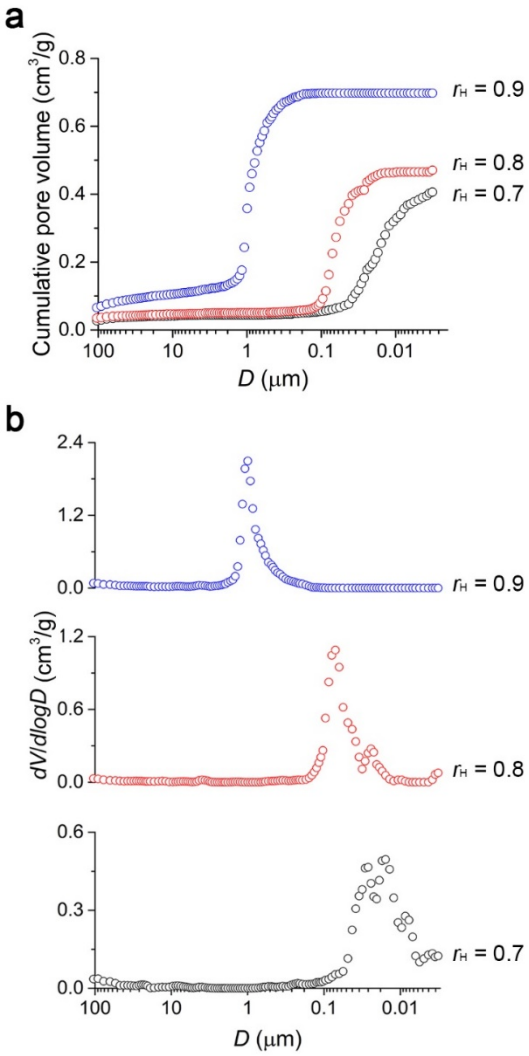

Figure 4.13. Representative mercury intrusion porosimetry data of Series 2. (a) Cumulative pore volume as a function of pore diameter (*D*). (b) Corresponding pore size distribution as a function of *D* derived from the cumulative volume (*V*) data.

4.3.3 Addition of PLA-OH at Fixed M:PLA-CTA

We also investigated changes in the morphology of the cross-linked precursor and the corresponding porous polymer through the addition of PLA-OH to the polymerization mixture while [S + DVB]:[PLA-CTA] was constant. Based on previous results, we expected that below the solubility limit of PLA-OH in the PLA domains the size of the

PLA domains would increase with the addition of PLA-OH, but macrophase separation would occur when the solubility limit was exceeded resulting in simultaneous macro- and microphase separation.[18] Consequently, porous polymers with greater void fractions or hierarchically porous polymers containing macro- and mesopores would be produced by the removal of PLA. To this end, we varied the molar mass of PLA-CTA-2 (11 and 35 kg mol^{-1}) and PLA-OH (11, 28, and 70 kg mol^{-1}) to elucidate the effect of PLA-OH composition on morphology of the porous polymer. The polymerization mixtures were prepared by adding PLA-OH to a solution of PLA-CTA, S, and DVB where [S]:[DVB] = 4:1 and $w_{PLA\text{-}CTA}$:w_{S+DVB} = 3:7 (the solution corresponds to r_H = 0 sample in Series 1). The sample composition is described by two parameters: (r_H, α) where $r_H = w_{PLA\text{-}OH}/w_{PLA}$ and $\alpha = M_{w,PLA\text{-}OH}/M_{w,PLA\text{-}CTA}$.

When 11 kg mol^{-1} PLA-OH was added to a solution of S, DVB, and PLA-CTA ($M_{w,PLA\text{-}CTA}$ = 35 kg mol^{-1}), a homogeneous polymerization mixture formed at all investigated compositions ($w_{PLA\text{-}OH}$ = 0.35, 0.56, 0.75). As $w_{PLA\text{-}OH}$ increased, an increase in d in the resulting cross-linked precursors and the corresponding porous polymers was observed by SAXS and SEM as shown in Figure 4.14 and summarized in Table 4.7, indicating swelling of the PLA microdomain by PLA-OH, while retaining the bicontinuous structure.

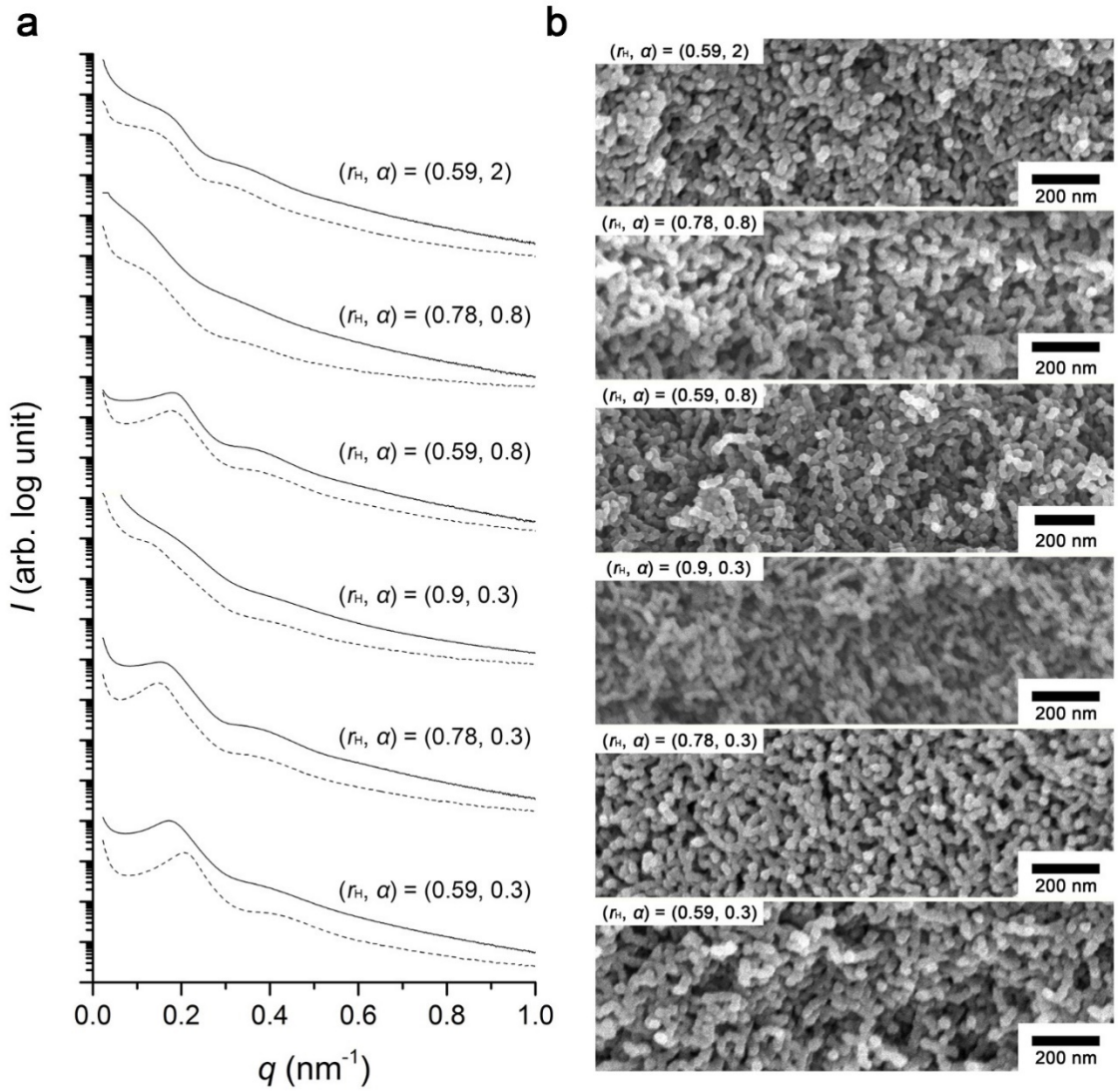

Figure 4.14. SAXS data of Series 3 precursors (dotted line) and the corresponding porous polymers (solid line) with PLA-CTA-2 of 35 kg mol^{-1}. (b) SEM images of corresponding porous polymers.

Table 4.7. Pore characteristics of the Series 3 porous polymers

(r_H, α)	d (nm)	D_{N2} (nm)	S_{N2} (m^2 g^{-1})	V_{N2} (mL g^{-1})[a]	D_{Hg} (nm)	S_{Hg} (m^2 g^{-1})	V_{Hg} (mL g^{-1})[b]
(0.59, 0.3)	31	15.6	208	0.85	144	62	0.74
(0.78, 0.3)	42	24.4	183	1.1	-	-	-
(0.9, 0.3)	48	34.6	80	0.21	63.2	146	0.83
(0.59, 0.8)	35	15.6	201	0.88	-	-	-
(0.78, 0.8)	63	34.2	163	0.46	-	-	-
(0.59, 2)	52	19.0	153	0.65	-	-	-
(0.58, 2.5)	-	3.7	267	0.28	404	96	0.77
(0.79, 6.4)	-	13.1	206	0.79	-	-	-

[a]Pore volume calculated from the point P/P_0 = 0.95 in the nitrogen sorption isotherm. [b]Pore volume calculated by mercury intrusion porosimetry.

The use of PLA-OH with larger M_w (28 and 70 kg mol^{-1}) decreased the solubility limit thus restricting the compositional ranges attainable. Within the solubility limit, a similar morphological effect was observed as a function of $w_{PLA\text{-}OH}$, although the extent of swelling increased slightly with the increase in the molar mass of PLA-OH resulting in smaller q^* in the SAXS data. Nitrogen sorption measurements of the porous polymers corroborated increased pore volume and pore size due to swelling of the PLA microdomain by PLA-OH (Figure 4.15). The increase in pore size with increasing r_H is comparable to Series 1, which is attributed to the concurrent decrease in [CTA] in the reaction mixture.

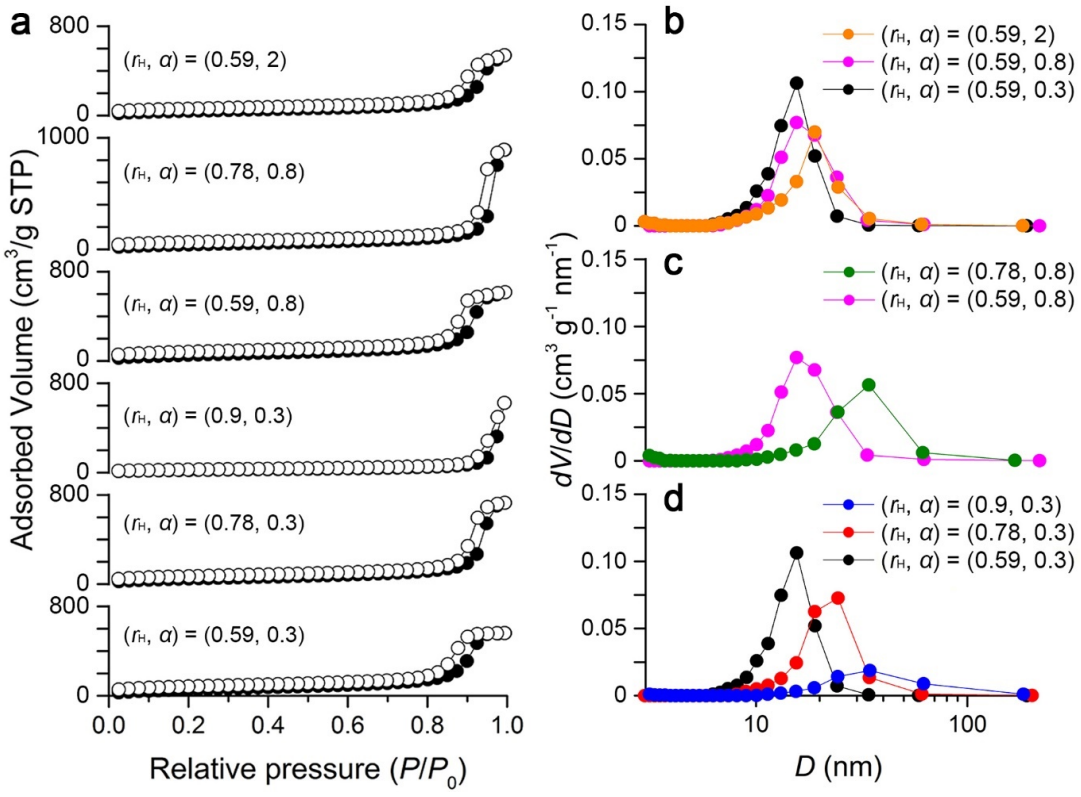

Figure 4.15. (a) Nitrogen sorption isotherms of the Series 3 with PLA-CTA-2 of 35 kg mol^{-1} obtained at 77 K (filled circles: adsorption branch; open circles: desorption branch). (b-d) Pore size distributions based on BJH analysis of the desorption branch of the isotherms in (a). (b) Porous polymers synthesized from PLA-OH of 11 kg mol^{-1}. (c) Porous polymers synthesized from PLA-OH of 28 kg mol^{-1}. (d) Porous polymers synthesized with $w_{\text{PLA-OH}} = 0.35$.

When PLA-CTA with a lower M_w (11 kg mol^{-1}) was combined with higher $M_{w,\text{PLA-OH}}$ (28 and 70 kg mol^{-1}), the system reached solubility limit of PLA-OH in the PLA microdomain during polymerization and resulted in macrophase separation between a fraction of PLA-OH and the rest of the polymerization mixture (Figure 4.16). For example, a cross-linked precursor synthesized from PLA-OH with molar mass of 28 kg mol^{-1}, (r_H, α) = (0.58, 2.5), produced a SAXS pattern where a broad and weak scattering peak appeared at q^* = 0.25 nm^{-1} (d = 25 nm) but strong scattering intensity from larger

length scale features was dominant (Figure 4.16c). SEM imaging of the corresponding porous polymer revealed macroporosity, further evidence that some portion of PLA-OH was excluded from the forming block polymer during polymerization (Figure 4.16d). This is consistent with the previous finding reported for the mixture of PEO, PLA-CTA, S, and DVB where PEO was used as a PLA-miscible and nonreactive porosity-inducing agent.[18] Further increasing the molar mass of PLA-OH to 70 kg mol^{-1} resulted in the shift of q^* to larger q in the SAXS data of the cross-linked precursor (q^* = 0.34 nm^{-1}, d = 18 nm) indicating that PLA-OH was excluded from the growing PLA-*b*-P(S-*co*-DVB) even more rapidly and thereby decreased the swelling of the PLA microdomain (Figure 4.16a), leading to both macrophase and microphase separation induced by polymerization. PLA etching of the precursor produced hierarchically porous polymer spheres as observed by SEM, where the voids between the spheres correspond to macropores and the mesopores are located within the spheres (Figure 4.16b).

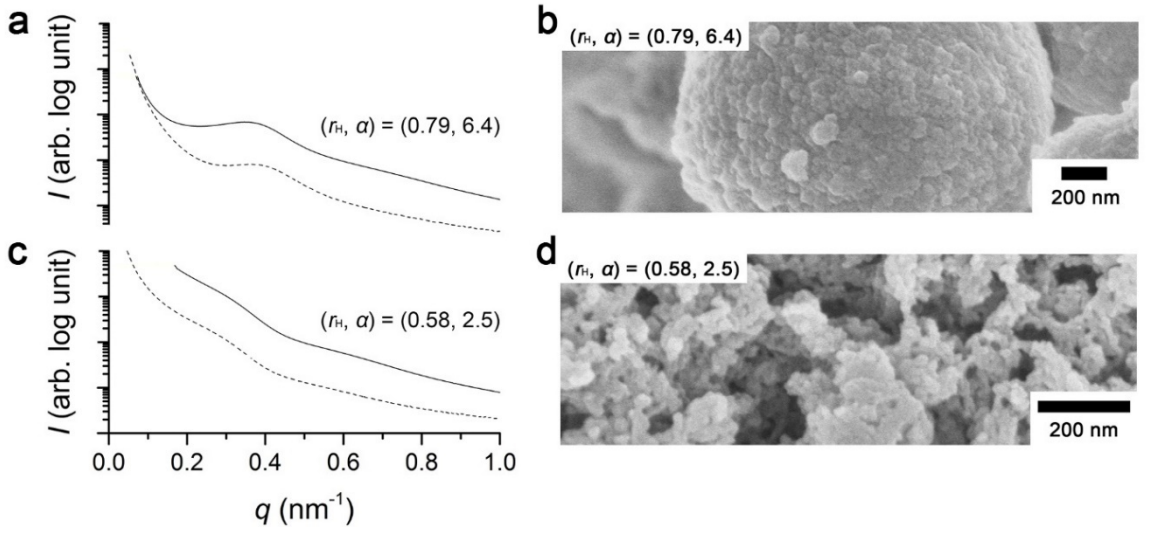

Figure 4.16. (a, c) SAXS data of Series 3 precursors (dotted lines) and the corresponding porous polymers (solid lines) with PLA-CTA-2 of 11 kg mol^{-1}. (b, d) SEM images of corresponding porous polymers.

Nitrogen sorption isotherm analysis data of the hierarchically porous polymers is shown in Figure 4.17. While the sample (r_H, α) = (0.79, 6.4) showed comparable D and pore volume to the mesoporous polymer produced without PLA-OH, the sample (r_H, α) = (0.58, 2.5) showed higher D (13 nm) and larger porosity. This is further evidence that some fraction of the PLA-OH contributed to swelling of PLA microdomain while the rest of PLA-OH was segregated from the polymerization mixture in case of (r_H, α) = (0.58, 2.5), but PLA-OH was almost completely excluded in the very early stage of polymerization in the mixture of (r_H, α) = (0.79, 6.4). For both cases, hierarchically structured precursors were produced as a result of the combined PIMS and PIPS processes, and were converted into the hierarchically porous polymers containing mesopores and macropores.

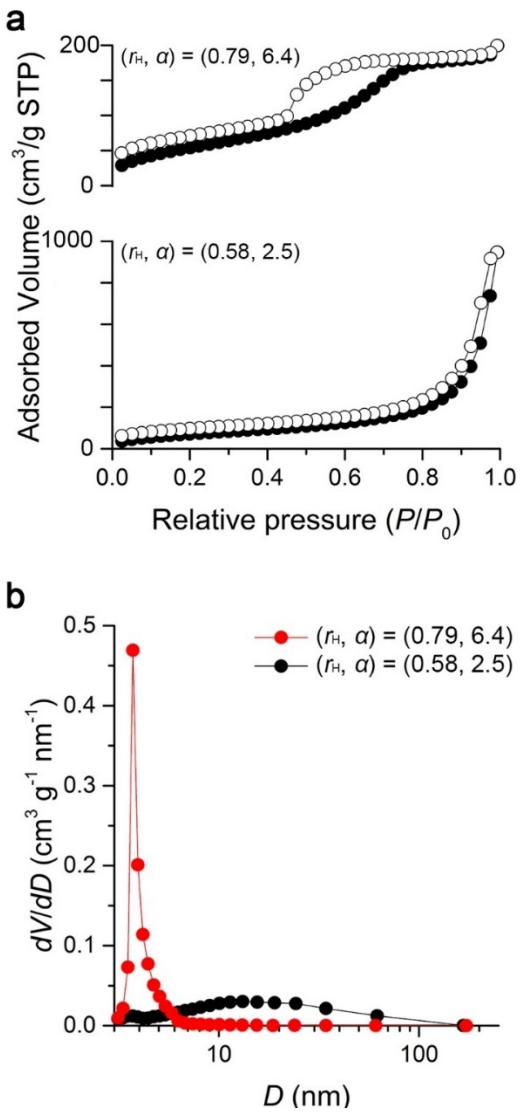

Figure 4.17. (a) Nitrogen sorption isotherms of the Series 3 with PLA-OH of 11 kg mol^{-1} obtained at 77.3 K (filled circles: adsorption branch; open circles: desorption branch). (b) Pore size distribution as a function of pore diameter (D) based on BJH analysis of the desorption branch in (a).

The macroporous characteristic of the (r_H, α) = (0.79, 6.4) porous polymer was evaluated by mercury intrusion porosimetry. This data is shown in Figure 4.18 in comparison to (r_H, α) = (0.9, 0.3), where no distinct macrophase separation was detected. As expected, the intrusion data of (r_H, α) = (0.79, 6.4) clearly exhibits two step-like increases in the

amount of intruded mercury at D = 0.85 μm and 22 nm, corroborating the hierarchical pore structure comprising of macropores and mesopores. When compared to (r_H, α) = (0.79, 6.4), the intrusion data of (r_H, α) = (0.9, 0.3) showed a larger pore volume with a rather broad distribution of pore sizes mostly in the mesopore regime, consistent with the nitrogen sorption isotherm analysis.

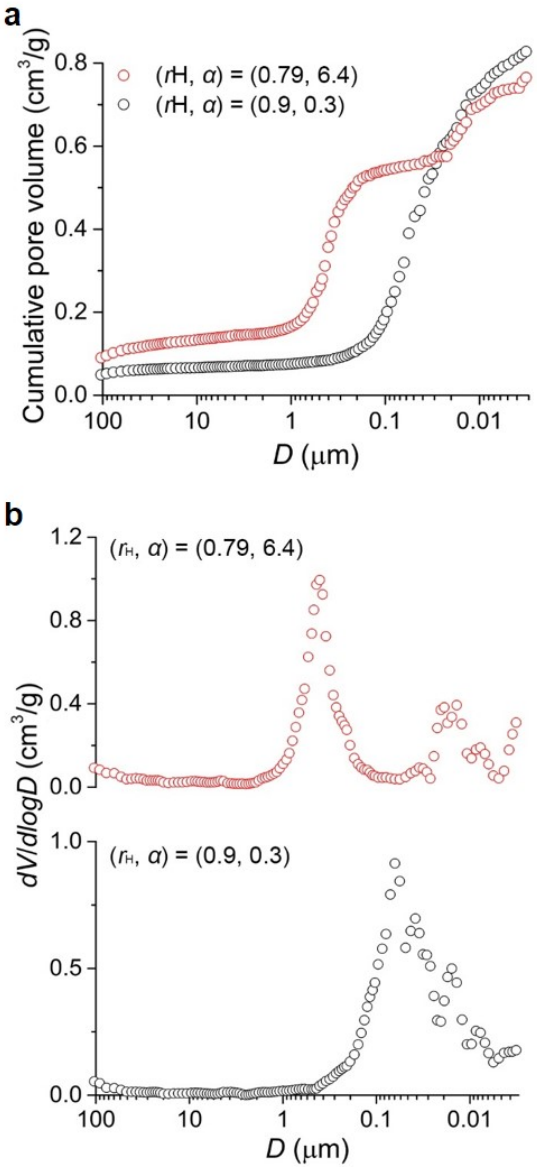

Figure 4.18. Representative mercury intrusion porosimetry data of Series 3 (a) Cumulative pore volume as a function of pore diameter (D). (b) Corresponding pore size distribution as a function of D derived from the cumulative volume (V) data.

4.4 Discussion

Analysis of the cross-linked precursors prepared in the presence of PLA-OH and the corresponding porous polymers indicate that PLA-OH selectively swells the PLA

microdomain generated by PIMS if the PLA-OH can be accommodated within the forming PLA microdomain (i.e., below the solubility limit). If the amount of PLA-OH exceeds the solubility limit during copolymerization of S and DVB, PLA-OH is excluded from the forming block polymer, inducing macrophase separation (i.e., PIPS) between PLA-OH and the block polymer. We demonstrate that the ratio of PLA-CTA to PLA-OH in weight (r_H) and molar mass (α) affects the solubility limit of the system. This is generally consistent with the phase behavior of block copolymer/homopolymer blends documented in the literature.[28,31,34]

SAXS, SEM, nitrogen sorption isotherm, and mercury intrusion porosimetry data obtained from the Series 1 precursors and the porous polymers suggests that the solubility limit is reached when $r_H \sim 0.9$. We note that w_{PLA} was fixed as 0.3 and PLA-CTA and PLA-OH with similar M_w (17 and 18 kg mol^{-1}, respectively) were used in Series 1. When $r_H \leq 0.9$, the addition of PLA-OH gradually increased the domain spacing ($d = 2\pi/q^*$) by selective swelling of the PLA microdomain. As the pores are derived by etching of the PLA microdomain, the pore diameter (D) also gradually increased as a function of r_H to generate mesopores in the range of 6 nm ($r_H = 0$) to 39 nm ($r_H = 0.9$) determined by nitrogen sorption analysis, which offers a route to precise control over pore size by adjusting r_H. Figure 4.19a shows changes in the length scale of the porous polymers in the mesoporous regime as a function of r_H as determined by SAXS (d), nitrogen sorption isotherm (mode pore diameter, D_{max}), and mercury intrusion porosimetry (D_{max}) analyses, respectively. SAXS and nitrogen sorption isotherm data showed good correlation

between the characteristic length scale and r_H, while the tendency was less apparent in mercury intrusion porosimetry data presumably because the technique is more optimized for the analysis of macroporous samples.

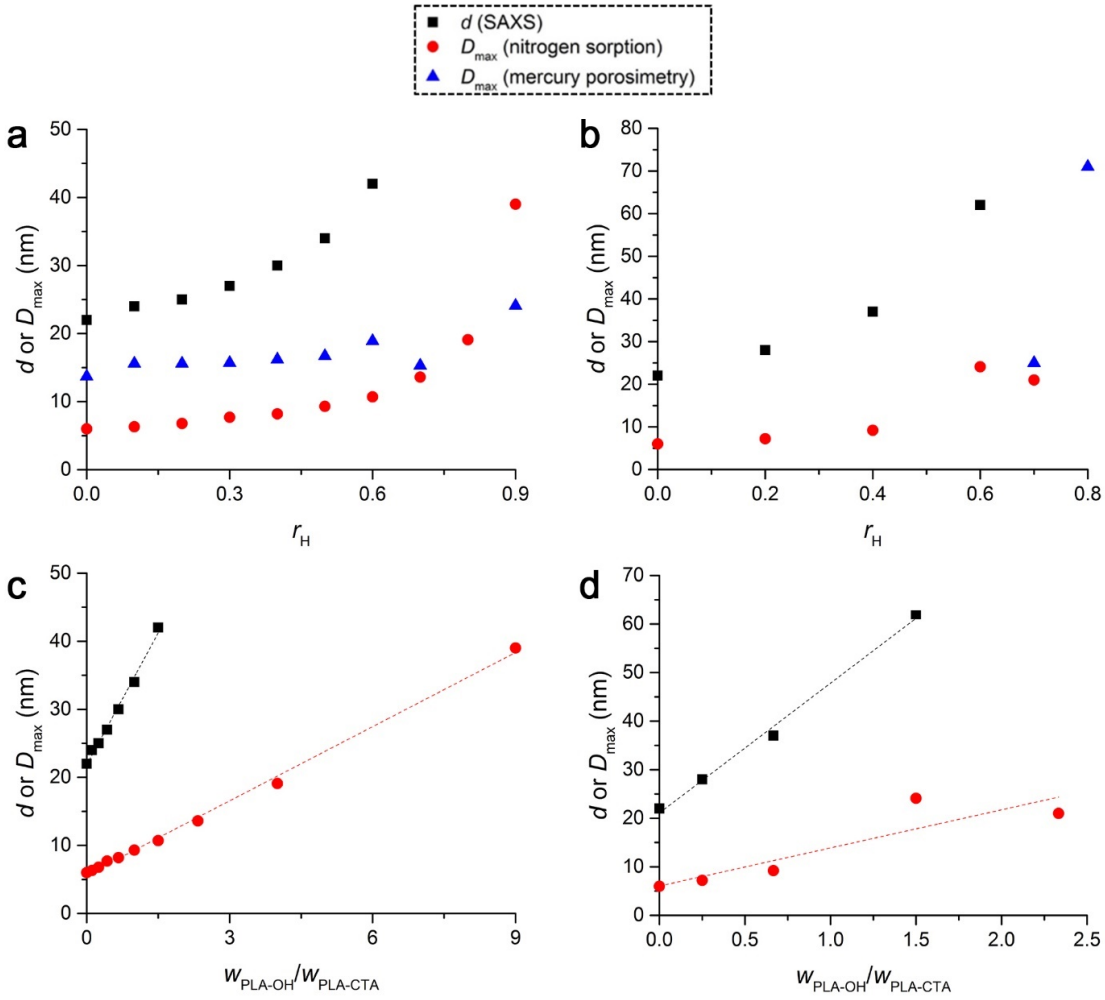

Figure 4.19. The plot of domain spacing (d) and mode pore diameter (D_{max}) vs. r_H (≤ 0.9) of Series 1 (a) and Series 2 (b) in the mesoporous regime. d (black squares) was estimated by SAXS analysis, and D_{max} was obtained from nitrogen sorption isotherm analysis (red circles) and mercury intrusion porosimetry analysis (blue triangles), respectively. The plot of d estimated from SAXS and D_{max} obtained from nitrogen sorption vs $w_{PLA\text{-}OH}/w_{PLA\text{-}CTA}$ of Series 1 (c) and Series 2 (d).

We found that the data shows a linear relationship when the length scales of the porous polymers were plotted versus the weight ratio of PLA-OH to PLA-CTA ($w_{PLA\text{-}OH}/w_{PLA\text{-}CTA}$) (Figure 4.19c). This tendency is intriguing but is not fully consistent with the literature where the relationship $d \sim \varphi^{-\beta}$ was suggested (φ is volume concentration of a homopolymer in the mixture of a diblock copolymer with the homopolymer, and β is a constant).[31] We do not have a definitive explanation on the behavior at this moment.

The bicontinuous disordered morphology persists over a range of compositions due to in situ cross-linking, which traps the disordered morphology of the emergent block polymer PLA-*b*-P(S-*co*-DVB) and prevents transition to an ordered phase.[15] Increasing r_H from 0 to 0.9 corresponds to the increase in [M (S + DVB)]:[PLA-CTA] from 80:1 to 810:1, and successful control over the pore size and the pore structure suggests that copolymerization of S and DVB proceeds in a controlled manner via RAFT process in this [M]:[PLA-CTA] range. We note that the molar mass of the P(S-*co*-DVB) block in PLA-*b*-P(S-*co*-DVB) would also increase as r_H increases.

When $0.9 < r_H < 1$, a drastic increase in the pore size and formation of macropores was observed by mercury intrusion porosimetry analysis and supported by SEM micrographs. Although the macropore volume and the macropore size seem to roughly increase as r_H increases, the data was rather scattered and the distributions were often not unimodal which suggests heterogeneity in the materials. It is likely that the system undergoes phase separation mainly via PIPS mechanism between PLA-OH and the growing block

polymer. Due to the high [M]:[PLA-CTA] ratio in the polymerization mixture, the P(S-*co*-DVB) fraction is enriched in PLA-b-P(S-*co*-DVB) in the early stage of polymerization resulting in increased incompatibility with PLA-OH. Indeed, the polymerization mixture became opaque after ca. 30 min of polymerization, followed by a later stage gelation (Figure 4.20), indicating that macrophase separation was induced via PIPS mechanism prior to arresting of the morphology. This resulted in a modest control over pore size and pore volume (Figure 4.21). In contrast, gelation occurred without macrophase separation, as the polymerization mixture remained transparent, when $r_H \leq 0.9$. Also, as the amount of AIBN was set as 0.1 eq relative to PLA-CTA, the AIBN loading is very low when $0.9 < r_H < 1$ and we posit that unreacted monomer which remains after the polymerization is completed can be evaporated to form macropores. To confirm this hypothesis, we performed SEM imaging on the precursor polymers for $r_H = 0.92$ and 0.94 and observed macropores on the surface of precursors (Figure 4.21). This macroporous structure generated by evaporation of unreacted monomer is regarded as the origin of heterogeneity of samples in $0.9 < r_H < 1$.

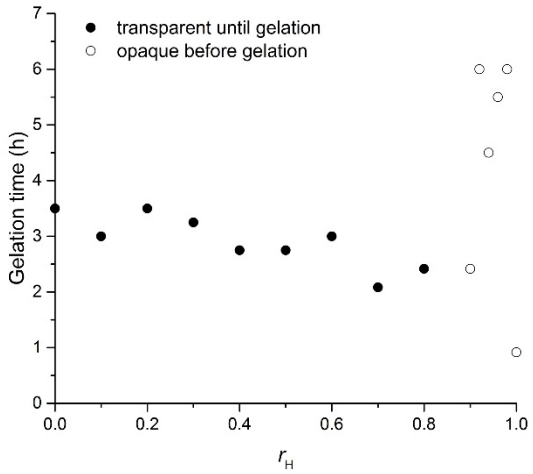

Figure 4.20. A plot of gelation time versus r_H in Series 1 samples.

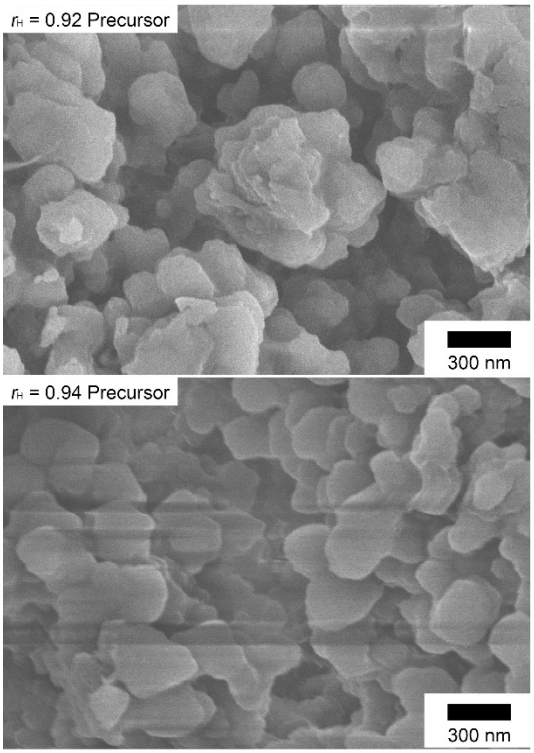

Figure 4.21. SEM image of Series 1 precursors with high r_H as indicated within each image. Samples were coated with Os prior to imaging.

When r_H = 1, normal free radical polymerization proceeded and phase separation occurred via the PIPS mechanism as there was no PLA-CTA in the polymerization mixture. It is known that the free radical copolymerization of S/DVB produces a heterogeneous network of densely cross-linked microgel particles in comparison to the homogeneous network structure formed via controlled radical polymerization processes such as RAFT.[21,38] While a cross-linked precursor was rapidly produced with high yield (> 90 wt%), presumably because of accelerated polymerization via the Trommsdorff effect, the porous polymer derived from the precursor revealed a rather irregular pore structure with a high degree of heterogeneity compared to the porous polymers obtained with $r_H \leq 0.9$.

In case of the Series 2, all the conditions were identical to Series 1 including molar masses of PLA-CTA and PLA-OH and w_{PLA} (0.3) except that molecular CTA was added to maintain the [M]:[total CTA] ratio. We visually monitored the polymerization mixtures over the course of the polymerization, and found that the polymerization mixture became opaque prior to gelation when $r_H > 0.8$ in the Series 2, unlike Series 1 which required a larger r_H (> 0.9).

The ability to tune the length scale of the porous polymers obtained from Series 2 is shown in Figure 4.19 as a function of r_H. Additionally, the length scales of the porous polymers were plotted versus $w_{PLA\text{-}OH}/w_{PLA\text{-}CTA}$. Compared with Series 1, the length scale increased more rapidly as r_H increased and a transition from the meso- to macroporous regimes was observed at $r_H = 0.6$. We posit that the formation of P(S-*co*-DVB) from the molecular CTA drives the system towards macrophase separation resulting in a larger increase in the associated length scale. Prior to gelation, the Series 2 polymerization mixture contains the species: PLA-OH, PLA-*b*-P(S-*co*-DVB), P(S-*co*-DVB), S, and DVB. As r_H increases, the concentration of PLA-*b*-P(S-*co*-DVB) decreases while the concentrations of PLA-OH and P(S-*co*-DVB) increase and the system may be considered as a pseudo-ternary blend of PLA and P(S-*co*-DVB) homopolymers with PLA-*b*-P(S-*co*-DVB) block polymer in a solution of unreacted S and DVB. Eventually the P(S-*co*-DVB) is fused to the cross-linked polystyrenic network as the polymerization mixture becomes a macroscopic gel.

While the PIMS process may be dominant at low r_H values where selective swelling of PLA and P(S-*co*-DVB) microdomains occurs with PLA-OH and P(S-*co*-DVB), respectively, we suggest that the structuring mechanism gradually changes to PIPS as r_H increases where the PLA-*b*-P(S-*co*-DVB) block polymer stabilizes the interface between PLA-OH and P(S-*co*-DVB) domains. Compared with Series 1 where the PIPS process produced a heterogeneous morphology at $r_H > 0.9$, the addition of the molecular CTA to the Series 2 polymerization mixture allows the system to undergo macrophase separation at high r_H while still polymerizing by the controlled RAFT mechanism to produce a well-defined macroscopic bicontinuous morphology, similar to reported literature.[24,25,27] Mercury intrusion porosimetry data supports improved control over the length scale in the macroporous regime for Series 2 porous polymers.

The data obtained from Series 3 shows the remarkable versatility of the system and the ability to produce polymers with a high degree of porosity. These results suggest that α has a profound impact on the solubility limit of PLA-OH during polymerization. As indicated in the literature, selective swelling of the microdomain by a homopolymer is likely to happen at $\alpha < 1$ while macrophase separation of the homopolymer and the block polymer occurs when $\alpha > 1$.[34] In the latter case, microphase separation will also occur in the block polymer-rich domains resulting in a hierarchical morphology.

Indeed, a hierarchical morphology is observed when α = 6.4 ($M_{w,PLA\text{-}CTA}$ = 11 and $M_{w,PLA\text{-}OH}$ = 70 kg mol^{-1}) and $w_{PLA\text{-}OH}$ = 0.31. The combined macro- and microphase separation (PIPS/PIMS) induces the hierarchical structure which is confirmed by mercury intrusion porosimetry data (Figure 4.18). In comparison with the analogous system, where PEO was used as the PLA-selective additive, a similar morphology was obtained at α = 1.3, when all other compositional variables were identical.[18] In the case of PLA homopolymer acting as the PLA-selective additive, a higher α value was required to produce the hierarchical morphology. When α = 2.5 ($M_{w,PLA\text{-}CTA}$ =11 and $M_{w,PLA\text{-}OH}$ = 28 kg mol^{-1}), it appears that some fraction of PLA-OH remained in the PLA microdomain formed by the PIMS process, but the remainder of the PLA-OH was segregated from the polymerization mixture contributing to the formation of macropores. We posit that the mixed behavior may be a result of the in situ cross-linking process which kinetically arrests the phase-separated morphology. Also, we note that the presence of unreacted monomer in the macro- and microphase separation processes reduces the segregation strength of the system compared to a blend of a block copolymer and a homopolymer in the bulk. The samples prepared with α = 0.6 ($M_{w,PLA\text{-}CTA}$ = 35 and $M_{w,PLA\text{-}OH}$ = 21 kg mol^{-1}) showed an increase in size of PLA microdomain as $w_{PLA\text{-}OH}$ increased via selective swelling of the PLA microdomain. Consistent with α < 1, macrophase separation was not observed from these polymerized mixtures.

4.5 Conclusions

The phase separation behavior of cross-linked polymers generated from polymerization mixtures containing PLA-CTA, S, DVB, PLA-OH, and CTA and the corresponding porous polymers were systematically investigated by combining SAXS, SEM, nitrogen sorption isotherm, and mercury intrusion porosimetry analyses. Starting from a polymerization mixture consisting of PLA-CTA, S, and DVB where PIMS produces a disordered bicontinuous morphology, gradually replacing PLA-CTA with PLA-OH of similar molar mass resulted in an increase in the length scale of the resulting bicontinuous morphology. Increasing the length scale by selectively swelling the PLA microdomain with PLA-OH allows for precise control pore size in the mesoporous regime. When PLA-OH was above the solubility limit, the polymerization mixture turned opaque prior to gelation and produced macroporous polymers without reliable control over pore size, presumably due to low concentrations of PLA-CTA and AIBN. Addition of CTA to the polymerization mixture to maintain a constant [M]:[total CTA] ratio ensured that the RAFT process proceeds even in the absence of PLA-CTA (i.e., PIPS also occurs via RAFT polymerization) and control over pore size in the macroporous regime was achieved. While addition of small molar mass PLA-OH was efficient for increasing mesopore volume by selective swelling of the PLA microdomain, it was possible to produce simultaneous micro- and macrophase separation by addition of high molar mass PLA-OH which generated hierarchically porous polymers containing meso- and macropores. The facile ability to control the length scale of the bicontinuous morphology, using a small library of PLA precursors, over the nanometer to micrometer length scales

suggests great promise for this methodology to produce a variety of porous polymers with 3D continuous pore structure.

4.6 References

1) Meuler, A. J.; Hillmyer, M. A.; Bates, F. S. Ordered Network Mesostructures in Block Polymer Materials. *Macromolecules* **2009**, *42*, 7221–7250.

2) Seo, M.; Hillmyer, M. A. Reticulated Nanoporous Polymers by Controlled Polymerization-Induced Microphase Separation. *Science.* **2012**, *336*, 1422–1425.

3) Sai, H.; Tan, K. W.; Hur, K.; Asenath-Smith, E.; Hovden, R.; Jiang, Y.; Riccio, M.; Muller, D. A.; Elser, V.; Estroff, L. A.; Gruner, S. M.; Wiesner, U. Hierarchical Porous Polymer Scaffolds from Block Copolymers. *Science* **2013**, *341*, 530–534.

4) Zhang, Y.; Sargent, J. L.; Boudouris, B. W.; Phillip, W. A. Nanoporous Membranes Generated from Self-Assembled Block Polymer Precursors: *Quo Vadis*? *J. Appl. Polym. Sci.* **2015**, *132*, 41683.

5) Nischang, I.; Teasdale, I.; Brüggemann, O. Porous Polymer Monoliths for Small Molecule Separations: Advancements and Limitations. *Anal. Bioanal. Chem.* **2011**, *400*, 2289–2304.

6) Olson, D. A.; Chen, L.; Hillmyer, M. A. Templating Nanoporous Polymers with Ordered Block Copolymers. *Chem. Mater.* **2008**, *20*, 869–890.

7) Ndoni, S.; Vigild, M. E.; Berg, R. H. Nanoporous Materials with Spherical and Gyroid Cavities Created by Quantitative Etching of Polydimethylsiloxane in Polystyrene - Polydimethylsiloxane Block Copolymers. *J. Am. Chem. Soc.* **2003**, *125*, 13366–13367.

8) Li, L.; Schulte, L.; Clausen, L. D.; Hansen, K. M.; Jonsson, G. E.; Ndoni, S. Gyroid Nanoporous Membranes with Tunable Permeability. *ACS Nano* **2011**, *5*, 7754–7766.

9) Schulte, L.; Grydgaard, A.; Jakobsen, M. R.; Szewczykowski, P. P.; Guo, F.; Vigild, M. E.; Berg, R. H.; Ndoni, S. Nanoporous Materials from Stable and Metastable Structures of 1,2-PB-*b*-PDMS Block Copolymers. *Polymer* **2011**, *52*, 422–429.

10) Mao, H.; Hillmyer, M. A. Macroscopic Samples of Polystyrene with Ordered Three-Dimensional Nanochannels. *Soft Matter* **2006**, *2*, 57–59.

11) Morkved, T. L.; Stepanek, P.; Krishnan, K.; Bates, F. S.; Lodge, T. P. Static and Dynamic Scattering from Ternary Polymer Blends: Bicontinuous Microemulsions, Lifshitz Lines, and Amphiphilicity. *J. Chem. Phys.* **2001**, *114*, 7247–7259.

12) Zhou, N.; Bates, F. S.; Lodge, T. P. Mesoporous Membrane Templated by a Polymeric Bicontinuous Microemulsion. *Nano Lett.* **2006**, *6*, 2354–2357.

13) Barrett, E. P.; Joyner, L. G.; Halenda, P. P. The Determination of Pore Volume and Area Distributions in Porous Substances. I. Computations from Nitrogen Isotherms. *J. Am. Chem. Soc.* **1951**, *73*, 373–380.

14) Schulze, M. W.; McIntosh, L. D.; Hillmyer, M. A.; Lodge, T. P. High-Modulus, High-Conductivity Nanostructured Polymer Electrolyte Membranes via Polymerization-Induced Phase Separation. *Nano Lett.* **2014**, *14*, 122–126.

15) McIntosh, L. D.; Schulze, M. W.; Irwin, M. T.; Hillmyer, M. A; Lodge, T. P. Evolution of Morphology, Modulus, and Conductivity in Polymer Electrolytes Prepared via Polymerization-Induced Phase Separation. *Macromolecules* **2015**, *48*, 1418–1428.

16) Oh, J.; Seo, M. Photoinitiated Polymerization-Induced Microphase Separation for the Preparation of Nanoporous Polymer Films. *ACS Macro Lett.* **2015**, *4*, 1244–1248.

17) Seo, M.; Kim, S. S.; Oh, J.; Kim, S. S.; Hillmyer, M. A. Hierarchically Porous Polymers from Hyper-Cross-Linked Block Polymer Precursors. *J. Am. Chem. Soc.* **2015**, *137*, 600–603.

18) Saba, S. A.; Mousavi, M. P. S.; Bühlmann, P.; Hillmyer, M. A. Hierarchically Porous Polymer Monoliths by Combining Controlled Macro- and Microphase Separation. *J. Am. Chem. Soc.* **2015**, *137*, 8896–8899.

19) Chan, P. K.; Rey, A. D. Polymerization-Induced Phase Separation. 1. Droplet Size Selection Mechanism. *Macromolecules* **1996**, *29*, 8934–8941.

20) Chan, P. K.; Rey, A. D. Polymerization-Induced Phase Separation. 2. Morphological Analysis. **1997**, *30*, 2135–2143.

21) Viklund, C.; Svec, F.; Fréchet, J. M. J.; Irgum, K. Monolithic, "Molded", Porous Materials with High Flow Characteristics for Separations, Catalysis, or Solid-Phase Chemistry: Control of Porous Properties during Polymerization. *Chem. Mater.* **1996**, *8*, 744–750.

22) Sherrington, D. C. Preparation, Structure and Morphology of Polymer Supports. *Chem. Commun.* **1998**, *21*, 2275–2286.

23) Peters, E. C.; Svec, F.; Fréchet, J. M. J.; Viklund, C.; Irgum, K. Control of Porous Properties and Surface Chemistry in "Molded" Porous Polymer Monoliths Prepared by Polymerization in the Presence of TEMPO. *Macromolecules* **1999**, *32*, 6377–6379.

24) Meyer, U.; Svec, F.; Fréchet, J. M. J.; Hawker, C. J.; Irgum, K. Use of Stable Free Radicals for the Sequential Preparation and Surface Grafting of Functionalized Macroporous Monoliths. *Macromolecules* **2000**, *33*, 7769–7775.

25) Kanamori, K.; Nakanishi, K.; Hanada, T. Rigid Macroporous Poly(divinylbenzene) Monoliths with a Well-Defined Bicontinuous Morphology Prepared by Living Radical Polymerization. *Adv. Mater.* **2006**, *18*, 2407–2411.

26) Kanamori, K.; Hasegawa, J.; Nakanishi, K.; Hanada, T. Facile Synthesis of Macroporous Cross-Linked Methacrylate Gels by Atom Transfer Radical Polymerization. *Macromolecules* **2008**, *41*, 7186–7193.

27) Hasegawa, J.; Kanamori, K.; Nakanishi, K.; Hanada, T.; Yamago, S. Pore Formation in Poly(divinylbenzene) Networks Derived from Organotellurium-Mediated Living Radical Polymerization. *Macromolecules* **2009**, *42*, 1270–1277.

28) Barlow (née Tan), K. J.; Hao, X.; Hughes, T. C.; Hutt, O. E.; Polyzos, A.; Turner, K. A.; Moad, G. Porous, Functional, Poly(styrene-*co*-divinylbenzene) Monoliths by RAFT Polymerization. *Polym. Chem.* **2014**, *5*, 722–732.

29) Barlow, K. J.; Bernabeu, V.; Hao, X.; Hughes, T. C.; Hutt, O. E.; Polyzos, A.; Turner, K. A.; Moad, G. Triphenylphosphine-Grafted, RAFT-Synthesised, Porous Monoliths as Catalysts for Michael Addition in Flow Synthesis. *React. Funct. Polym.* **2015**, *96*, 89–96.

30) Liu, K.; Aggarwal, P.; Tolley, H. D.; Lawson, J. S.; Lee, M. L. Fabrication of Highly Cross-Linked Reversed-Phase Monolithic Columns via Living Radical Polymerization. *J. Chromatogr. A* **2014**, *1367*, 90–98.

31) Lai, C.; Russel, W. B.; Register, R. A. Scaling of Domain Spacing in Concentrated Solutions of Block Copolymers in Selective Solvents. *Macromolecules* **2002**, *35*, 4044–4049.

32) Winey, K. I.; Thomas, E. L.; Fetters, L. J. Swelling a Lamellar Diblock Copolymer with Homopolymer: Influences of Homopolymer Concentration and Molecular Weight. *Macromolecules* **1991**, *24*, 6182–6188.

33) Hanley, K. J.; Lodge, T. P.; Huang, C.-I. Phase Behavior of a Block Copolymer in Solvents of Varying Selectivity. *Macromolecules* **2000**, *33*, 5918–5931.

34) Hamley, I.W. The Physics of Block Copolymers, Oxford University Press Inc., New York, **1998**, pp. 331-412.

35) Bates, F. S.; Wiltzius, P. Spinodal Decomposition of a Symmetric Critical Mixture of Deuterated and Protonated Polymer. *J. Chem. Phys.* **1989**, *91*, 3258–3274.

36) Webb, P.A.; Orr, C. Analytical Methods in Fine Particle Technology, Micromeritics Instrument Corp., **1997**.

37) Xie, S.; Allington, R. W.; Fréchet, J. M. J.; Svec, F. Porous Polymer Monoliths: An Alternative to Classical Beads. *Adv. Biochem. Eng. Biotechnol.* **2002**, *76*, 87–125.

38) Norisuye, T.; Morinaga, T.; Tran-cong-miyata, Q.; Goto, A.; Fukuda, T.; Shibayama, M. Comparison of the Gelation Dynamics for Polystyrenes Prepared by Conventional and Living Radical Polymerizations: A Time-Resolved Dynamic Light Scattering Study. *Polymer* **2005**, *46*, 1982–1994.

Chapter 5. Tricontinuous Nanostructured Polymers via Polymerization-Induced Microphase Separation

5.1 Introduction

Tricontinuous morphologies of segmented multiblock polymers are useful in technologies requiring disparate properties in a single material, which may include multiple mechanical attributes such as high ultimate elongation, elastic modulus, and impact strength[1] or a combination of mechanical rigidity, ion conductivity, and electron conductivity.[2] One route to such materials relies on the self-assembly of block polymers that can adopt structures with multiple, continuous, and independent networks.[3–6] Recently, the selective etching of one or more segments was demonstrated and resulted in a mesoporous (pore size 2 – 50 nm) polymer with two distinct pore networks.[7] Alternatively, disordered tricontinuous morphologies have been produced through the phase separation of polymer blends. In these cases, the structure comprises of one phase segregating to the interface of two interpenetrating and incompatible domains.[8–10] We combine these two approaches to synthesize a disordered and cross-linked tricontinuous block polymer with three independent nonintersecting networks, two of which can be selectively etched with distinct chemistries to produce a mesoporous polymer.

Our group has reported the preparation of mesoporous polymers via polymerization-induced microphase separation (PIMS).[11] In this route, a poly(lactide) macro-chain transfer agent (PLA-CTA) is dissolved in a multifunctional monomer mixture of styrene

and divinylbenzene (DVB). The RAFT polymerization of the monomers induces microphase separation during incipient formation of a block polymer accompanied by in situ cross-linking that covalently fixes a disordered, bicontinuous structure. Selective hydrolytic etching of the PLA domains results in a percolating mesopore network over a wide range of compositions.[12,13]

5.2 Experimental Methods

Given that the incompatibility between poly(isoprene) (PI) and PLA is much greater than either polymer with poly(styrene),[14] we hypothesized that blends of PLA-CTA and PI-CTA could be used to prepare tricontinuous nanostructured polymers via PIMS if macrophase separation can be avoided. After initial optimization experiments, we settled on the polymerization of the mixture depicted in Figure 5.1, which comprised of PLA-CTA (25 wt%) and PI-CTA (25 wt%) co-dissolved in technical grade DVB (50 wt%).

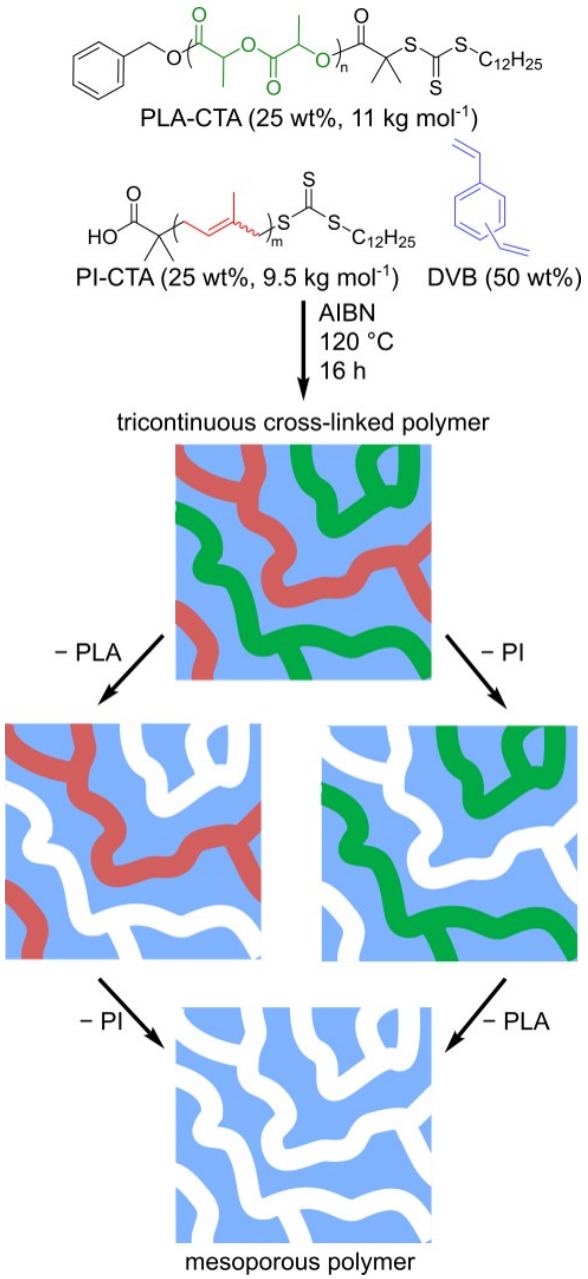

Figure 5.1. Preparation of tricontinuous mesoporous polymers via PIMS and orthogonal degradation of the PI and PLA blocks which produces a mesoporous polymer.

5.3 Results and Discussion

5.3.1 Properties of Nanostructured Polymer

Polymerization of the optimized reaction mixture resulted in 88 wt% conversion of the liquid precursor to an insoluble product. The unreacted volatile components (comprising 12 wt%) after polymerization were identified as ethylstyrene and DVB, as determined by ^{1}H NMR spectroscopy (Figure 5.2). The presence of unreacted DVB is likely due to hindered diffusion of monomer after network gelation and vitrification.[13] While thermal gravimetric analysis of the monoliths post-polymerization was not useful for determining the monolith composition (Figure 5.3a), differential scanning calorimetry (DSC) analysis of the as-synthesized monolith showed T_g's at –56 and 47 °C, from the PI and PLA blocks respectively, corroborating a microphase-separated structure containing PLA– and PI–rich domains (Figure 5.4a, top). The T_g values are close to their respective homopolymers indicating relatively pure microdomains.[15] At T > 100 °C the parent monolith exhibits an irreversible exotherm that we attribute to PI cross-linking (Figure 5.4 top, a); a third T_g for the crosslinked DVB microphase was not apparent by DSC. Dynamic mechanical analysis also did not reveal a T_g for the poly(DVB) microphase due to the high degree of cross-linking (Figure 5.4 bottom).

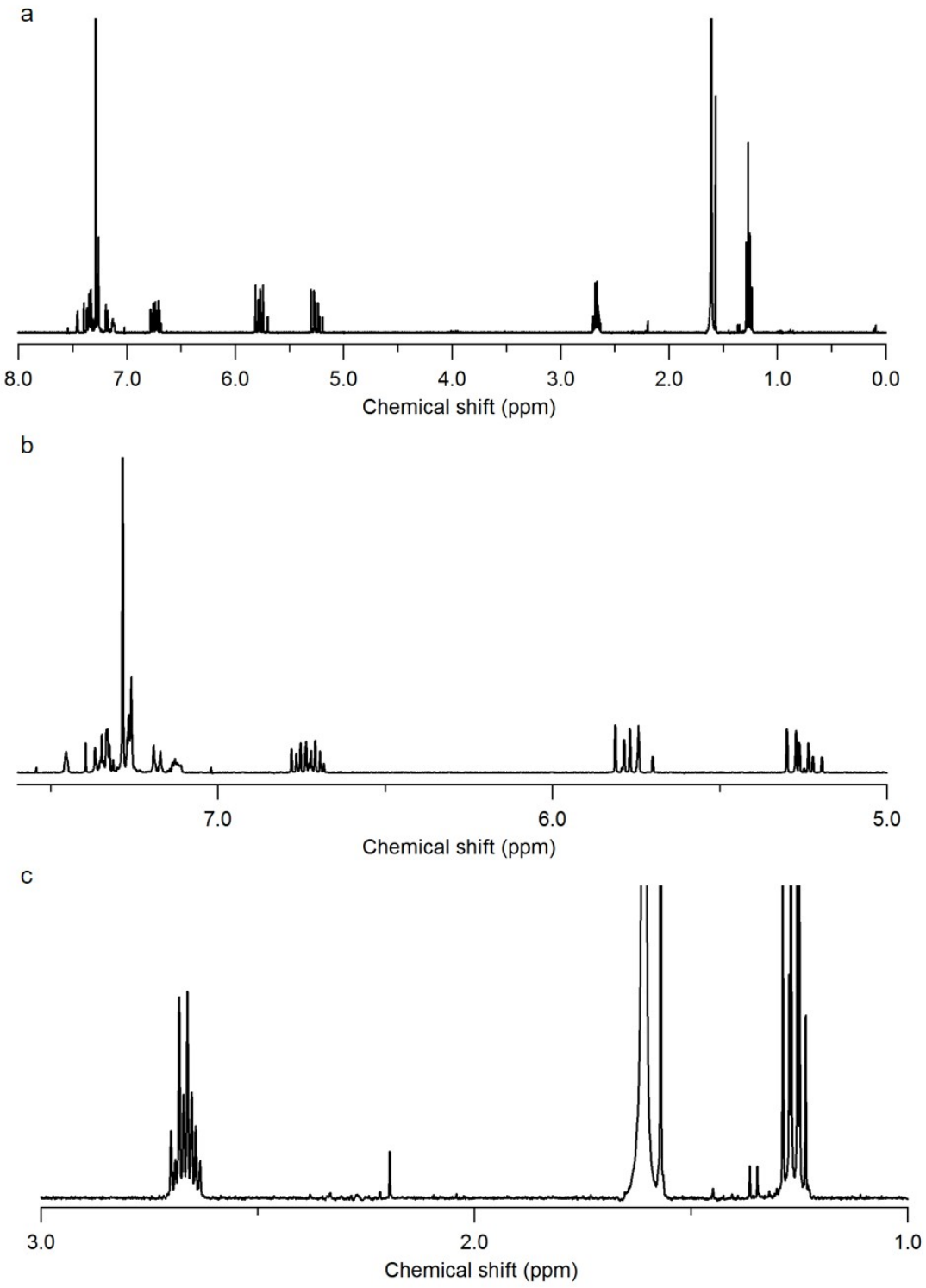

Figure 5.2. (a) ^{1}H NMR spectrum of remaining volatile components (divinylbenzene and ethylbenzene) after tricontinuous polymer synthesis. (b,c) Expansion of spectra.

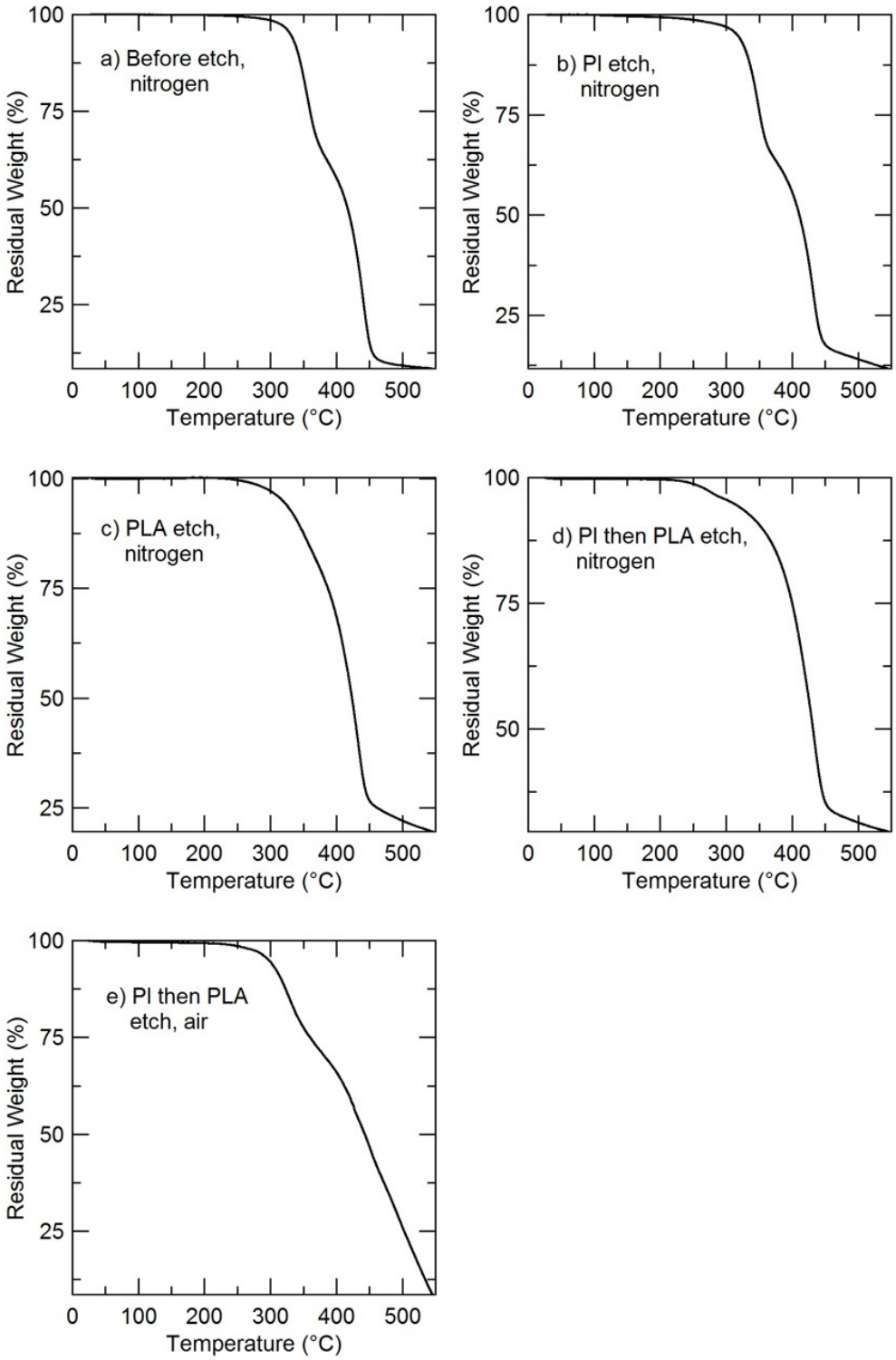

Figure 5.3. TGA profiles of tricontinuous polymers (a) before and (b–e) after etching. Samples were heated at 10 °C min^{-1} under nitrogen or air, as specified.

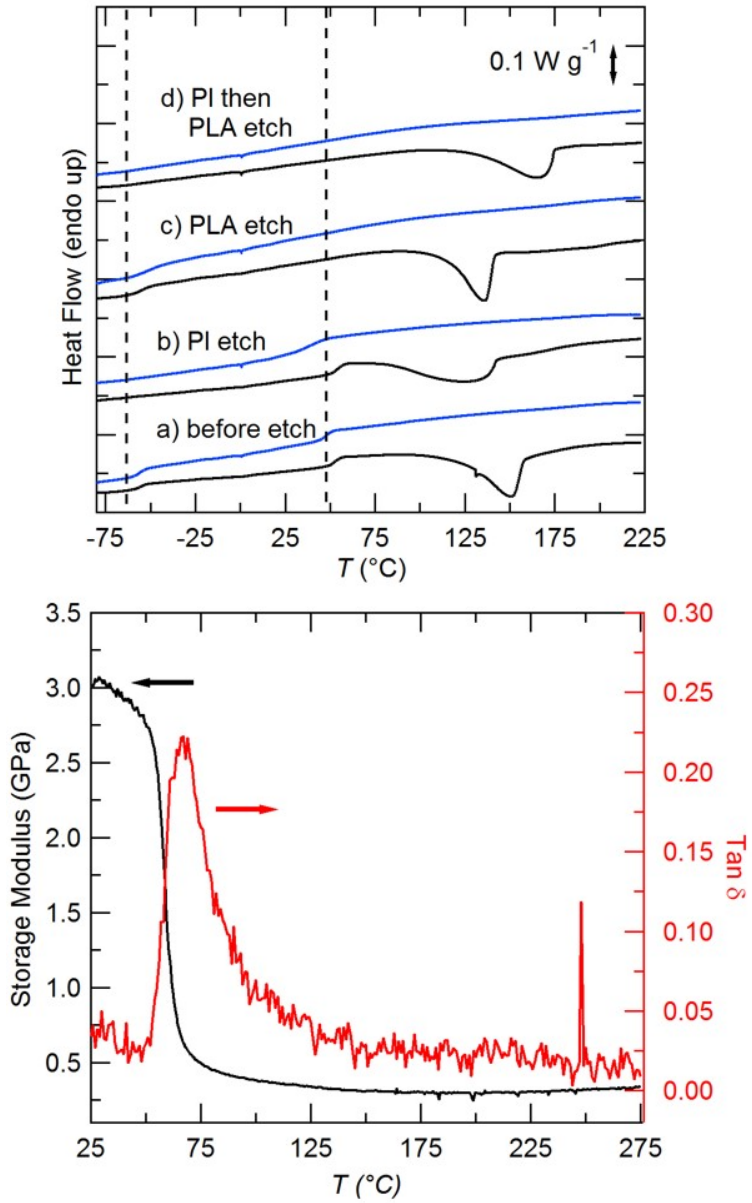

Figure 5.4. (top) DSC thermograms of tricontinuous nanostructured polymers (a) before and (b–d) after etching, as indicated. Black (lower) traces are upon heating and blue (upper) traces are upon re-heating at a ramp rate of 10 °C min^{-1}. The vertical dashed lines at –64 °C and 48 °C correspond to the T_g values of PI-CTA and PLA-CTA homopolymers, respectively. The exotherms at elevated temperatures are attributed to PI cross-linking in the polymer prior to etching, and additionally to partial pore collapse after etching. (bottom) Variation in the storage modulus, E', and tan δ of the tricontinuous nanostructured precursor prior to etching, measured by DMTA. The precipitous drop in the E' and maximum in tan δ, at 63 °C is close to the T_g of PLA as measured by DSC. No transition is observed for the PDVB block due to the high degree of cross-linking.

Further evidence of the disordered microphase-separated structure was revealed by SAXS where the broad maximum indicates overall compositional heterogeneities at the 16 nm length scale (Figure 5.5a). An image of the nanostructure was obtained in real space using transmission electron microscopy (TEM) (Figure 5.6a). Before TEM imaging, the polymer was stained with OsO_4 to provide contrast. OsO_4 stains the PI block rendering it darkest and leaves the PLA and PDVB unstained making these blocks the lightest in the TEM images.[16] A higher magnification TEM micrograph clearly shows the disordered microphase-separated structure, and the corresponding Fourier transform indicates compositional heterogeneities on the 14 nm length scale, consistent with SAXS (Figure 5.7).

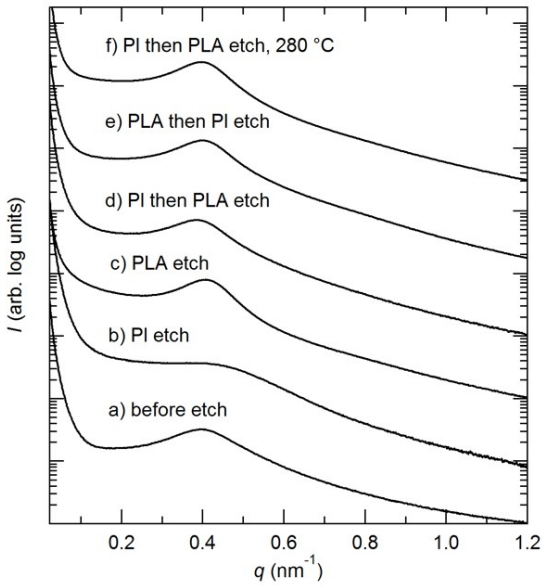

Figure 5.5. SAXS profiles acquired at room temperature (a) before and (b–e) after etching the tricontinuous nanostructured polymer. The single broad scattering peak at q^* = 0.40 nm^{-1} indicates compositional heterogeneities on the 16 nm length scale and the peak position is unaffected by etching, confirming the mechanical integrity of the matrix. (f) The mesoporous polymer after heating at a rate of 10 C min^{-1}. The mesoporous structure persists at 280 °C. Data are arbitrarily shifted vertically for clarity.

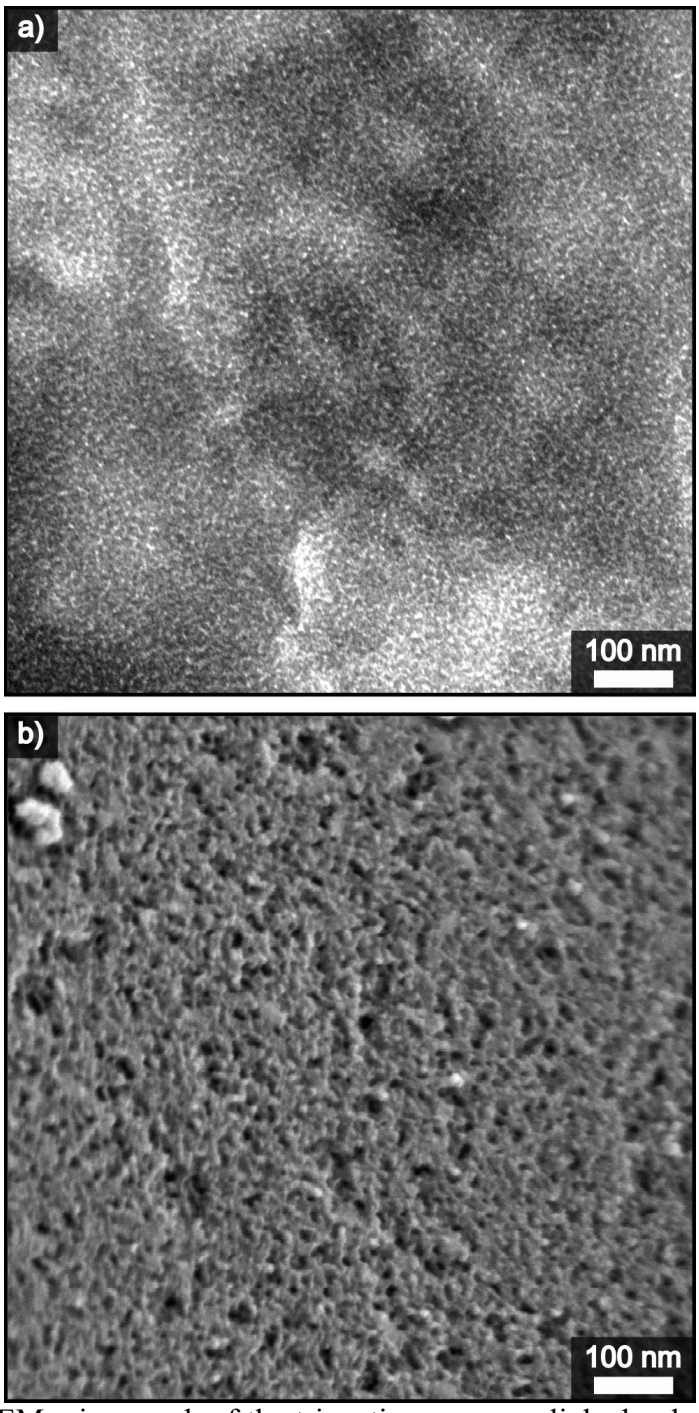

Figure 5.6. (a) TEM micrograph of the tricontinuous cross-linked polymer after staining with OsO_4. The larger length scale lighter and darker regions in the image are attributed to thickness variation across the sample. (b) SEM micrograph of the mesoporous polymer after etching both the PI and PLA blocks and coating with ca. 1 nm of Ir.

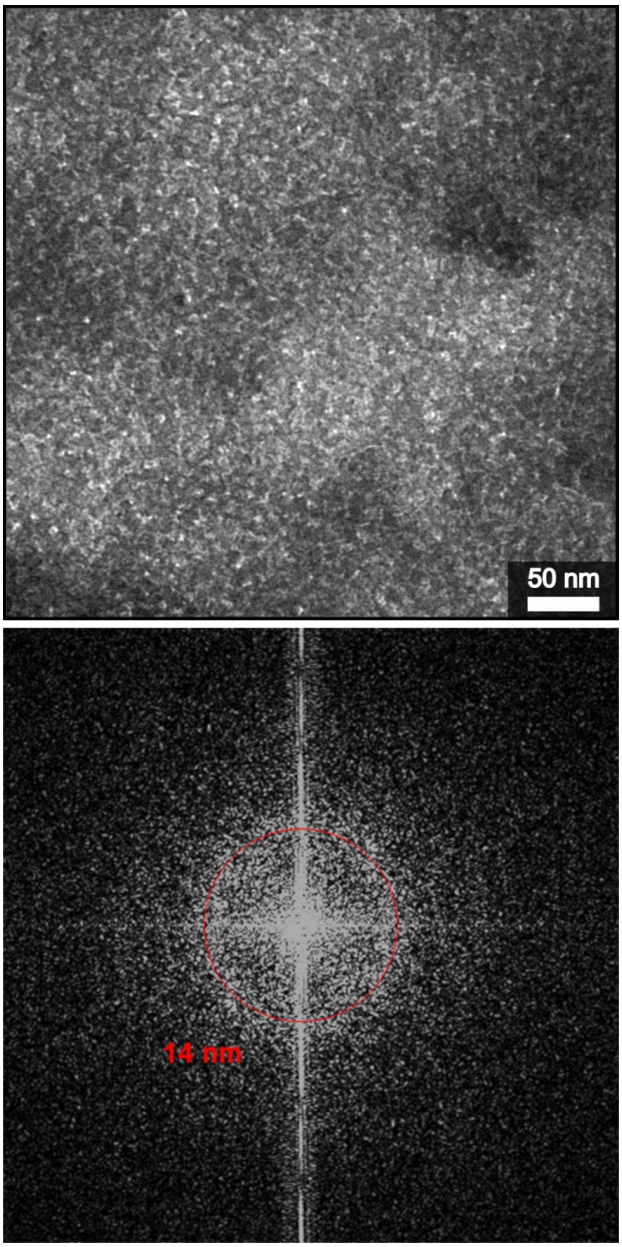

Figure 5.7. (top)Higher magnification TEM micrograph of a tricontinuous polymer prior to etching. The polymer was stained with OsO_4 for electron imaging. (bottom) FFT of TEM micrograph.

5.3.2 Properties of Mesoporous Polymer

The tricontinuity of the polymer was established through orthogonal etching, i.e. the PI and the PLA were independently etched by separate mechanisms. Etching of PLA from

disordered bicontinuous monoliths prepared via PIMS is well-established, and results in a pore network that should contain carboxylic acid groups lining the pore walls.[11] The selective etching of PI from other nanostructured block polymers to produce mesoporous materials has been accomplished by ozonolyis[17–20] and metathesis;[21,22] however, this process has generally only been applied to thin films. A few examples of PI etching from thicker films have been demonstrated, but this process typically requires stronger oxidation conditions including UV radiation[7] or a combination of UV and ozone.[23] A metathesis etching procedure was demonstrated for the removal of polybutadiene (PB) from microphase-separated monolithic PB-*b*-PLA, but the trisubstituted olefins in PI renders the metathesis degradation more challenging.[19,24] Thus, we developed a cross metathesis etching procedure to remove PI from bulk polymers using Grubbs second generation catalyst in cyclohexane with *trans*-4-octene as the cross metathesis reactant. PI is soluble in cyclohexane, while the PLA and PDVB blocks are insoluble, facilitating the selective removal of PI without compromising the mechanical integrity of the matrix. Using this approach, 82 wt% of the PI block was removed based on gravimetric analysis, producing a pore network that should contain alkene groups lining the pore walls. It is likely that the repeat units at the PI-PDVB interface are not accessible to the catalyst solution, which is consistent with results from a related system in which a chemical modification of a PI that lined the pore walls of a mesoporous PS matrix reached a maximum modification of 77 mol%.[16]

FTIR spectra are consistent with the selective etching of the PLA and PI (Figure 5.8). Furthermore, selective etching of the PI block results in the disappearance of only the lower T_g in DSC thermograms (Figure 5.4b), and, similarly, etching of the PLA block results in the disappearance of only the higher T_g (Figure 5.4c). Aspects of this disordered mesoporous structure, after removal of the PI or PLA block, are visible in scanning electron microscopy (SEM) (Figure 5.9) and the broad peak in SAXS profiles is consistent with coincidental length scales in the nanostructure pre- and post-etching (Figure 5.5b–e). After etching of both the PLA and PI blocks, an irreversible exotherm is still observed in DSC thermograms and, in this case, is attributed to partial pore collapse upon heating which reduces the surface energy of the nanostructure (Figure 5.4b–d).[25] SEM of the mesoporous polymer post etching both the PLA and PI shows a high degree of porosity (Figure 5.6b) and after heating in the DSC the sample shows a textured surface with some retained porosity (Figure 5.10). This polymer has improved thermal stability compared to non-crosslinked mesoporous poly(styrene), as the pore collapse exotherm is shifted by more than 30 °C to 125 °C.[25]

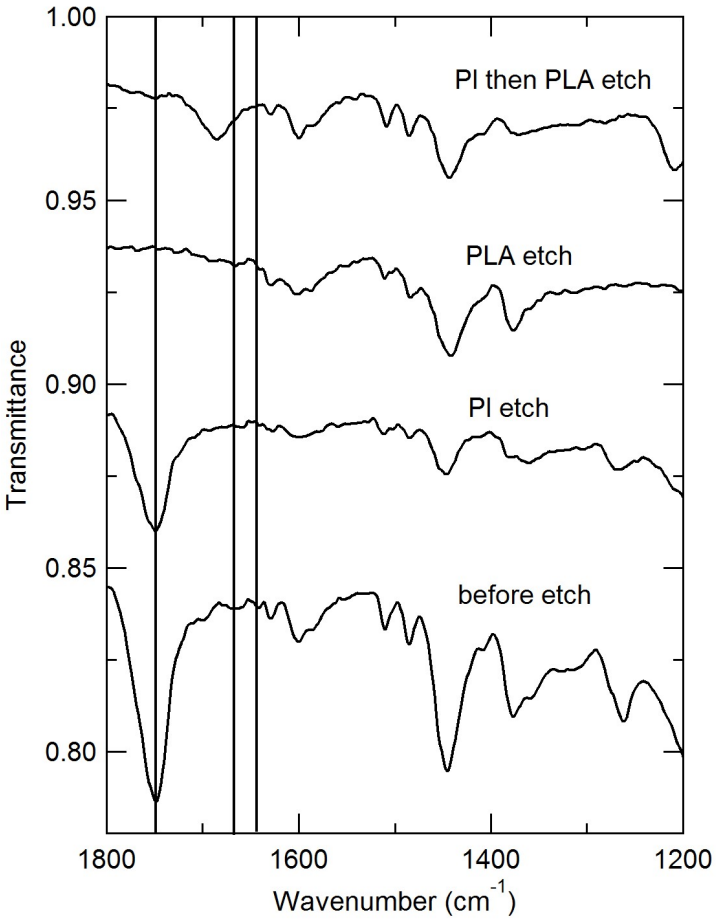

Figure 5.8. FTIR spectra of tricontinuous polymers before and after etching, as indicated in the plot. The disappearance of the carbonyl stretch, indicated by the vertical line at 1750 cm^{-1}, is consistent with PLA removal. The weak absorptions indicated at 1665 and 1645 cm^{-1} are the *trans* and *cis* C=C stretch of PI, respectively.

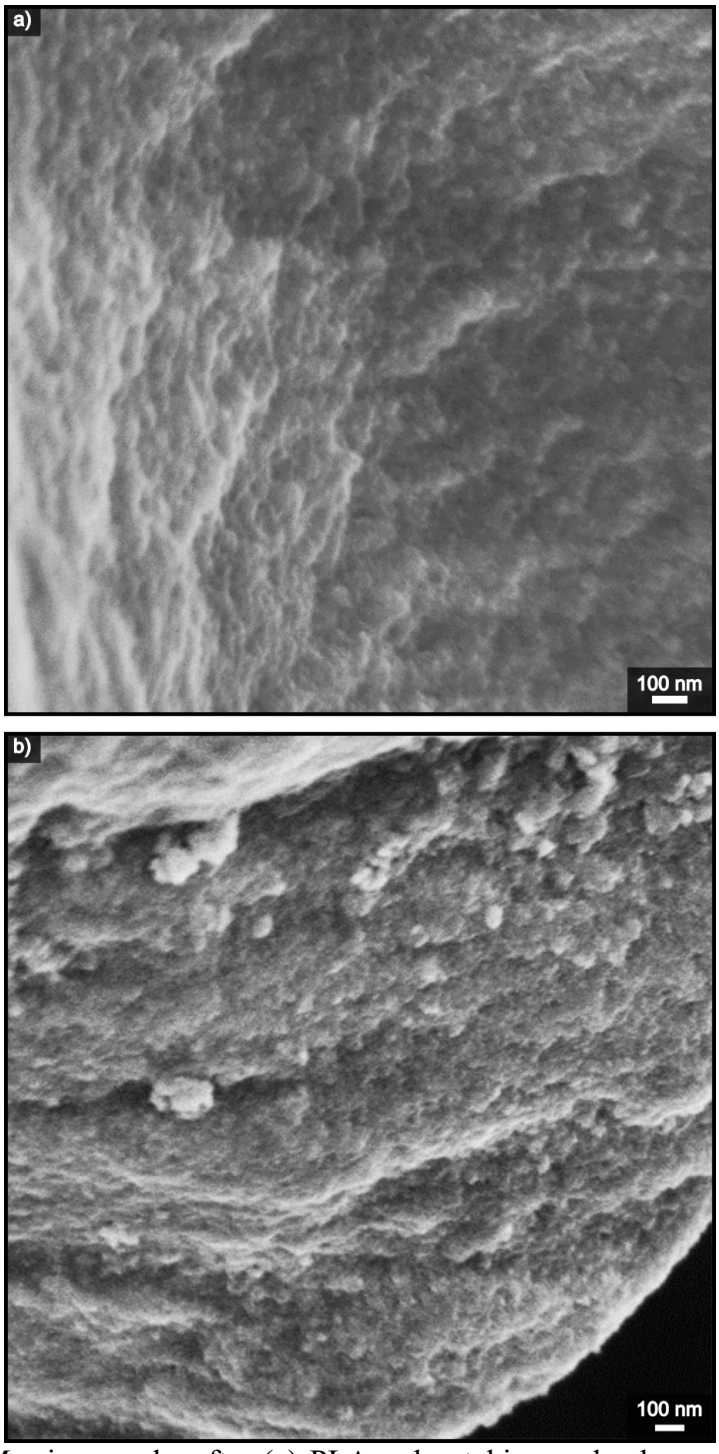

Figure 5.9. SEM micrographs after (a) PLA only etching and subsequent staining with OsO_4 or (b) PI only etching and subsequent staining with RuO_4. Even after staining, the polymers charged significantly under the electron beam and higher magnification images could not be readily obtained. Moreover, the anticipated small features sizes and relatively low void fraction make imaging challenging.

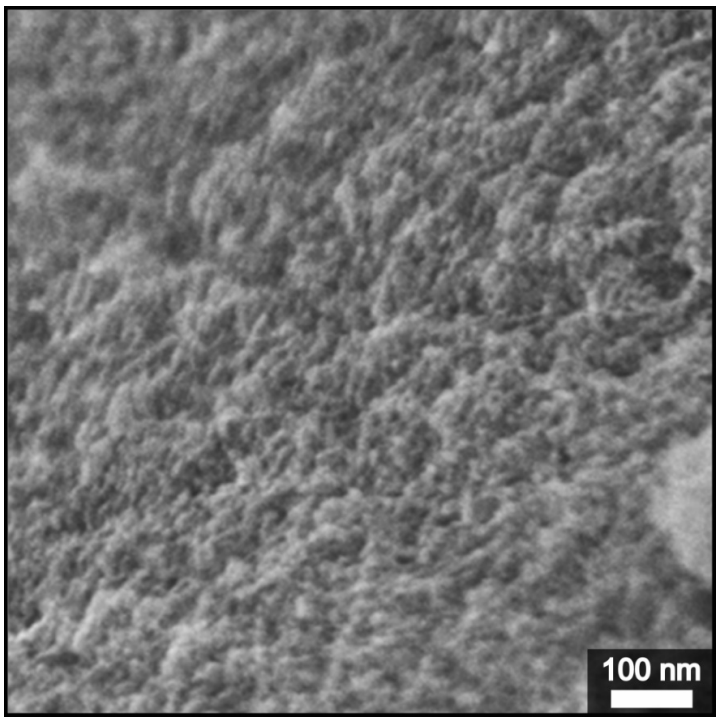

Figure 5.10. SEM micrograph of the after etching of both PLA and PI and then heating in the DSC to 225 °C. The sample was coated in ca. 1 nm Ir prior to electron imaging.

Nitrogen sorption analysis after each etch step gave Type IVa isotherms with H2a hysteresis, indicative of a disordered networked pore structure (Figure 5.11).[26] Orthogonal etching of both blocks, specifically PI etching followed by PLA etching, resulted in a significant increase in porosity. The BET specific surface area and pore volume is greater than the sum of the individual contributions, implying that there is some porosity that is only accessible after removal of both the PI and PLA.[27] Indeed, mesopore size distributions show a second population of smaller mesopores that are apparent only after orthogonal etching (Figure 5.12).[28] These sub-structural pores have been observed where inefficient chain packing results in additional porosity in the matrix block.[12,29] Our first attempts at etching PLA followed by etching PI were unsuccessful, as

the presence of residual base from the PLA etch caused early catalyst decomposition. Instead, etching PLA with trifluoroacetic acid, which was readily removed under vacuum, permitted the subsequent successful etching of PI.[30] Using this route, the mesoporous polymer had comparable porosity to the etching in the reverse order (Figures 5.12 and 5.13). Incredibly, due to the high degree of cross-linking in the PDVB matrix, approximately half of the porosity as determined by nitrogen sorption measurements (i.e., surface area and pore volume, Figure 5.14) is retained after heating at 280 °C for 30 min, and the mesostructure can still be seen in SAXS and SEM (Figure 5.15).

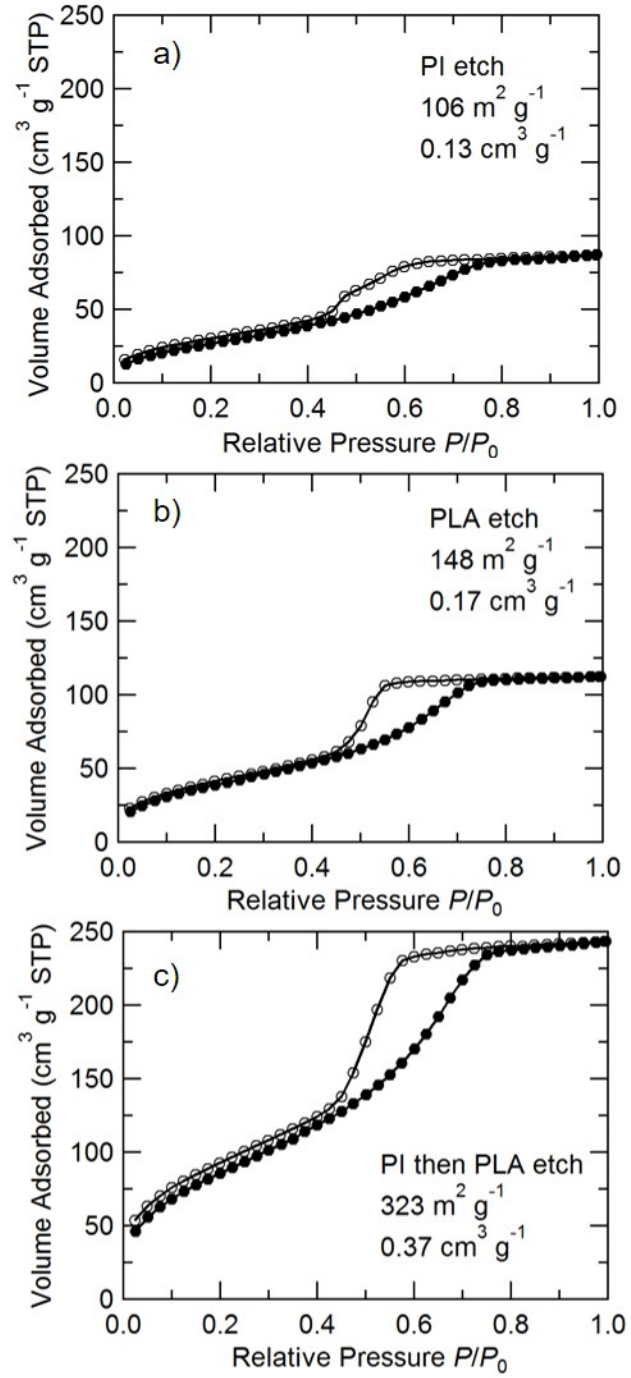

Figure 5.11. Nitrogen sorption isotherms of etched polymers after (a) PI only etching, (b) PLA only etching, (c) and PI then PLA etching. The corresponding BET specific surfaces areas and pore volumes are indicated. Filled circles indicate nitrogen adsorption and empty circles indicate desorption.

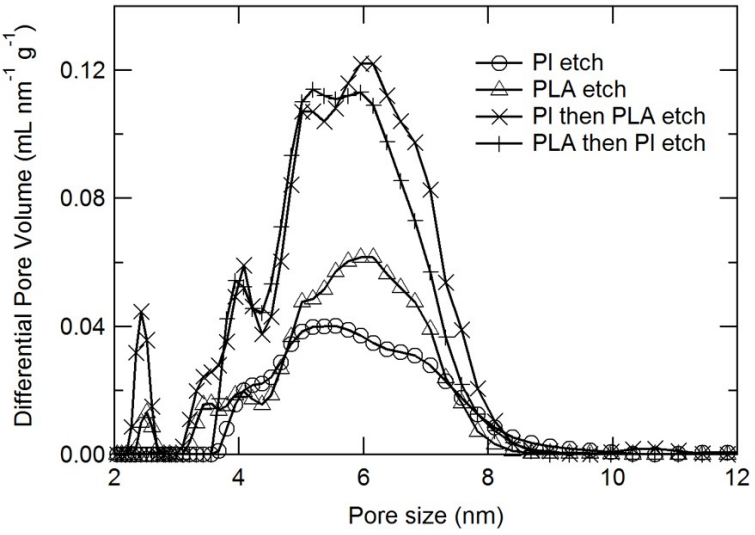

Figure 5.12. Mesopore size distributions after selective etching based on QSDFT analysis applied to the adsorption branch.

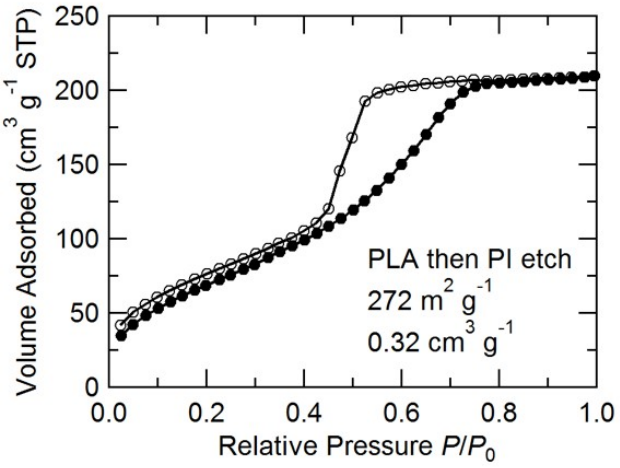

Figure 5.13. Nitrogen sorption isotherm after PLA then PI etching. Filled circles indicate nitrogen adsorption; empty circles indicate desorption. The specific surface area and pore volume is indicated.

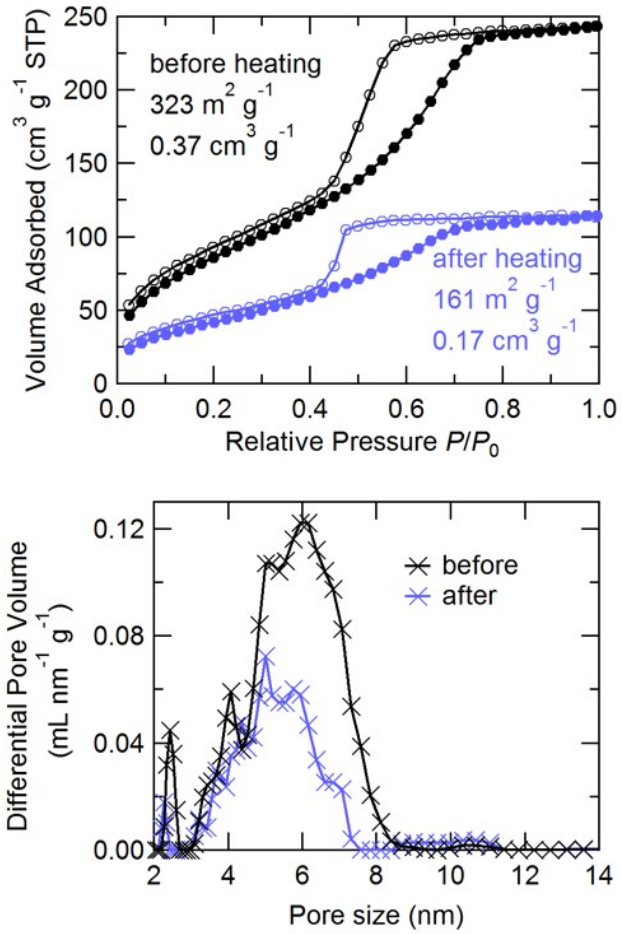

Figure 5.14. (top) Nitrogen sorption isotherm and (bottom) QSDFT mesopore size distribution of a tricontinuous monolith after etching both PI and PLA and then heating at 280 °C for 30 min. Approximately half of the surface area and pore volume is retained, as indicated. Filled circles correspond to the adsorption branch, open circles to the desorption branch of the isotherm.

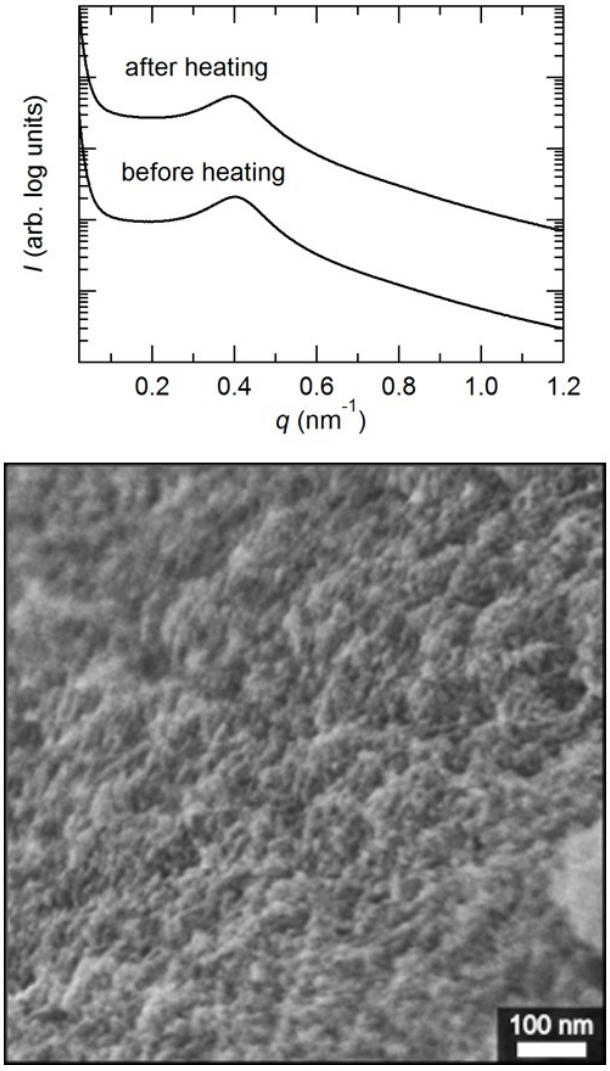

Figure 5.15. (top) SAXS after etching of both PLA and PI, before and after heating to 280 °C. The peak position and intensity is maintained indicating that some of the mesostructured is retained. Traces were arbitrarily shifted vertically for clarity. (bottom) SEM after removing both the PLA and PI domains and then heating in the DSC.

The ability to form a tricontinuous structure is a direct consequence of the high level of incompatibility between PLA and PI which promotes segregation of the PI into relatively pure percolating domains.[14] This was confirmed when we attempted to prepare bicontinuous polymer monoliths of PI-*b*-PDVB, similar to our well-established results

with PLA-*b*-PDVB.[11–13,29] In this case, 70 wt% of the reaction mixture (comprised of 50 wt% PI-CTA dissolved in technical grade DVB) is converted to an insoluble transparent yellow monolith. Although DSC and SAXS analysis suggest that this polymer is microphase-separated (Figures 5.16 and 5.17) with a disordered morphology (Figures 5.18 and 5.19), the PI T_g was still observed after metathesis etching (Figure 5.16) and only 66 wt% of the PI was removed. In terms of the PIMS process, this implies that the kinetic trapping of the PI-*b*-PDVB structure is occurring before well-segregated continuous domains of PI can form, likely because of the relatively small interaction parameter.[14] However, in the presence of PLA-CTA, the PI microphase separates into continuous domains facilitating the preparation of tricontinuous polymers.

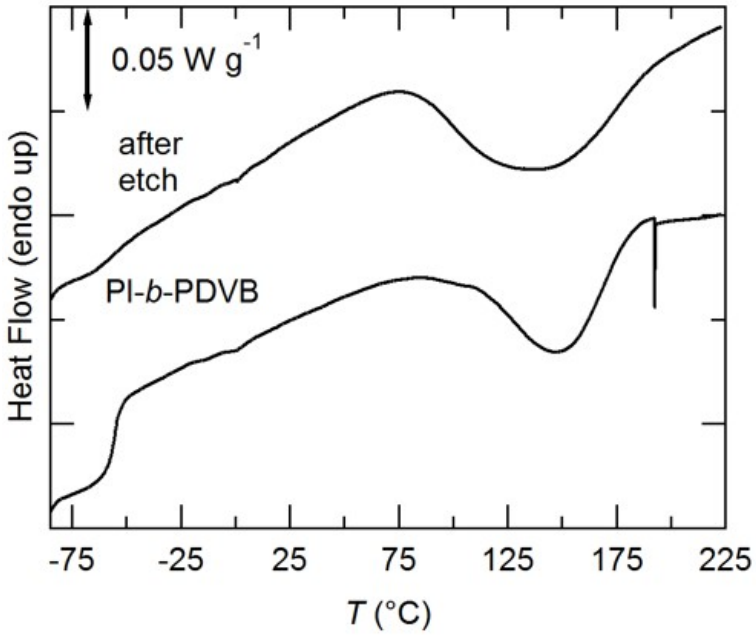

Figure 5.16. DSC thermograms of a PI-*b*-PDVB before and after etching. Traces are the second heating at a ramp rate of 10 °C min^{-1}. The exotherm prior to etching is attributed to PI cross-linking, and additionally to pore collapse after etching.

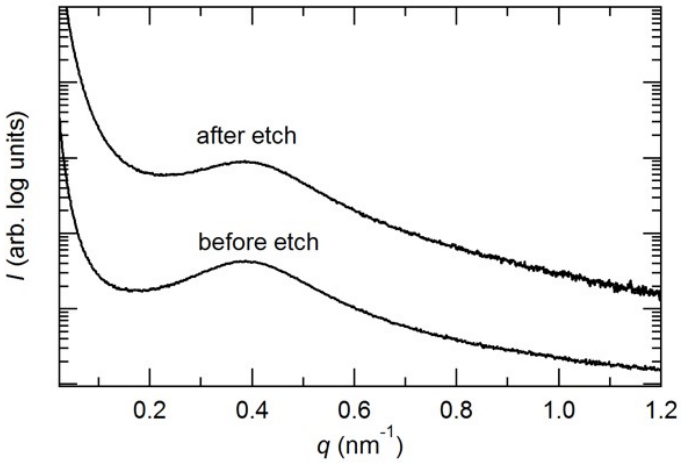

Figure 5.17. SAXS profiles of PI-*b*-PDVB before and after etching, as indicated. The broad maximum at $q^* = 0.39$ nm^{-1} indicates compositional heterogeneities on the 16 nm length scale. Data are arbitrarily shifted vertically for clarity.

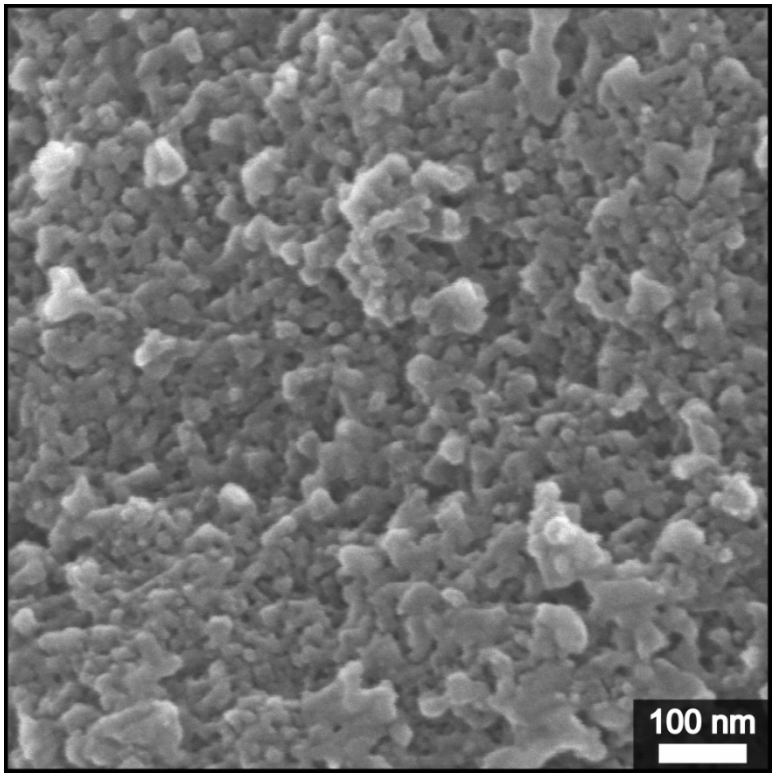

Figure 5.18. SEM micrograph of mesoporous PI-*b*-PDVB after PI etching. The sample was coated in ca. 1 nm of Ir prior to imaging.

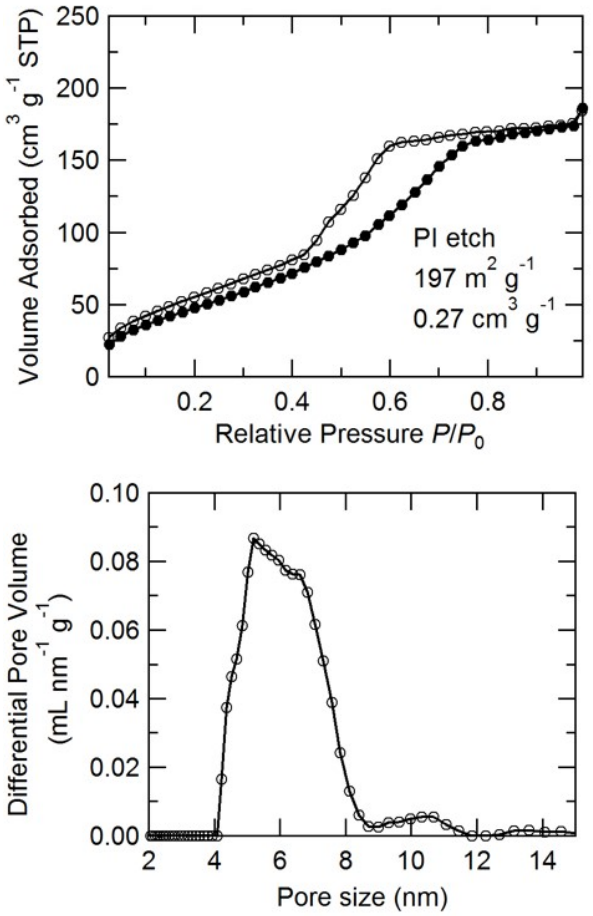

Figure 5.19. (top) Nitrogen sorption isotherm and (bottom) QSDFT pore size distribution after etching PI-*b*-PDVB. In the isotherm filled circles correspond to nitrogen adsorption and empty circles to desorption.

5.4 Conclusions

In summary, we have demonstrated the synthesis of a disordered tricontinuous block polymer representing a unique combination of the disordered structure of polymer blends and the nanometer scale features of ordered self-assembled nanostructures from block polymers. Importantly, orthogonal etching of two of the blocks renders the material mesoporous, which should have two distinct pore wall functionalities, and good control over pore size is attained. DSC and SAXS provide strong evidence of the microphase-

separated structure, and nitrogen sorption measurements show the increase in porosity with orthogonal etching. SEM and TEM provide further confirmation of the disordered network structure.

5.5 References

1) Ravati, S.; Beaulieu, C.; Zolali, A. M.; Favis, B. D. High Performance Materials Based on a Self-Assembled Multiple-Percolated Ternary Blend. *AIChE J.* **2014**, *60*, 3005–3012.

2) Yang, X.; Chen, Y.; Wang, M.; Zhang, H.; Li, X.; Zhang, H. Phase Inversion: A Universal Method to Create High-Performance Porous Electrodes for Nanoparticle-Based Energy Storage Devices. *Adv. Funct. Mater.* **2016**, *26*, 8427–8434.

3) Alward, D. B.; Kinning, D. J.; Thomas, E. L.; Fetters, L. J. Effect of Arm Number and Arm Molecular Weight on the Solid-State Morphology of Poly(styrene-isoprene) Star Block Copolymers. *Macromolecules* **1986**, *19*, 215–224.

4) Bates, F. S.; Fredrickson, G. H. Block Copolymer Thermodynamics: Theory and Experiment. *Annu. Rev. Phys. Chem.* **1990**, *41*, 525–557.

5) Tselikas, Y.; Hadjichristidis, N.; Lescanec, R. L.; Honeker, C. C.; Wohlgemuth, M.; Thomas, E. L. Architecturally-Induced Tricontinuous Cubic Morphology in Compositionally Symmetric Miktoarm Starblock Copolymers. *Macromolecules* **1996**, *29*, 3390–3396.

6) Suzuki, J.; Seki, M.; Matsushita, Y. The Tricontinuous Double-Gyroid Structure from a Three-Component Polymer System. *J. Chem. Phys.* **2000**, *112*, 4862–4868.

7) Cowman, C. D.; Padgett, E.; Tan, K. W.; Hovden, R.; Gu, Y.; Andrejevic, N.; Muller, D.; Coates, G. W.; Wiesner, U. Multicomponent Nanomaterials with Complex Networked Architectures from Orthogonal Degradation and Binary Metal Backfilling in ABC Triblock Terpolymers. *J. Am. Chem. Soc.* **2015**, *137*, 6026–6033.

8) Takenaka, M.; Hashimoto, T.; Dobashi, T. Tricontinuous Structure in a Homopolymer–Homopolymer–Random–Copolymer Ternary Mixture Quenched Under the Tricritical Point. *Phys. Rev. E* **1995**, *52*, 5142–5145.

9) Ravati, S.; Favis, B. D. Tunable Morphologies for Ternary Blends with Poly(butylene succinate): Partial and Complete Wetting Phenomena. *Polymer.* **2013**, *54*, 3271–3281.

10) Shukutani, T.; Myojo, T.; Nakanishi, H.; Norisuye, T.; Tran-Cong-Miyata, Q. Tricontinuous Morphology of Ternary Polymer Blends Driven by Photopolymerization: Reaction and Phase Separation Kinetics. *Macromolecules* **2014**, *47*, 4380–4386.

11) Seo, M.; Hillmyer, M. A. Reticulated Nanoporous Polymers by Controlled Polymerization-Induced Microphase Separation. *Science.* **2012**, *336*, 1422–1425.

12) Schulze, M. W.; Hillmyer, M. A. Tuning Mesoporosity in Cross-Linked Nanostructured Thermosets via Polymerization-Induced Microphase Separation. *Macromolecules* **2017**, *50*, 997–1007.

13) Park, J.; Saba, S. A.; Hillmyer, M. A.; Kang, D.-C.; Seo, M. Effect of Homopolymer in Polymerization-Induced Microphase Separation Process. *Polymer* **2017**, DOI:10.1016/j.polymer.2017.04.046.

14) Lee, S.; Gillard, T. M.; Bates, F. S. Fluctuations, Order, and Disorder in Short Diblock Copolymers. *AIChE J.* **2013**, *59*, 3502–3513.

15) Angelo, R. J.; Ikeda, R. M.; Wallach, M. L. Multiple Glass Transitions of Block Polymers. *Polymer.* **1965**, *6*, 141–156.

16) Bailey, T. S.; Rzayev, J.; Hillmyer, M. A. Routes to Alkene and Epoxide Functionalized Nanoporous Materials from Poly(styrene-*b*-isoprene-*b*-lactide) Triblock Copolymers. *Macromolecules* **2006**, *39*, 8772–8781.

17) Guo, S.; Rzayev, J.; Bailey, T. S.; Zalusky, A. S.; Olayo-Valles, R.; Hillmyer, M. A. Nanopore and Nanobushing Arrays from ABC Triblock Thin Films Containing Two Etchable Blocks. *Chem. Mater.* **2006**, *18*, 1719–1721.

18) Lee, J.-S.; Hirao, A.; Nakahama, S. Polymerization of Monomers Containing Functional Silyl Groups. 5. Synthesis of New Porous Membranes with Functional Groups. *Macromolecules* **1988**, *21*, 274–276.

19) Avgeropoulos, A.; Chan, V. Z.-H.; Lee, V. Y.; Ngo, D.; Miller, R. D.; Hadjichristidis, N.; Thomas, E. L. Synthesis and Morphological Behavior of Silicon-Containing Triblock Copolymers for Nanostructure Applications. *Chem. Mater.* **1998**, *10*, 2109–2115.

20) Chen, S.; Huang, Y.; Tsiang, R. C. Ozonolysis Efficiency of PS-*b*-PI Block Copolymers for Forming Nanoporous Polystyrene. *J. Polym. Sci. Part A Polym. Chem.* **2007**, *46*, 1964–1973.

21) Craig, S. W.; Manzer, J. A.; Coughlin, E. B. Highly Efficient Acyclic Diene Metathesis Depolymerization Using a Ruthenium Catalyst Containing a N-Heterocyclic Carbene Ligand. *Macromolecules* **2001**, *34*, 7929–7931.

22) Sedransk, K. L.; Kaminski, C. F.; Hutchings, L. R.; Moggridge, G. D. The Metathetic Degradation of Polyisoprene and Polybutadiene in Block Copolymers Using Grubbs Second Generation Catalyst. *Polym. Degrad. Stab.* **2011**, *96*, 1074–1080.

23) Chan, V. Z.; Hoffman, J.; Lee, V. Y.; Iatrou, H.; Avgeropoulos, A.; Hadjichristidis, N.; Miller, R. D.; Thomas, E. L. Ordered Bicontinuous Nanoporous and Nanorelief Ceramic Films from Self Assembling Polymer Precursors. *Science* **1999**, *286*, 1716–1719.

24) Ouardad, S.; Peruch, F. Metathetic Degradation of *trans*-1,4-polyisoprene with Ruthenium Catalysts. *Polym. Degrad. Stab.* **2014**, *99*, 249–253.

25) Zalusky, A. S.; Olayo-Valles, R.; Wolf, J. H.; Hillmyer, M. A. Ordered Nanoporous Polymers from Polystyrene-Polylactide Block Copolymers. *J. Am. Chem. Soc.* **2002**, *124*, 12761–12773.

26) Thommes, M.; Kaneko, K.; Neimark, A. V.; Olivier, J. P.; Rodriguez-Reinoso, F.; Rouquerol, J.; Sing, K. S. W. Physisorption of Gases, with Special Reference to the Evaluation of Surface Area and Pore Size Distribution. *Pure Appl. Chem.* **2015**, *87*, 1051–1069.

27) Brunauer, S.; Emmett, P. H.; Teller, E. Adsorption of Gases in Multimolecular Layers. *J. Am. Chem. Soc.* **1938**, *60*, 309–319.

28) Gor, G. Y.; Thommes, M.; Cychosz, K. A.; Neimark, A. V. Quenched Solid Density Functional Theory Method for Characterization of Mesoporous Carbons by Nitrogen Adsorption. *Carbon* **2012**, *50*, 1583–1590.

29) Larsen, M. B.; Horn, J. D. Van; Wu, F.; Hillmyer, M. A. Intrinsically Hierarchical Nanoporous Polymers via Polymerization-Induced Microphase Separation. *Macromolecules* **2017**, *50*, 4363-4371.

30) Sarkar, A.; Stefik, M. Robust Porous Polymers Enabled by a Fast Trifluoroacetic Acid Etch with Improved Selectivity for Polylactide. *Mater. Chem. Front.* **2017** DOI:10.1039/c6qm00266h.

Bibliography

Ahn, H.; Park, S.; Kim, S.; Yoo, P. J.; Ryu, D. Y.; Russell, T. P. Nanoporous Block Copolymer Membranes for Ultrafiltration: A Simple Approach to Size Tunability. *ACS Nano* **2014**, *8*, 11745–11752.

Alward, D. B.; Kinning, D. J.; Thomas, E. L.; Fetters, L. J. Effect of Arm Number and Arm Molecular Weight on the Solid-State Morphology of Poly(styrene-isoprene) Star Block Copolymers. *Macromolecules* **1986**, *19*, 215–224.

Amendt, M. A.; Roerdink, M.; Moench, S.; Phillip, W. A.; Cussler, E. L.; Hillmyer, M. A. Functionalized Nanoporous Membranes from Reactive Triblock Polymers. *Aust. J. Chem.* **2011**, *64*, 1074–1082.

Angelo, R. J.; Ikeda, R. M.; Wallach, M. L. Multiple Glass Transitions of Block Polymers. *Polymer.* **1965**, *6*, 141–156.

Avgeropoulos, A.; Chan, V. Z.-H.; Lee, V. Y.; Ngo, D.; Miller, R. D.; Hadjichristidis, N.; Thomas, E. L. Synthesis and Morphological Behavior of Silicon-Containing Triblock Copolymers for Nanostructure Applications. *Chem. Mater.* **1998**, *10*, 2109–2115.

Bailey, T. S.; Rzayev, J.; Hillmyer, M. A. Routes to Alkene and Epoxide Functionalized Nanoporous Materials from Poly(styrene-*b*-isoprene-*b*-lactide) Triblock Copolymers. *Macromolecules* **2006**, *39*, 8772–8781.

Bandari, R.; Kuballa, J.; Buchmeiser, M. R. Ring-Opening Metathesis Polymerization-Derived, Lectin-Functionalized Monolithic Supports for Affinity Separation of Glycoproteins. *J. Sep. Sci.* **2013**, *36*, 1169–1175.

Bard, A. J.; Faulkner, L. R. *Electrochemical Methods: Fundamentals and Applications*, 2nd ed.; John Wiley and Sons: New York, 2001.

Barlow, K. J.; Bernabeu, V.; Hao, X.; Hughes, T. C.; Hutt, O. E.; Polyzos, A.; Turner, K. A.; Moad, G. Triphenylphosphine-Grafted, RAFT-Synthesised, Porous Monoliths as Catalysts for Michael Addition in Flow Synthesis. *React. Funct. Polym.* **2015**, *96*, 89–96.

Barlow, K. J.; Hao, X.; Hughes, T. C.; Hutt, O. E.; Polyzos, A.; Turner, K. A.; Moad, G. Porous, Functional, Poly(styrene-*co*-divinylbenzene) Monoliths by RAFT Polymerization. *Polym. Chem.* **2014**, *5*, 722–732.

Barrett, E. P.; Joyner, Leslie, G.; Halenda, Paul, P. The Determination of Pore Volume and Area Distributions in Porous Substances. I. Computations from Nitrogen Isotherms. *J. Am. Chem. Soc.* **1951**, *73*, 373–380.

Bates, F. S.; Fredrickson, G. H. Block Copolymer Thermodynamics: Theory and Experiment. *Annu. Rev. Phys. Chem.* **1990**, *41*, 525–557.

Bates, F. S.; Wiltzius, P. Spinodal Decomposition of a Symmetric Critical Mixture of Deuterated and Protonated Polymer. *J. Chem. Phys.* **1989**, *91*, 3258–3274.

Bayer, E. Towards the Chemical Synthesis of Proteins. *Angew. Chemie* **1991**, *30*, 113–129.

Bertrand, A.; Hillmyer, M. A. Nanoporous Poly(lactide) by Olefin Metathesis Degradation. *J. Am. Chem. Soc.* **2013**, *135*, 10918–10921.

Bolton, J.; Bailey, T. S.; Rzayev, J. Large Pore Size Nanoporous Materials from the Self-Assembly of Asymmetric Bottlebrush Block Copolymers. *Nano Lett.* **2011**, *11*, 998–1001.

Brett, C. M. A.; Brett, A. M. O. *Electrochemistry Principles, Methods, and Applications*; Oxford University Press: New York, NY, **1993**.

Bronstein, L. M.; Goerigk, G.; Kostylev, M.; Pink, M.; Khotina, I. A.; Valetsky, P. M.; Matveeva, V. G.; Sulman, E. M.; Sulman, M. G.; Bykov, A. V.; Lakina, N.V; Spontak, R.J. Structure and Catalytic Properties of Pt-Modified Hyper-Cross-Linked Polystyrene Exhibiting Hierarchical Porosity. *J. Phys. Chem. B* **2004**, *108*, 18234–18242.

Brown, J. F.; Krajnc, P.; Cameron, N. R. PolyHIPE Supports in Batch and Flow-Through Suzuki Cross-Coupling Reactions. *Ind. Eng. Chem. Res.* **2005**, *44*, 8565–8572.

Brunauer, S.; Emmett, P. H.; Teller, E. Adsorption of Gases in Multimolecular Layers. *J. Am. Chem. Soc.* **1938**, *60*, 309–319.

Cavicchi, K. A.; Zalusky, A. S.; Hillmyer, M. A.; Lodge, T. P. An Ordered Nanoporous Monolith from an Elastomeric Crosslinked Block Copolymer Precursor. *Macromol. Rapid Commun.* **2004**, *25*, 704–709.

Chan, V. Z.; Hoffman, J.; Lee, V. Y.; Iatrou, H.; Avgeropoulos, A.; Hadjichristidis, N.; Miller, R. D.; Thomas, E. L. Ordered Bicontinuous Nanoporous and Nanorelief Ceramic Films from Self Assembling Polymer Precursors. *Science.* **1999**, *286*, 1716–1719.

Chan, P. K.; Rey, A. D. Polymerization-Induced Phase Separation. 1. Droplet Size Selection Mechanism. *Macromolecules* **1996**, *29*, 8934–8941.

Chan, P. K.; Rey, A. D. Polymerization-Induced Phase Separation. 2. Morphological Analysis. **1997**, *30*, 2135–2143.

Chen, L.; Hillmyer, M. A. Mechanically and Thermally Robust Ordered Nanoporous Monoliths Using Norbornene-Functional Block Polymers. *Macromolecules* **2009**, *42*, 4237–4243.

Chen, L.; Phillip, W. A.; Cussler, E. L.; Hillmyer, M. A. Robust Nanoporous Membranes Templated by a Doubly Reactive Block Copolymer. *J. Am. Chem. Soc.* **2007**, *129*, 13786–13787.

Chen, S.; Huang, Y.; Tsiang, R. C. Ozonolysis Efficiency of PS-*b*-PI Block Copolymers for Forming Nanoporous Polystyrene. *J. Polym. Sci. Part A Polym. Chem.* **2007**, *46*, 1964–1973.

Chen, X. C.; Kortright, J. B.; Balsara, N. P. Water Uptake and Proton Conductivity in Porous Block Copolymer Electrolyte Membranes. *Macromolecules* **2015**, *48*, 5648–5655.

Chopade, S. A.; Au, J. G.; Li, Z.; Schmidt, P. W.; Hillmyer, M. A.; Lodge, T. P. Robust Polymer Electrolyte Membranes with High Ambient-Temperature Lithium-Ion Conductivity via Polymerization-Induced Microphase Separation. *ACS Appl. Mater. Interfaces* **2017**, *9*, 14561–14565.

Chopade, S. A.; So, S.; Hillmyer, M. A.; Lodge, T. P. Anhydrous Proton Conducting Polymer Electrolyte Membranes via Polymerization-Induced Microphase Separation. *ACS Appl. Mater. Interfaces* **2016**, *8*, 6200–6210.

Craig, S. W.; Manzer, J. A.; Coughlin, E. B. Highly Efficient Acyclic Diene Metathesis Depolymerization Using a Ruthenium Catalyst Containing a N-Heterocyclic Carbene Ligand. *Macromolecules* **2001**, *34*, 7929–7931.

CoralPor Porous Glass Product Information. http://www.us.schott.com/SCHOTT. Accessed on May 8, 2015.

Cowman, C. D.; Padgett, E.; Tan, K. W.; Hovden, R.; Gu, Y.; Andrejevic, N.; Muller, D.; Coates, G. W.; Wiesner, U. Multicomponent Nanomaterials with Complex Networked Architectures from Orthogonal Degradation and Binary Metal Backfilling in ABC Triblock Terpolymers. *J. Am. Chem. Soc.* **2015**, *137*, 6026–6033.

Debye, P.; Hückel. On the Theory of Electrolytes I. Freezing Point Depression and Related Phenomena. *Phys. Z.* **1923**, *24*, 185-206.

Dohner, R. E.; Wegmann, D.; Morf, W. E.; Simon, W. Reference Electrode with Free-Flowing Free-Diffusion Liquid Junction. *Anal. Chem.* **1986**, *58*, 2585–2589.

Eder, K.; Huber, C. G.; Buchmeiser, M. R. Surface-Functionalized, Ring-Opening Metathesis Polymerization-Derived Monoliths for Anion-Exchange Chromatography. *Macromol. Rapid Commun.* **2007**, *28*, 2029–2032.

Fierke, M. A. The Utilization of Templated Porous Electrodes in Electrochemical Applications, University of Minnesota, **2013**.

Germack, D. S.; Wooley, K. L. Isoprene Polymerization via Reversible Addition Fragmentation Chain Transfer Polymerization. *J. Polym. Sci. Part A-Polymer Chem.* **2007**, *45*, 4100–4108.

Germack, D. S.; Wooley, K. L. RAFT-Based Synthesis and Characterization of ABC versus ACB Triblock Copolymers Containing *tert*-Butyl Acrylate, Isoprene, and Styrene Blocks. *Macromol. Chem. Phys.* **2007**, *208*, 2481–2491.

Gömann, A.; Deverell, J. A.; Munting, K. F.; Jones, R. C.; Rodemann, T.; Canty, A. J.; Smith, J. A.; Guijt, R. M. Palladium-Mediated Organic Synthesis Using Porous Polymer Monolith Formed in Situ as a Continuous Catalyst Support Structure for Application in Microfluidic Devices. *Tetrahedron* **2009**, *65*, 1450–1454.

Gor, G. Y.; Thommes, M.; Cychosz, K. A.; Neimark, A. V. Quenched Solid Density Functional Theory Method for Characterization of Mesoporous Carbons by Nitrogen Adsorption. *Carbon* **2012**, *50*, 1583–1590.

Gruber, M. F.; Schulte, L.; Ndoni, S. Nanoporous Materials Modified with Biodegradable Polymers as Models for Drug Delivery Applications. *J. Colloid Interface Sci.* **2013**, *395*, 58–63.

Gu, Y.; Wiesner, U. Tailoring Pore Size of Graded Mesoporous Block Copolymer Membranes: Moving from Ultrafiltration toward Nanofiltration. *Macromolecules* **2015**, *48*, 6153–6159.

Guo, S.; Rzayev, J.; Bailey, T. S.; Zalusky, A. S.; Olayo-Valles, R.; Hillmyer, M. A. Nanopore and Nanobushing Arrays from ABC Triblock Thin Films Containing Two Etchable Blocks. *Chem. Mater.* **2006**, *18*, 1719–1721.

Hamley, I.W. The Physics of Block Copolymers, Oxford University Press Inc., New York, **1998**, pp. 331-412.

Hanley, K. J.; Lodge, T. P.; Huang, C.-I. Phase Behavior of a Block Copolymer in Solvents of Varying Selectivity. *Macromolecules* **2000**, *33*, 5918–5931.

Hasegawa, J.; Kanamori, K.; Nakanishi, K.; Hanada, T.; Yamago, S. Pore Formation in Poly(divinylbenzene) Networks Derived from Organotellurium-Mediated Living Radical Polymerization. *Macromolecules* **2009**, *42*, 1270–1277.

Hawker, C. J. “Living” Free Radical Polymerization: A Unique Technique for the Preparation of Controlled Macromolecular Architectures. *Acc. Chem. Res.* **1997**, *4842*, 373–382.

He, D.; Ulbricht, M. Tailored “Grafting-From” Functionalization of Microfiltration Membrane Surface Photo-Initiated by Immobilized Iniferter. *Macromol. Chem. Phys.* **2009**, *210*, 1149–1158.

He, L.; Zhang, Y.; Zeng, C.; Ngiam, M.; Liao, S.; Quan, D.; Zeng, Y.; Lu, J.; Ramakrishna, S. Manufacture of PLGA Multiple-Channel Conduits with Precise Hierarchical Pore Architectures and In Vitro/Vivo Evaluation for Spinal Cord Injury. *Tissue Eng. Part C- Methods* **2009**, *15*, 243–255.

Hess, S. C.; Kohll, A. X.; Raso, R. A.; Schumacher, C. M.; Grass, R. N.; Stark, W. J. Template-Particle Stabilized Bicontinuous Emulsion Yielding Controlled Assembly of Hierarchical High-Flux Filtration Membranes. *ACS Appl. Mater. Interfaces* **2015**, *7*, 611–617.

Hillmyer, M. A. Nanoporous Materials from Block Copolymer Precursors. *Adv. Polym. Sci.* **2005**, *190*, 137–181.

Hjertén, S.; Liao, J.-L.; Zhang, R. High-Performance Liquid Chromatography on Continuous Polymer Beds. *J. Chromatogr.* **1989**, *473*, 273–275.

Jones, B. H.; Lodge, T. P. Hierarchically Structured Materials from Block Polymer Confinement within Bicontinuous Microemulsion-Derived Nanoporous Polyethylene. *ACS Nano* **2011**, *5*, 8914–8927.

Kanamori, K.; Hasegawa, J.; Nakanishi, K.; Hanada, T. Facile Synthesis of Macroporous Cross-Linked Methacrylate Gels by Atom Transfer Radical Polymerization. *Macromolecules* **2008**, *41*, 7186–7193.

Kato, T.; Hillmyer, M. A. Functionalized Nanoporous Polyethylene Derived from Miscible Block Polymer Blends. *ACS Appl. Mater. Interfaces* **2013**, *5*, 291–300.

Kim, S.; Yoo, M.; Kang, N.; Moon, B.; Kim, B. J.; Choi, S.; Kim, J. U.; Bang, J. Nanoporous Bicontinuous Structures via Addition of Thermally-Stable Amphiphilic Nanoparticles within Block Copolymer Templates. *ACS Appl. Mater. Interfaces* **2013**, *5*, 5659–5666.

Jackson, E. A.; Lee, Y.; Hillmyer, M. A. ABAC Tetrablock Terpolymers for Tough Nanoporous Filtration Membranes. *Macromolecules* **2013**, *46*, 1484–1491.

Jalal, T.; Bettahalli, N. M. S.; Le, N. L.; Nunes, S. P. Hydrophobic Hyflon AD/PVDF Membranes for Butanol Dehydration via Pervaporation. *Ind. Eng. Chem. Res.* **2015**, *54*, 11180–11187.

Jones, B. H.; Lodge, T. P. Nanocasting Nanoporous Inorganic and Organic Materials from Polymeric Bicontinuous Microemulsion Templates. *Polym. J.* **2012**, *44*, 131–146.

Kanamori, K.; Hasegawa, J.; Nakanishi, K.; Hanada, T. Facile Synthesis of Macroporous Cross-Linked Methacrylate Gels by Atom Transfer Radical Polymerization. *Macromolecules* **2008**, *41*, 7186–7193.

Kanamori, K.; Nakanishi, K.; Hanada, T. Rigid Macroporous Poly(divinylbenzene) Monoliths with a Well-Defined Bicontinuous Morphology Prepared by Living Radical Polymerization. *Adv. Mater.* **2006**, *18*, 2407–2411.

Lai, J. T.; Filla, D.; Shea, R. Functional Polymers from Novel Carboxyl-Terminated Trithiocarbonates as Highly Efficient RAFT Agents. *Macromolecules* **2002**, *35*, 6754–6756.

Lai, C.; Russel, W. B.; Register, R. A. Scaling of Domain Spacing in Concentrated Solutions of Block Copolymers in Selective Solvents. *Macromolecules* **2002**, *35*, 4044–4049.

Laher, M.; Causon, T. J.; Buchberger, W.; Hild, S.; Nischang, I. Assessing the Nanoscale Structure and Mechanical Properties of Polymer Monoliths Used for Chromatography. *Anal. Chem.* **2013**, *85*, 5645–5649.

Larsen, M. B.; Horn, J. D. Van; Wu, F.; Hillmyer, M. A. Intrinsically Hierarchical Nanoporous Polymers via Polymerization-Induced Microphase Separation. *Macromolecules* **2017**, *50*, 4363-4371.

Lee, J.-S.; Hirao, A.; Nakahama, S. Polymerization of Monomers Containing Functional Silyl Groups. 5. Synthesis of New Porous Membranes with Functional Groups. *Macromolecules* **1988**, *21*, 274–276.

Lee, S.; Gillard, T. M.; Bates, F. S. Fluctuations, Order, and Disorder in Short Diblock Copolymers. *AIChE J.* **2013**, *59*, 3502–3513.

Li, L.; Schulte, L.; Clausen, L. D.; Hansen, K. M.; Jonsson, G. E.; Ndoni, S. Gyroid Nanoporous Membranes with Tunable Permeability. *ACS Nano* **2011**, *5*, 7754–7766.

Li, Y.; Tolley, H. D.; Lee, M. L. Size-Exclusion Separation of Proteins Using a Biocompatible Polymeric Monolithic Capillary Column with Mesoporosity. *J. Chromatogr. A* **2010**, *1217*, 8181–8185.

Li, X.; Zhou, M.; Turson, M.; Lin, S.; Jiang, P.; Dong, X. Preparation of Clenbuterol Imprinted Monolithic Polymer with Hydrophilic Outer Layers by Reversible Addition-Fragmentation Chain Transfer Polymerization and Its Application in the Clenbuterol Determination from Human Serum by On-Line Solid-Phase Extractio. *Analyst* **2013**, *138*, 3066–3074.

Liang, C.; Dai, S. Dual Phase Separation for Synthesis of Bimodal Meso-/Macroporous. *Chem. Mater.* **2009**, *21*, 2115–2124.

Liu, K.; Aggarwal, P.; Tolley, H. D.; Lawson, J. S.; Lee, M. L. Fabrication of Highly Cross-Linked Reversed-Phase Monolithic Columns via Living Radical Polymerization. *J. Chromatogr. A* **2014**, *1367*, 90–98.

Lohmeijer, B. G. G.; Pratt, R. C.; Leibfarth, F.; Logan, J. W.; Long, D. A.; Dove, A. P.; Nederberg, F.; Choi, J.; Wade, C.; Waymouth, R. M.; Hedrick, J.L. Guanidine and Amidine Organocatalysts for Ring-Opening Polymerization of Cyclic Esters. *Macromolecules* **2006**, *39*, 8574–8583.

Lowell, S.; Shields, J. E.; Thomas, M. A.; Thommes, M. Characterization of Porous Solids and Powders: Surface Area, Pore Size and Density; Scarlett, B., Ed.; Kluwer Academic Publishers: Norwell, MA, **2004**; pp. 13, 44.

Lubbad, S. H.; Buchmeiser, M. R. Highly Cross-Linked Polymeric Capillary Monoliths for the Separation of Low, Medium, and High Molecular Weight Analytes. *J. Sep. Sci.* **2009**, *32*, 2521–2529.

Mao, H.; Arrechea, P. L.; Bailey, T. S.; Johnson, B. J. S.; Hillmyer, M. A. Control of Pore Hydrophilicity in Ordered Nanoporous Polystyrene Using an AB/AC Block Copolymer Blending Strategy. *Faraday Discuss.* **2005**, *128*, 149–162.

Mao, H.; Hillmyer, M. A. Nanoporous Polystyrene by Chemical Etching of Poly(ethylene oxide) from Ordered Block Copolymers. *Macromolecules* **2005**, *38*, 4038–4039.

Mao, H.; Hillmyer, M. A. Macroscopic Samples of Polystyrene with Ordered Three-Dimensional Nanochannels. *Soft Matter* **2006**, *2*, 57–59.

Mao, H.; Hillmyer, M. A. Morphological Behavior of Polystyrene-*block*-Polylactide/Polystyrene-*block*-Poly(ethylene oxide) Blends. *Macromol. Chem. Phys.* **2008**, *209*, 1647–1656.

Maya, F.; Svec, F. A New Approach to the Preparation of Large Surface Area Poly(styrene-*co*-divinylbenzene) Monoliths via Knitting of Loose Chains Using External

Crosslinkers and Application of These Monolithic Columns for Separation of Small Molecules. *Polymer.* **2014**, *55*, 340–346.

McIntosh, L. D.; Schulze, M. W.; Irwin, M. T.; Hillmyer, M. A.; Lodge, T. P. Evolution of Morphology, Modulus, and Conductivity in Polymer Electrolytes Prepared via Polymerization-Induced Phase Separation. *Macromolecules* **2015**, *48*, 1418–1428.

Meyer, U.; Svec, F.; Fréchet, J. M. J.; Hawker, C. J.; Irgum, K. Use of Stable Free Radicals for the Sequential Preparation and Surface Grafting of Functionalized Macroporous Monoliths. *Macromolecules* **2000**, *33*, 7769–7775.

Minakuchi, H.; Nakanishi, K.; Soga, N.; Ishizuka, N.; Tanaka, N. Octadecylsilylated Porous Silica Rods as Separation Media for Reversed-Phase Liquid Chromatography. *Anal. Chem.* **1996**, *68*, 3498–3501.

Moravcová, D.; Jandera, P.; Planeta, J.; Urban, J.; Planeta, J. Characterization of Polymer Monolithic Stationary Phases for Capillary HPLC. *J. Sep. Sci.* **2003**, *26*, 1005–1016.

Morkved, T. L.; Stepanek, P.; Krishnan, K.; Bates, F. S.; Lodge, T. P. Static and Dynamic Scattering from Ternary Polymer Blends: Bicontinuous Microemulsions, Lifshitz Lines, and Amphiphilicity. *J. Chem. Phys.* **2001**, *114*, 7247–7259.

Morris, R. E.; Wheatley, P. S. Gas Storage in Nanoporous Materials. *Angew. Chemie - Int. Ed.* **2008**, *47*, 4966–4981.

Mousavi, M. P. S.; Bühlmann, P. Reference Electrodes with Salt Bridges Contained in Nanoporous Glass: An Underappreciated Source of Error. *Anal. Chem.* **2013**, *85*, 8895–8901.

Mousavi, M. P. S.; Saba, S. A.; Anderson, E. L.; Hillmyer, M. A.; Bühlmann, P. Avoiding Errors in Electrochemical Measurements: Effect of Frit Material on the Performance of Reference Electrodes with Porous Frit Junctions. *Anal. Chem.* **2016**, *88*, 8706–8713.

Meuler, A. J.; Hillmyer, M. A.; Bates, F. S. Ordered Network Mesostructures in Block Polymer Materials. *Macromolecules* **2009**, *42*, 7221–7250.

Mulvenna, R. A.; Weidman, J. L.; Jing, B.; Pople, J. A.; Zhu, Y.; Boudouris, B. W.; Phillip, W. A. Tunable Nanoporous Membranes with Chemically-Tailored Pore Walls from Triblock Polymer Templates. *J. Memb. Sci.* **2014**, *470*, 246–256.

Nasiri, M.; Bertrand, A.; Reineke, T. M.; Hillmyer, M. A. Polymeric Nanocylinders by Combining Block Copolymer Self-Assembly and Nanoskiving. *ACS Appl. Mater. Interfaces* **2014**, *6*, 16283–16288.

Ndoni, S.; Vigild, M. E.; Berg, R. H. Nanoporous Materials with Spherical and Gyroid Cavities Created by Quantitative Etching of Polydimethylsiloxane in Polystyrene–Polydimethylsiloxane Block Copolymers. *J. Am. Chem. Soc.* **2003**, *125*, 13366–13367.

Nischang, I.; Brüggemann, O. On the Separation of Small Molecules by Means of Nano-Liquid Chromatography with Methacrylate-Based Macroporous Polymer Monoliths. *J. Chromatogr. A* **2010**, *1217*, 5389–5397.

Nischang, I.; Teasdale, I.; Brüggemann, O. Porous Polymer Monoliths for Small Molecule Separations: Advancements and Limitations. *Anal. Bioanal. Chem.* **2011**, *400*, 2289–2304.

Norisuye, T.; Morinaga, T.; Tran-cong-miyata, Q.; Goto, A.; Fukuda, T.; Shibayama, M. Comparison of the Gelation Dynamics for Polystyrenes Prepared by Conventional and Living Radical Polymerizations: A Time-Resolved Dynamic Light Scattering Study. *Polymer* **2005**, *46*, 1982–1994.

Oh, J.; Seo, M. Photoinitiated Polymerization-Induced Microphase Separation for the Preparation of Nanoporous Polymer Films. *ACS Macro Lett.* **2015**, *4*, 1244–1248.

Olson, D. A.; Chen, L.; Hillmyer, M. A. Templating Nanoporous Polymers with Ordered Block Copolymers. *Chem. Mater.* **2008**, *20*, 869–890.

Ottens, M.; Leene, G.; Beenackers, A. A. C. M.; Cameron, N.; Sherrington, D. C. PolyHipe: A New Polymeric Support for Heterogeneous Catalytic Reactions: Kinetics of Hydration of Cyclohexene in Two- and Three-Phase Systems over a Strongly Acidic Sulfonated PolyHipe. *Ind. Eng. Chem. Res.* **2000**, *39*, 259–266.

Ouardad, S.; Peruch, F. Metathetic Degradation of *trans*-1,4-polyisoprene with Ruthenium Catalysts. *Polym. Degrad. Stab.* **2014**, *99*, 249–253.

Park, J.; Saba, S. A.; Hillmyer, M. A.; Kang, D.-C.; Seo, M. Effect of Homopolymer in Polymerization-Induced Microphase Separation Process. *Polymer* **2017**, DOI:10.1016/j.polymer.2017.04.046.

Peters, E. C.; Svec, F.; Fréchet, J. M. J. Preparation of Large-Diameter "Molded" Porous Polymer Monoliths and the Control of Pore Structure Homogeneity. *Chem. Mater.* **1997**, *9*, 1898–1902.

Peters, E. C.; Svec, F.; Fréchet, J. M. J.; Viklund, C.; Irgum, K. Control of Porous Properties and Surface Chemistry in "Molded" Porous Polymer Monoliths Prepared by Polymerization in the Presence of TEMPO. *Macromolecules* **1999**, *32*, 6377–6379.

Peterson, D. S.; Rohr, T.; Svec, F.; Fréchet, J. M. J. Enzymatic Microreactor-on-a-Chip: Protein Mapping Using Trypsin Immobilized on Porous Polymer Monoliths Molded in Channels of Microfluidic Devices. *Anal. Chem.* **2002**, *74*, 4081–4088.

Peterson, D. S.; Rohr, T.; Svec, F.; Fréchet, J. M. J. Dual-Function Microanalytical Device by In Situ Photolithographic Grafting of Porous Polymer Monolith: Integrating Solid-Phase Extraction and Enzymatic Digestion for Peptide Mass Mapping. *Anal. Chem.* **2003**, *75*, 5328–5335.

Petro, M.; Svec, F.; Fréchet, J. M. J. Immobilization of Trypsin onto "Molded" Macroporous Poly(glycidyl methacrylate-*co*-ethylene dimethacrylate) Rods and Use of the Conjugates as Bioreactors and for Affinity Chromatography. *Biotechnol. Bioeng.* **1996**, *49*, 355–363.

Phillip, W. A.; Dorin, R. M.; Werner, J.; Hoek, E. M. V; Wiesner, U.; Elimelech, M. Tuning Structure and Properties of Graded Triblock Terpolymer-Based Mesoporous and Hybrid Films. *Nano Lett.* **2011**, *11*, 2892–2900.

Phillip, W. A.; O'Neill, B.; Rodwogin, M.; Hillmyer, M. A.; Cussler, E. L. Self-Assembled Block Copolymer Thin Films as Water Filtration Membranes. *ACS Appl. Mater. Interfaces* **2010**, *2*, 847–853.

Pitet, L. M.; Amendt, M. A.; Hillmyer, M. A. Nanoporous Linear Polyethylene from a Block Polymer Precursor. *J. Am. Chem. Soc.* **2010**, *132*, 8230–8231.

Radjabian, M.; Abetz, V. Tailored Pore Sizes in Integral Asymmetric Membranes Formed by Blends of Block Copolymers. *Adv. Mater.* **2015**, *27*, 352–355.

Ravati, S.; Beaulieu, C.; Zolali, A. M.; Favis, B. D. High Performance Materials Based on a Self-Assembled Multiple-Percolated Ternary Blend. *AIChE J.* **2014**, *60*, 3005–3012.

Ravati, S.; Favis, B. D. Tunable Morphologies for Ternary Blends with Poly(butylene succinate): Partial and Complete Wetting Phenomena. *Polymer.* **2013**, *54*, 3271–3281.

Roe, R.J.; Nojima, S. Small-Angle X-Ray Scattering Study of Micro- and Macro-Phase Separations in Blends of Block Copolymer with Homopolymer. *Mater. Res. Soc. Symp. Proc.* **1987**, *79*, 151–158.

Rzayev, J.; Hillmyer, M. A. Nanoporous Polystyrene Containing Hydrophilic Pores from an ABC Triblock Copolymer Precursor. *Macromolecules* **2005**, *38*, 3–5.

Rzayev, J.; Hillmyer, M. A. Nanochannel Array Plastics with Tailored Surface Chemistry. *J. Am. Chem. Soc.* **2005**, *127*, 13373–13379.

Saba, S. A.; Mousavi, M. P. S.; Bühlmann, P.; Hillmyer, M. A. Hierarchically Porous Polymer Monoliths by Combining Controlled Macro- and Microphase Separation. *J. Am. Chem. Soc.* **2015**, *137*, 8896–8899.

Saban, M. D.; Georges, M. K.; Veregin, R. P. N.; Hamer, G. K. H.; Kazmaier, P. M. Nitroxide-Mediated Free Radical Polymerization of Styrene. Absence of the Gel Effect. *Macromolecules* **1995**, *28*, 7032–7034.

Sai, H.; Tan, K. W.; Hur, K.; Asenath-Smith, E.; Hovden, R.; Jiang, Y.; Riccio, M.; Muller, D. A.; Elser, V.; Estroff, L. A.; Gruner, S. M.; Wiesner, U. Hierarchical Porous Polymer Scaffolds from Block Copolymers. *Science* **2013**, *341*, 530–534.

Santora, B. P.; Gagne, M. R.; Moloy, K. G.; Radu, N. S. Porogen and Cross-Linking Effects on the Surface Area, Pore Volume Distribution, and Morphology of Macroporous Polymers Obtained by Bulk Polymerization. *Macromolecules* **2001**, *34*, 658–661.

Sarkar, A.; Stefik, M. Robust Porous Polymers Enabled by a Fast Trifluoroacetic Acid Etch with Improved Selectivity for Polylactide. *Mater. Chem. Front.* **2017** DOI:10.1039/c6qm00266h.

Schulte, L.; Grydgaard, A.; Jakobsen, M. R.; Szewczykowski, P. P.; Guo, F.; Vigild, M. E.; Berg, R. H.; Ndoni, S. Nanoporous Materials from Stable and Metastable Structures of 1,2-PB-*b*-PDMS Block Copolymers. *Polymer* **2011**, *52*, 422–429.

Schulze, M. W.; Hillmyer, M. A. Tuning Mesoporosity in Cross-Linked Nanostructured Thermosets via Polymerization-Induced Microphase Separation. *Macromolecules* **2017**, *50*, 997–1007.

Schulze, M. W.; McIntosh, L. D.; Hillmyer, M. A.; Lodge, T. P. High-Modulus, High-Conductivity Nanostructured Polymer Electrolyte Membranes via Polymerization-Induced Phase Separation. *Nano Lett.* **2014**, *14*, 122–126.

Schumers, J.-M.; Vlad, A.; Huynen, I.; Gohy, J.-F.; Fustin, C.-A. Functionalized Nanoporous Thin Films from Photocleavable Block Copolymers. *Macromol. Rapid Commun.* **2012**, *33*, 199–205.

Sedransk, K. L.; Kaminski, C. F.; Hutchings, L. R.; Moggridge, G. D. The Metathetic Degradation of Polyisoprene and Polybutadiene in Block Copolymers Using Grubbs Second Generation Catalyst. *Polym. Degrad. Stab.* **2011**, *96*, 1074–1080.

Seo, M. *Submicron Porous Materials*; Bettotti, P., Ed.; Springer: Cham, Switzerland, **2017**; pp 59, 61, 62.

Seo, M.; Hillmyer, M. A. Reticulated Nanoporous Polymers by Controlled Polymerization-Induced Microphase Separation. *Science.* **2012**, *336*, 1422–1425.

Seo, M.; Kim, S.; Oh, J.; Kim, S.-J.; Hillmyer, M. A. Hierarchically Porous Polymers from Hyper-Cross-Linked Block Polymer Precursors. *J. Am. Chem. Soc.* **2015**, *137*, 600–603.

Seo, M.; Murphy, C. J.; Hillmyer, M. A. One-Step Synthesis of Cross-Linked Block Polymer Precursor to a Nanoporous Thermoset. *ACS Macro Lett.* **2013**, *2*, 617–620.

Sherrington, D. C. Preparation, Structure and Morphology of Polymer Supports. *Chem. Commun.* **1998**, *21*, 2275–2286.

Shinkai, T.; Sugiyama, K.; Ito, K.; Yokoyama, H. Nanoporous Fabrication of Block Copolymers via Carbon Dioxide Swelling: Difference between CO_2-Swollen and Nanoporous Block Copolymers. *Polymer.* **2016**, *100*, 19–27.

Shintani, Y.; Zhou, X.; Furuno, M.; Minakuchi, H.; Nakanishi, K. Monolithic Silica Column for In-Tube Solid-Phase Microextraction Coupled to High-Performance Liquid Chromatography. *J. Chromatogr. A* **2003**, *985*, 351–357.

Shukutani, T.; Myojo, T.; Nakanishi, H.; Norisuye, T.; Tran-Cong-Miyata, Q. Tricontinuous Morphology of Ternary Polymer Blends Driven by Photopolymerization: Reaction and Phase Separation Kinetics. *Macromolecules* **2014**, *47*, 4380–4386.

Sinner, F.; Buchmeiser, M. R. A New Class of Continuous Polymer Supports Prepared by Ring-Opening Metathesis Polymerization: A Straightforward Route to Functionalized Monoliths. *Macromolecules* **2000**, *33*, 5777–5786.

Smått, J.-H.; Weidenthaler, C.; Rosenholm, J. B.; Linde, M. Hierarchically Porous Metal Oxide Monoliths Prepared by the Nanocasting Route. *Chem. Mater.* **2006**, *18*, 1443–1450.

Suzuki, J.; Seki, M.; Matsushita, Y. The Tricontinuous Double-Gyroid Structure from a Three-Component Polymer System. *J. Chem. Phys.* **2000**, *112*, 4862–4868.

Svec, F. Recent Developments in the Field of Monolithic Stationary Phases for Capillary Electrochromatography. *J. Sep. Sci.* **2005**, *28*, 729–745.

Svec, F. Porous Polymer Monoliths: Amazingly Wide Variety of Techniques Enabling Their Preparation. *J. Chromatogr. A* **2010**, *1217*, 902–924.

Svec, F.; Fréchet, J. M. J. Continuous Rods of Macroporous Polymer as High-Performance Liquid Chromatography Separation Media. *Anal. Chem.* **1992**, *64*, 820–822.

Svec, F.; Fréchet, J. M. J. Kinetic Control of Pore Formation in Macroporous Polymers. Formation of "Molded" Porous Materials with High Flow Characteristics for Separations or Catalysis. *Chem. Mater.* **1995**, *7*, 707–715.

Svec, F.; Lv, Y. Advances and Recent Trends in the Field of Monolithic Columns for Chromatography. *Anal. Chem.* **2015**, *87*, 250–273.

Taguchi, A.; Smätt, J. H.; Lindén, M. Carbon Monoliths Possessing a Hierarchical, Fully Interconnected Porosity. *Adv. Mater.* **2003**, *15*, 1209–1211.

Takenaka, M.; Hashimoto, T.; Dobashi, T. Tricontinuous Structure in a Homopolymer–Homopolymer–Random–Copolymer Ternary Mixture Quenched Under the Tricritical Point. *Phys. Rev. E* **1995**, *52*, 5142–5145.

Thommes, M.; Kaneko, K.; Neimark, A. V.; Olivier, J. P.; Rodriguez-Reinoso, F.; Rouquerol, J.; Sing, K. S. W. Physisorption of Gases, with Special Reference to the Evaluation of Surface Area and Pore Size Distribution. *Pure Appl. Chem.* **2015**, *87*, 1051–1069.

Thommes, M.; Cychosz, K. A.; Neimark, A. V. *Advanced Physical Adsorption Characterization of Nanoporous Carbons*, 1st ed.; Tascón, J., Ed.; Elsevier, **2012**.

Tselikas, Y.; Hadjichristidis, N.; Lescanec, R. L.; Honeker, C. C.; Wohlgemuth, M.; Thomas, E. L. Architecturally-Induced Tricontinuous Cubic Morphology in Compositionally Symmetric Miktoarm Starblock Copolymers. *Macromolecules* **1996**, *29*, 3390–3396.

Turson, M.; Zhou, M.; Jiang, P.; Dong, X. Monolithic Poly(ethylhexyl methacrylate-*co*-ethylene dimethacrylate) Column with Restricted Access Layers Prepared via Reversible Addition-Fragmentation Chain Transfer Polymerization. *J. Sep. Sci.* **2011**, *34*, 127–134.

Urban, J.; Jandera, P.; Schoenmakers, P. Preparation of Monolithic Columns with Target Mesopore-Size Distribution for Potential Use in Size-Exclusion Chromatography. *J. Chromatogr. A* **2007**, *1150*, 279–289.

Valkama, S.; Nykänen, A.; Kosonen, H.; Ramani, R.; Tuomisto, F.; Engelhardt, P.; Ten Brinke, G.; Ikkala, O.; Ruokolainen, J. Hierarchical Porosity in Self-Assembled Polymers: Post-Modification of Block Copolymer-Phenolic Resin Complexes by Pyrolysis Allows the Control of Micro- and Mesoporosity. *Adv. Funct. Mater.* **2007**, *17*, 183–190.

Viklund, C.; Nordström, A.; Irgum, K.; Svec, F.; Fréchet, J. M. J. Preparation of Porous Poly (styrene-*co*-divinylbenzene) Monoliths with Controlled Pore Size Distributions

Initiated by Stable Free Radicals and Their Pore Surface Functionalization by Grafting. *Macromolecules* **2001**, *34*, 4361–4369.

Viklund, C.; Svec, F.; Fréchet, J. M. J.; Irgum, K. Monolithic, "Molded", Porous Materials with High Flow Characteristics for Separations, Catalysis, or Solid-Phase Chemistry: Control of Porous Properties during Polymerization. *Chem. Mater.* **1996**, *8*, 744–750.

Wang, Z.; Li, F.; Ergang, N. S.; Stein, A. Effects of Hierarchical Architecture on Electronic and Mechanical Properties of Nanocast Monolithic Porous Carbons and Carbon-Carbon Nanocomposites. *Chem. Mater.* **2006**, *18*, 5543–5553.

Webb, P.A.; Orr, C. Analytical Methods in Fine Particle Technology, Micromeritics Instrument Corp., **1997**.

Weidman, J. L.; Mulvenna, R. A.; Boudouris, B. W.; Phillip, W. A. Unusually Stable Hysteresis in the pH-Response of Poly(acrylic acid) Brushes Confined within Nanoporous Block Polymer Thin Films. *J. Am. Chem. Soc.* **2016**, *138*, 7030–7039

Werner, J. G.; Scherer, M. R. J.; Steiner, U.; Wiesner, U. Gyroidal Mesoporous Multifunctional Nanocomposites via Atomic Layer Deposition. *Nanoscale* **2014**, *6*, 8736–8742.

Winey, K. I.; Thomas, E. L.; Fetters, L. J. Swelling a Lamellar Diblock Copolymer with Homopolymer: Influences of Homopolymer Concentration and Molecular Weight. *Macromolecules* **1991**, *24*, 6182–6188.

Wolf, J. H.; Hillmyer, M. A. Ordered Nanoporous Poly(cyclohexylethylene). *Langmuir* **2003**, *19*, 6553–6560.

Xie, S.; Allington, R. W.; Fréchet, J. M. J.; Svec, F. Porous Polymer Monoliths: An Alternative to Classical Beads. *Adv. Biochem. Eng. Biotechnol.* **2002**, *76*, 87–125.

Xie, Y.; Moreno, N.; Calo, V. M.; Cheng, H.; Hong, P.-Y.; Sougrat, R.; Behzad, A. R.; Tayouo, R.; Nunes, S. P. Synthesis of Highly Porous Poly(*tert*-butyl acrylate)-*b*-polysulfone-*b*-poly(*tert*-butyl acrylate) Asymmetric Membranes. *Polym. Chem.* **2016**, *7*, 3076–3089.

Yan, N.; Wang, Y. Reversible Switch between the Nanoporous and Nonporous State of Amphiphilic Block Copolymer Films Regulated by Selective Swelling. *Soft Matter* **2015**, *11*, 6927–6937.

Yang, S. Y.; Ryu, I.; Kim, H. Y.; Kim, J. K.; Jang, S. K.; Russell, T. P. Nanoporous Membranes with Ultrahigh Selectivity and Flux for the Filtration of Viruses. *Adv. Mater.* **2006**, *18*, 709–712.

Yang, X.; Chen, Y.; Wang, M.; Zhang, H.; Li, X.; Zhang, H. Phase Inversion: A Universal Method to Create High-Performance Porous Electrodes for Nanoparticle-Based Energy Storage Devices. *Adv. Funct. Mater.* **2016**, *26*, 8427–8434.

Yang, X.-Y.; Chen, L.-H.; Li, Y.; Rooke, J. C.; Sanchez, C.; Su, B.-L. Hierarchically Porous Materials: Synthesis Strategies and Structure Design. *Chem. Soc. Rev.* **2017**, *46*, 481–558.

Yu, C.; Davey, M. H.; Svec, F.; Fréchet, J. M. Monolithic Porous Polymer for On-Chip Solid-Phase Extraction and Preconcentration Prepared by Photoinitiated *in situ* Polymerization within a Microfluidic Device. *Anal. Chem.* **2001**, *73*, 5088–5096.

Zalusky, A. S.; Olayo-Valles, R.; Wolf, J. H.; Hillmyer, M. A. Ordered Nanoporous Polymers from Polystyrene-Polylactide Block Copolymers. *J. Am. Chem. Soc.* **2002**, *124*, 12761–12773.

Zhang, Q.; Gu, Y.; Li, Y. M.; Beaucage, P. A.; Kao, T.; Wiesner, U. Dynamically Responsive Multifunctional Asymmetric Triblock Terpolymer Membranes with Intrinsic Binding Sites for Covalent Molecule Attachment. *Chem. Mater.* **2016**, *28*, 3870–3876.

Zhang, Y.; Sargent, J. L.; Boudouris, B. W.; Phillip, W. A. Nanoporous Membranes Generated from Self-Assembled Block Polymer Precursors: *Quo Vadis*? *J. Appl. Polym. Sci.* **2015**, *132*, 41683.

Zhao, H.; Gu, W.; Sterner, E.; Russell, T. P.; Coughlin, E. B.; Theato, P. Highly Ordered Nanoporous Thin Films from Photocleavable Block Copolymers. *Macromolecules* **2011**, *44*, 6433–6440.

Zhou, N.; Bates, F. S.; Lodge, T. P. Mesoporous Membrane Templated by a Polymeric Bicontinuous Microemulsion. *Nano Lett.* **2006**, *6*, 2354–2357.

Appendix A. Nanoporous Polymer Monoliths with Functional Pore Walls

The use of block polymers in the synthesis of nanoporous materials affords a wide range of possibilities for tuning pore wall functionality through tailored block chemistries. A variety of techniques have been applied to tune pore wall chemistry including multiblock polymers,[1,2] polymer blends,[3,4] the incorporation of functional groups into the block junction,[5] and selective swelling with additives.[6–8] The strength of such approaches resides in the ability to tailor the density and chemistry of the functional groups which can be chosen for targeted applications in aqueous solutions.[9–13] Therefore, we focused our efforts on synthesizing mesoporous P(S-*co*-DVB) monoliths to which hydrophilic polymer chains were covalently attached at one end to the pore wall. Two approaches were taken: multiblock macro-CTAs (Appendix A.1) and blends of macro-CTAs (Appendix A.2). Preliminary results of applications of these materials are also described (Appendix B).

A.1 Multiblock Macro-CTAs

PLA-*b*-PI-CTA (synthesis described in Section 2.1.1.3) was used to copolymerize S and DVB (synthesis described in Section 2.1.2.1) to prepare PIMS monoliths, shown schematically in Figure A.1. As previously described, PLA was chosen as it readily selectively etches while PI was chosen as the second block because of the latent reactivity of the alkene units which permits post-polymerization modifications.[14] As the polymerization proceeded, the growing P(S-*co*-DVB) block microphase-separated from

the PLA-*b*-PI-CTA, and in situ cross-linking trapped a bicontinuous structure. The PLA block was then selectively etched in aqueous solutions of base to afford a mesoporous monolith with the PI block lining the pore walls of the P(S-*co*-DVB) matrix. Subsequent treatment of the monolith with *m*-chloroperoxybenzoic acid (*m*-CPBA) allowed for the controlled epoxidation of the PI block.[14] The addition of hydrophilic functional groups to the hydrophobic mechanically robust matrix increases the wettability of the monolith for applications in aqueous solutions (Section B.1). We show that for constant PLA molar mass ($M_{n,\,PLA}$ = 27 kg mol^{-1}) and varied PI molar mass ($M_{n,\,PI}$ = 1.4, 7, 15 kg mol^{-1}) we can tune the density of PI chains on the pore walls of the monolith, and thereby functional groups, while retaining the overall morphology and bicontinuous structure. Hereon in, monoliths are referred to as LI xx-yy where xx and yy denote the M_n of the PLA and PI blocks used to prepare the monoliths, respectively.

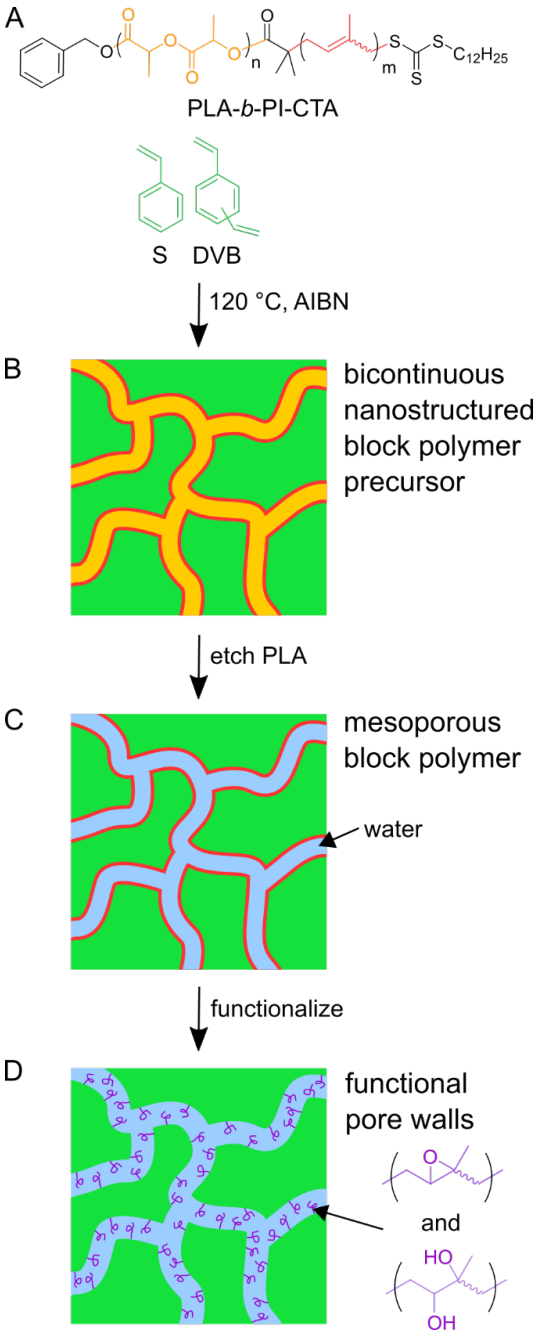

Figure A.1. Preparation of nanostructured block polymer monoliths. (a) PLA-*b*-PI-CTA is dissolved in styrene and DVB monomers to form a homogenous reaction mixture. (b) RAFT copolymerization of the monomers produces a bicontinuous PLA-*b*-PI-*b*-P(S-*co*-DVB) block polymer precursor. (c) Selective etching of PLA results in a mesoporous polymer monolith with PI lining the pore walls of the P(S-*co*-DVB) matrix. (d) The surface chemistry of the pore walls is further tailored through epoxidation of the PI alkene groups.

The thermal properties of the macro-CTAs (Figure A.2) and monoliths (Figure A.3) were characterized by differential scanning calorimetry (DSC). Except for the most asymmetric macro-CTA ($M_{n,\ PI}$ = 1.4) which exhibits a single glass transition (T_g), presumably due to the low volume fraction of PI, the macro-CTAs show two T_gs, at -62 and 49 °C, corresponding to PI and PLA, respectively.[15] An exotherm at temperatures > 140 °C is associated with cross-linking of PI, and is not observed upon subsequent cooling and re-heating. In the nanostructured monoliths, the T_g of the PI is no longer observed, possibly because the polymer chains are highly confined in the nanostructured monolith. Heating of hydroxyl-terminated PS-*b*-PI-*b*-PLA-OH in styrene monomer at 120 °C shows no change in the SEC trace of the block polymer (Figure A.4) which suggests that the PI does not react to an appreciable extent during styrene polymerization. The additional peak observed in SEC after heating is attributed to the formation of PS homopolymer due to the auto-polymerization of styrene.

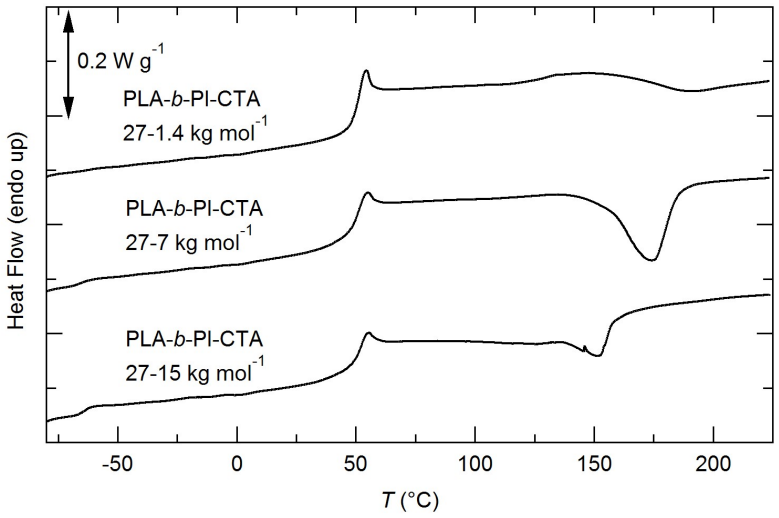

Figure A.2. DSC thermograms of the PLA-*b*-PI-CTA macro-CTA precursors on the second heating cycle. The T_gs at -62 and 49 °C correspond to the PI and PLA blocks, respectively, and the exotherm is attributed to the cross-linking of the PI. No T_g is observed for the lowest molar mass PI (1.4 kg mol^{-1}).

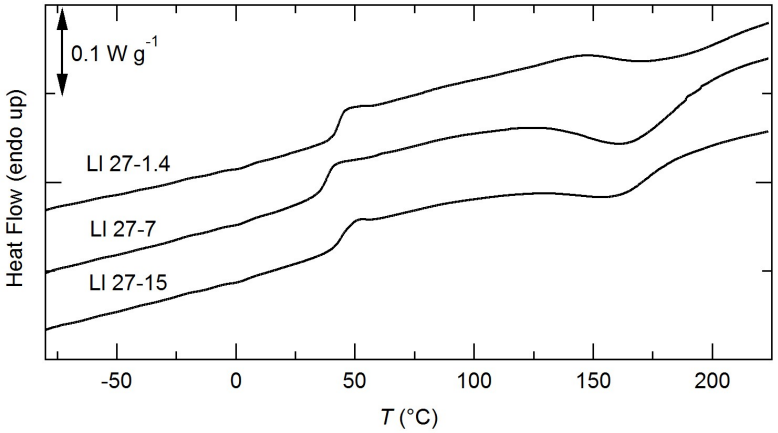

Figure A.3. DSC thermograms of a PLA-*b*-PI-*b*-P(S-*co*-DVB) nanostructured monoliths on the second heating cycle. A glass transition of the PLA block is observed, and the exotherm is attributed to the cross-linking of PI.

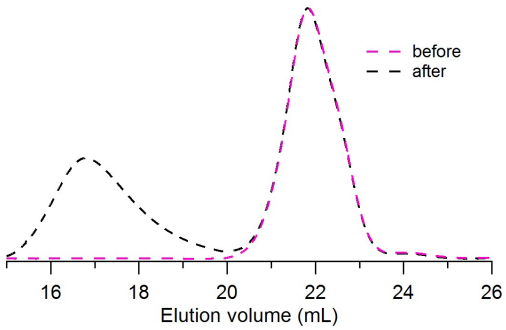

Figure A.4. SEC traces (RI detector) in $CHCl_3$ of PS-*b*-PI-*b*-PLA-OH before and after heating in styrene monomer at 120 °C. The peak associated with the triblock polymer does not change upon heating; the additional peak that develops is attributed to PS homopolymer.

Small-angle X-ray scattering (SAXS) profiles indicate compositional heterogeneities present in the polymer monoliths both before and after etching (Figure A.5). The single broad scattering peak is typical of disordered microphase-separated block polymers, and the increase in scattering intensity after etching is consistent with the increased electron

density contrast of the pores with the polymer matrix. As the molar mass of the PI block increases the position of the scattering peak shifts slightly towards larger wavevector $q^* = 0.14 – 0.18$ nm^{-1} which corresponds to the formation of smaller domains, $d = 35 – 45$ nm.

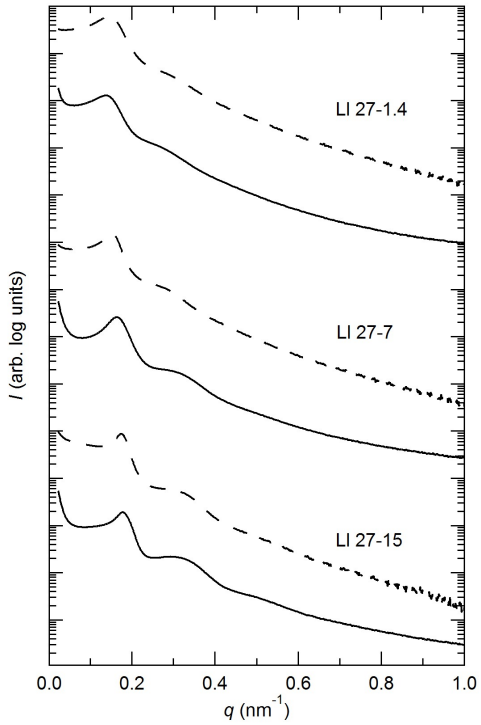

Figure A.5. SAXS patterns of the nanostructured block polymer precursors (solid lines) and the corresponding nanoporous polymers (dashed lines). The increased scattering intensity after etching is consistent with the increased electron density contrast of the pores with the polymer matrix. The data are arbitrarily shifted between samples, but the relative intensities before and after etching a sample are maintained.

The mesoporous monoliths were imaged using scanning electron microscopy (SEM) where the gray regions are the PI-*b*-P(S-*co*-DVB) matrix and the dark regions are the mesopores (Figures A.6 top and A.7). Qualitatively, the morphology is independent of PI molar mass and a bicontinuous structure is attained in all cases. Quantitatively, the porosity was characterized using nitrogen sorption measurements which gave type IV

isotherms with H2 hysteresis, consistent with the formation of a disordered network structure (Figure A.8).[16] Mesopore size distributions were estimated using quenched solid density functional theory and are largely independent of the PI molar mass, with all compositions having average pore sizes of 14 nm (Figure A.6 bottom).[17] The BET specific surface areas are 105, 99, and 79 m^2 g^{-1} and total pore volumes are 0.38, 0.38, and 0.29 mL g^{-1} for LI 27-1.4, LI 27-7, and LI 27-15, respectively.[18] As expected, the pore size, which most strongly depends on the molar mass of PLA, is largely invariant across the compositions studied, and the pore volumes and surfaces areas decrease with decreasing PLA content. The incorporation of PI onto the pore walls of the monolith has negligible effect on the elastic modulus when compared to monoliths without PI (both on the order of 1 GPa), which implies that the primary contribution to the modulus is the cross-linked PS matrix. The incorporation of PI onto the pore walls of the monolith does provide a modest increase in toughness compared to monoliths that do not contain PI (900 ± 140 from 510 ± 220 kJ m^{-3}, standard deviations reported for 3 samples) (Figure A.9).

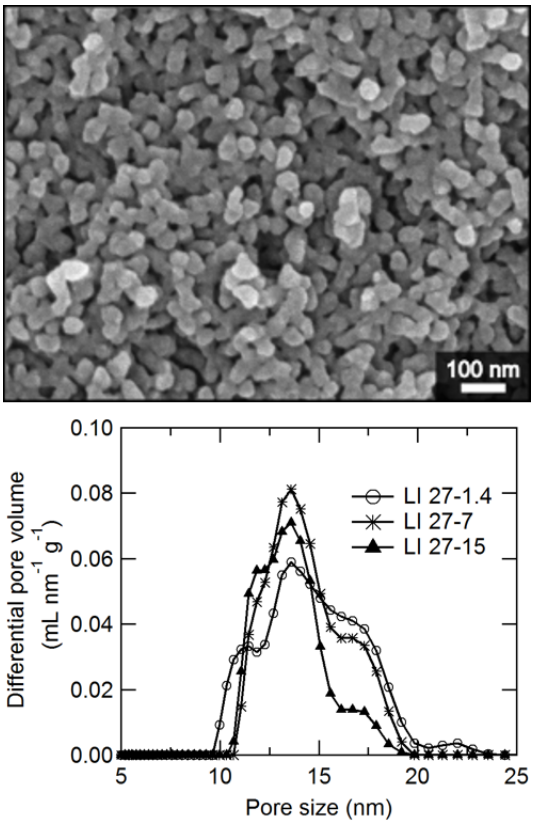

Figure A.6. Nanoporous polymer monolith characterization after etching of PLA. Top: Representative SEM micrograph of mesoporous PI-*b*-P(S-*co*-DVB) derived from LI 27-1.4 after coating with ca. 3 nm Pt. Bottom: Mesopore size distributions based on QSDFT.

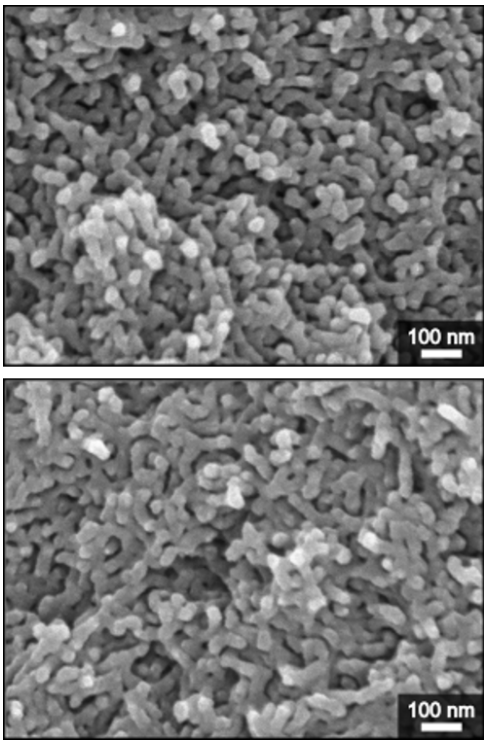

Figure A.7. SEM micrographs of PI-*b*-P(S-*co*-DVB) mesoporous monoliths derived from LI 27-7 (top) and LI 27-15 (bottom) after coating with ca. 3 nm Pt.

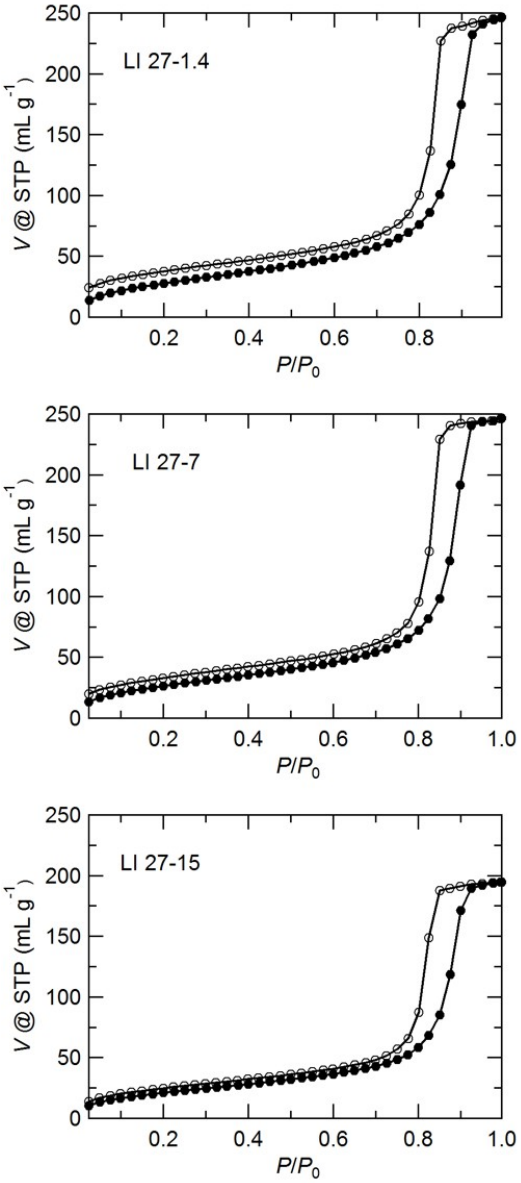

Figure A.8. Nitrogen sorption isotherms of the mesoporous PI-*b*-P(S-*co*-DVB) monoliths. Filled circles indicate adsorption, empty circles indicate desorption.

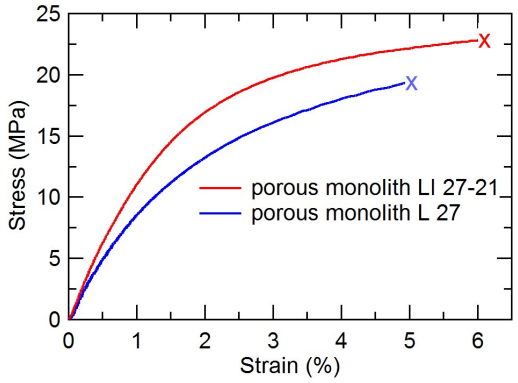

Figure A.9. Representative stress-strain curves for mesoporous monoliths with (LI 27-15) and without (L 27) PI lining the pore walls. Samples were extended at a rate of 1 mm min^{-1}.

Due to the cross-linked nature of the monoliths, it is challenging to directly characterize the polymer chains on the pore walls after monolith synthesis or post-polymerization modifications. In some cases FTIR, X-ray photoelectron spectroscopy, or titration may provide qualitative or quantitative evidence.[19] For this system, based on results from a similar study in which PS-*b*-PI-*b*-PLA self-assembled to form cylindrical PLA core domains surrounded by PI shells in a PS matrix, we expect that ca. 75% of the PI is epoxidized, likely due to the limited accessibility of the alkene groups near the interface of PI-*b*-P(S-*co*-DVB).[14] These results corroborated well with the sample composition determined by elemental analysis (Table A.1) and the monoliths were then tested as the frits in reference electrodes (Appendix B).

Table A.1. Calculated and measured carbon and hydrogen elemental analysis for a monolith derived from a PLA-*b*-PI-CTA ($M_{n,\,PLA}$ = 27 kg mol^{-1}, $M_{n,\,PI}$ = 7 kg mol^{-1}).

	Calculated (wt%)		Measured (wt%)	
	C	H	C	H
Nanostructured precursor	81.2	7.5	79.2 ± 0.2	7.3 ± 0.1
Mesoporous monolith	91.7	8.1	90.3 ± 0.4	8.1 ± 0.2
Epoxidized monolith	90.3[a]	8.0[a]	88.3 ± 0.4	7.6 ± 0.1

[a]Assumes 75% epoxidation of PI. Averages and standard deviations are reported for three samples.

A.2 Blends of Macro-CTAs

As an alternative to using multi-block macro-CTAs, monoliths with functional pore walls were prepared through copolymerization of S and DVB from blends of macro-CTAs. The macro-CTAs are chosen such that one can be selectively etched and the other provides some desired functionality e.g. hydrophilicity. The main advantage of this strategy is that it allows for the screening of materials with a wide range of functional group densities on the pore walls by simple variations in the initial blend composition. However, the approach is limited by the miscibility of the two macro-CTAs, which is a requirement for forming a single composite domain such that upon etching the remaining macro-CTA partially occupies the pore space. Immiscibility often results in macroscopically phase separated structures or, under the right conditions, tricontinuous structures (Chapter 5). With the choice of PLA-CTA as the selectively etchable block, we synthesized monoliths from blends of PLA-CTA with PEO-CTA or poly(dimethylacrylamide)-CTA (PDMA-CTA), which were prepared by previously reported syntheses and are miscible with PLA.[20,21] Specifically, PEO-CTA of M_w = 2, 20, and 41 kg mo1^{-1} and PDMA-CTA of M_w = 31 kg mol^{-1} were studied. At 68 wt% S/DVB (4/1 molar), mesoporous bicontinuous monoliths were produced over the ranges of 20 – 32 wt% PLA-CTA, where the remainder was PEO-CTA or PDMA-CTA. In a typical case, nitrogen sorption analysis indicated specific surface areas between 90 – 150 m^2 g^{-1}, depending on the initial composition. At lower PLA contents either the domains were discontinuous or there was pore collapse upon etching. In the former, the PLA could not be etched completely, as determined by gravimetric analysis. In the latter, the PLA was etched completely

however the monoliths exhibited negligible specific surface areas. The bicontinuous mesoporous monoliths were then tested in aqueous solution as reference electrodes (Appendix B) as the hydrophilic PEO or PDMA facilitated wetting of the pores of the monolith.

A.3 References

1) Rzayev, J.; Hillmyer, M. A. Nanochannel Array Plastics with Tailored Surface Chemistry. *J. Am. Chem. Soc.* **2005**, *127*, 13373–13379.

2) Zhang, Q.; Gu, Y.; Li, Y. M.; Beaucage, P. A.; Kao, T.; Wiesner, U. Dynamically Responsive Multifunctional Asymmetric Triblock Terpolymer Membranes with Intrinsic Binding Sites for Covalent Molecule Attachment. *Chem. Mater.* **2016**, *28*, 3870–3876.

3) Mao, H.; Arrechea, P. L.; Bailey, T. S.; Johnson, B. J. S.; Hillmyer, M. A. Control of Pore Hydrophilicity in Ordered Nanoporous Polystyrene Using an AB/AC Block Copolymer Blending Strategy. *Faraday Discuss.* **2005**, *128*, 149–162.

4) Radjabian, M.; Abetz, V. Tailored Pore Sizes in Integral Asymmetric Membranes Formed by Blends of Block Copolymers. *Adv. Mater.* **2015**, *27*, 352–355.

5) Schumers, J.-M.; Vlad, A.; Huynen, I.; Gohy, J.-F.; Fustin, C.-A. Functionalized Nanoporous Thin Films from Photocleavable Block Copolymers. *Macromol. Rapid Commun.* **2012**, *33*, 199–205.

6) Gu, Y.; Wiesner, U. Tailoring Pore Size of Graded Mesoporous Block Copolymer Membranes: Moving from Ultrafiltration toward Nanofiltration. *Macromolecules* **2015**, *48*, 6153–6159.

7) Shinkai, T.; Sugiyama, K.; Ito, K.; Yokoyama, H. Nanoporous Fabrication of Block Copolymers via Carbon Dioxide Swelling: Difference between CO_2-Swollen and Nanoporous Block Copolymers. *Polymer.* **2016**, *100*, 19–27.

8) Chen, X. C.; Kortright, J. B.; Balsara, N. P. Water Uptake and Proton Conductivity in Porous Block Copolymer Electrolyte Membranes. *Macromolecules* **2015**, *48*, 5648–5655.

9) Xie, Y.; Moreno, N.; Calo, V. M.; Cheng, H.; Hong, P.-Y.; Sougrat, R.; Behzad, A. R.; Tayouo, R.; Nunes, S. P. Synthesis of Highly Porous Poly(*tert*-butyl acrylate)-*b*-Polysulfone-*b*-Poly(*tert*-butyl acrylate) Asymmetric Membranes. *Polym. Chem.* **2016**, *7*, 3076–3089.

10) Weidman, J. L.; Mulvenna, R. A.; Boudouris, B. W.; Phillip, W. A. Unusually Stable Hysteresis in the pH-Response of Poly(Acrylic Acid) Brushes Confined within Nanoporous Block Polymer Thin Films. *J. Am. Chem. Soc.* **2016**, *138*, 7030–7039.

11) Gruber, M. F.; Schulte, L.; Ndoni, S. Nanoporous Materials Modified with Biodegradable Polymers as Models for Drug Delivery Applications. *J. Colloid Interface Sci.* **2013**, *395*, 58–63.

12) Ahn, H.; Park, S.; Kim, S.; Yoo, P. J.; Ryu, D. Y.; Russell, T. P. Nanoporous Block Copolymer Membranes for Ultrafiltration: A Simple Approach to Size Tunability. *ACS Nano* **2014**, *8*, 11745–11752.

13) Yan, N.; Wang, Y. Reversible Switch between the Nanoporous and Nonporous State of Amphiphilic Block Copolymer Films Regulated by Selective Swelling. *Soft Matter* **2015**, *11*, 6927–6937.

14) Bailey, T. S.; Rzayev, J.; Hillmyer, M. A. Routes to Alkene and Epoxide Functionalized Nanoporous Materials from Poly(styrene-*b*-isoprene-*b*-lactide) Triblock Copolymers. *Macromolecules* **2006**, *39*, 8772–8781.

15) Angelo, R. J.; Ikeda, R. M.; Wallach, M. L. Multiple Glass Transitions of Block Polymers. *Polymer.* **1965**, *6*, 141–156.

16) Lowell, S.; Shields, J. E.; Thomas, M. A.; Thommes, M. *Characterization of Porous Solids and Powders: Surface Area, Pore Size and Density*; Scarlett, B., Ed.; Kluwer Academic Publishers: Norwell, MA, **2004**.

17) Gor, G. Y.; Thommes, M.; Cychosz, K. a.; Neimark, A. V. Quenched Solid Density Functional Theory Method for Characterization of Mesoporous Carbons by Nitrogen Adsorption. *Carbon.* **2012**, *50*, 1583–1590.

18) Brunauer, S.; Emmett, P. H.; Teller, E. Adsorption of Gases in Multimolecular Layers. *J. Am. Chem. Soc.* **1938**, *60*, 309–319.

19) Fierke, M. A. The Utilization of Templated Porous Electrodes in Electrochemical Applications, University of Minnesota, **2013**.

20) Schulze, M. W.; McIntosh, L. D.; Hillmyer, M. A.; Lodge, T. P. High-Modulus, High-Conductivity Nanostructured Polymer Electrolyte Membranes via Polymerization-Induced Phase Separation. *Nano Lett.* **2014**, *14*, 122–126.

21) Nasiri, M.; Bertrand, A.; Reineke, T. M.; Hillmyer, M. A. Polymeric Nanocylinders by Combining Block Copolymer Self-Assembly and Nanoskiving. *ACS Appl. Mater. Interfaces* **2014**, *6*, 16283–16288.

Appendix B. Application of Nanoporous Polymer Monoliths

B.1 Implementation of Nanoporous Polymer Monoliths as Reference Electrodes

The work in this section was done as a collaborative effort. Professor Philippe Bühlmann, Dr. Maral Mousavi, and Evan Anderson at UMN provided expertise in electrochemisty techniques, and Maral and Evan performed the electrochemical measurements.

Reference electrodes are necessary for the vast majority of electrochemical techniques.[1] These electrodes should provide a stable and reproducible reference potential, regardless of the sample solution. The electrodes are often built using a nanoporous frit filled with electrolyte, where the nanoporous material serves to separate the sample and reference solutions. The purpose of the frit is to minimize mixing of the two solutions while maintaining electrical contact (Figure B.1). Nanoporous glass frits, with pore size ca. 10 nm and, more recently, nanoporous polymers with pore size ca. 1 μm, are often used for this purpose.[2] However, use of the former can introduce errors in many measurements due to electrostatic screening effects caused by the surface charge density on the pore wall of the glass, while the latter is not suitable for long-term measurements as the large pore sizes allow for more rapid mixing and contamination of the sample and reference solution.[2,3]

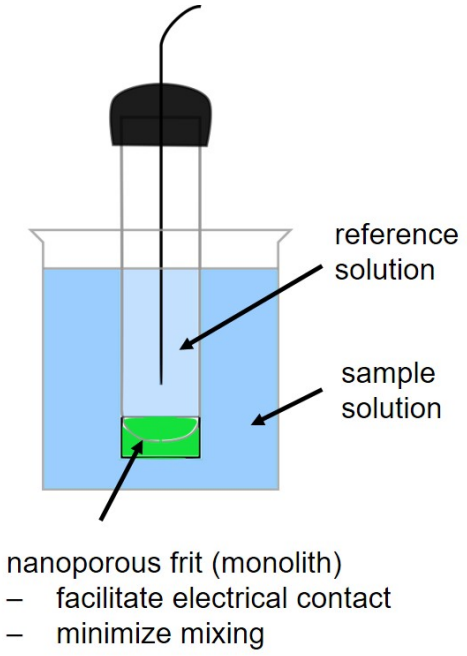

Figure B.1. Cartoon of the reference electrode.

In attempts to reduce these undesirable sample-dependent potentials we tested the polymer monoliths described in Appendix A as the reference electrode frit material, using a previously reported technique.[2] The dependence of the potential of the reference electrode is measured in aqueous solutions of KCl, $CaCl_2$, Na_2SO_4, and tetrabutylammonium chloride (TBACl) as well as at varying pH. The former describes the electromotive force (emf) response to ions of various size and charge, while the later reflects changes in acidity.

Even with hydrophilic pore walls, especially at low densities of hydrophilic functional groups, the air-filled pores of dried monoliths did not always readily wet with aqueous solution (determined by impedance spectroscopy). Therefore, prior to testing, the

monoliths were either pre-wet in ethanol or were stored in water after PLA etching (without drying). Even at low concentrations of PEO or PDMA on the pore walls, there were still specific interactions between the electrolyte and polymer chains which resulted in emf changes comparable to the commercially available nanoporous glasses. The monoliths with epoxidized PI on the pore walls resulted in the smallest emf changes and are summarized below.

Using impedance spectroscopy, the resistances of the monoliths derived from LI 27-1.6, 27-7, and 27-13 were measured as 700 ± 200, 700 ± 100, and 630 ± 40 Ω, respectively. While these resistances are greater than nanoporous glass frits (< 150 Ω), they are not so large as to prevent electrical transport through the pores and the values are comparable to commercially available polyethylene and Teflon frits, which have pore sizes that are three orders of magnitude larger.[2] Furthermore, the small pore size of the frits prepared via PIMS minimizes the flow rate of solution out of the frit thereby decreasing the likelihood of sample and reference solution mixing. Specifically, the epoxidized monoliths have flow rates of 0.007 ± 0.003 μL h^{-1}, which is greater than that of the commercially available nanoporous glasses, Vycor and CoralPor (0.00002 μL h^{-1} and 0.00001 μL h^{-1}). The polyol chains effectively decrease the pore radius in aqueous solution thus decreasing the flow rate.[4] For comparison, mesoporous P(S-*co*-DVB) monoliths without the epoxidized PI attached to the pore walls, but with a comparable dry-state pore size, have much higher flow rates of 0.06 ± 0.05 μL h^{-1}. The large standard

deviations in these samples may be due to some de-wetting of the pores over the long term measurement.

The monoliths were then tested in various aqueous solutions. Over a range of electrolyte concentrations, the emf response of the epoxidized monolith derived from LI 27-7 varies by ca. 40 mV (Figure B.2). While this change is less than the nanoporous glasses (ca. 70 mV), it still does not achieve the desirable sample independent response.[2] Varying the molar mass of the PI block had negligible effect on the emf response (Figure B.3). The response was the same for both electrolyte addition and dilution, thus the changing emf response is likely due to interactions of the ions with the epoxidized PI. Similarly, when the pH is varied a smaller change in emf is observed (ca. 15 mV compared to ca. 40 mV for nanoporous glasses), but the response is still not completely sample independent (Figure B.4).

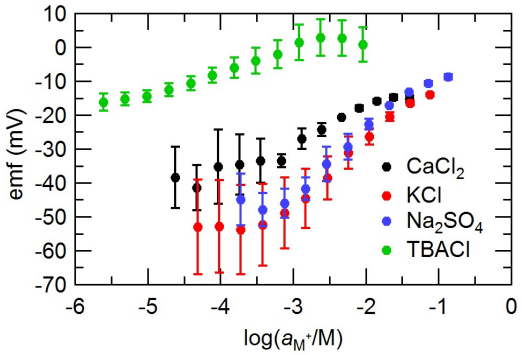

Figure B.2. Effect of various electrolytes and concentrations on the emf response of a monolith derived from LI 27-7. Error bars indicate standard deviations based on three samples.

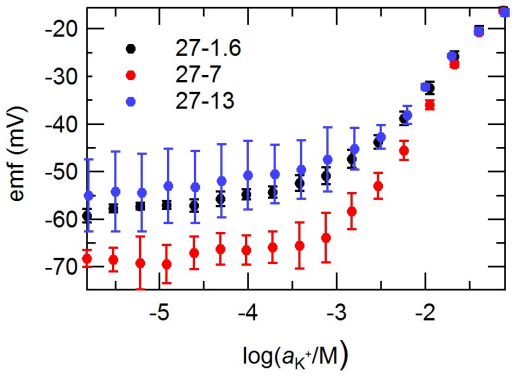

Figure B.3. Effect of PI molar mass on emf response to varying KCl concentration. Similarly, the other electrolytes studied showed no discernable molar mass dependence of the emf response. Error bars indicate standard deviations based on three samples.

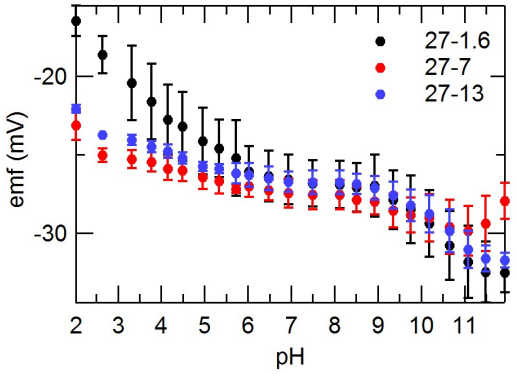

Figure B.4. Dependence of the potential on pH of monoliths with different PI molar masses with a 10 mM NaCl background.

The morphology and flow rates through the functional polymer monoliths are comparable to the commercially available nanoporous glasses, and the electrical resistances are low enough to permit transport, however the sample independent response has not been achieved. Likely, a polymer monolith with a similar chemistry to the monoliths presented here, but with pore sizes closer to 20 – 40 nm would be beneficial. This is expected to minimize ion-polymer interactions while retaining the benefits of small pores.

We also investigated the performance of mesoporous P(S-*co*-DVB) as the reference electrode, which was prepared by the etching of nanostructured PLA-*b*-P(S-co-DVB) with two different RAFT agents. When the RAFT agent was DDMAT (as shown elsewhere in this thesis) hydrolytic etching of the PLA block produced monoliths which should have carboxylic acid groups on the pore walls. Alternatively, when the RAFT agent was 2-(benzylsulfanylthiocarbonylsulfanyl)ethanol, hydrolytic etching of PLA block should result in monoliths with hydroxyl groups on the pore walls.[5] We hypothesized that the latter would be more hydrophilic and therefore the pores would be more easily wetted. In principle, there should be minimal interactions of ions in this system as, unlike the previously described systems, there are no swollen polymer chains occupying the pore and there is no surface charge on the pore walls unlike in the nanoporous glasses. However, the emf of these monoliths was highly inconsistent across samples, and was not pursued further.

B.2 Synthesis of Polymer Monoliths in Capillaries

Similar to the monoliths prepared via PIPS, the monoliths prepared via PIMS obtain the shape of the container used for polymerization. Traditionally, technological applications of macroporous PIPS monoliths take advantage of this property by the direct preparation of the monolith in capillaries such that no further processing is required. By attaching the capillary to a pump these monoliths have been widely applied as the stationary phase in chromatography.[6] In this preparative method, the inner surface of the capillary is pre-

treated to place reactive vinyl groups on the walls. This permits covalent attachment of the monolith to the column because as the monomers copolymerize they also react with the vinyl groups on the capillary. Thus, after attaching to a pump for use in a chromatographic separation, the mobile phase then flows through the pores of the monolith, rather than around it (i.e. avoids channeling).

With the successful technological application of PIPS monoliths as an example, we attempted a similar in situ synthesis and with the goal of using the hierarchically porous monoliths described in Chapter 3 as the stationary phase in chromatography. Specifically, 450 μm inner diameter fused silica capillaries were pre-treated with 3-(trimethoxysilyl)propyl methacrylate according to a literature procedure to yield vinyl groups on the pore walls of the capillary.[7] The main difficulty was that filling of the capillary with the PIMS reaction mixture of PLA-CTA/S/DVB/PEO-OH was incomplete, primarily due to the high viscosity of the mixture. The viscosity of PIMS mixtures are inherently greater than the traditional mixtures used in PIPS because of the high dissolved polymer content and, in the case of the hierarchically porous polymers, the semi-crystallinity of the PEO. Diluting the reaction mixture with 30 vol% dioxane had no apparent effect on the pore structure, but still only resulted in partial filling of the capillary (Figure B.5). Presumably, the viscosity of the mixture was still too high to permit complete filling and facilitate polymerization from the walls of the capillary. Using a column with a larger inner diameter would likely remedy some of the difficulties associated with filling a capillary. However, the scaling of PIPS reaction mixtures to

columns has encountered challenges with larger temperature gradients during polymerization, due to the exothermic nature of the polymerization, which leads to structural inhomogeneity in these materials.[8] The impact of scale-up on the morphology of PIMS monoliths has not been directly studied but the possible morphological consequences of the exotherm should be considered. From a technological standpoint, this strategy would also require larger volumes of material.

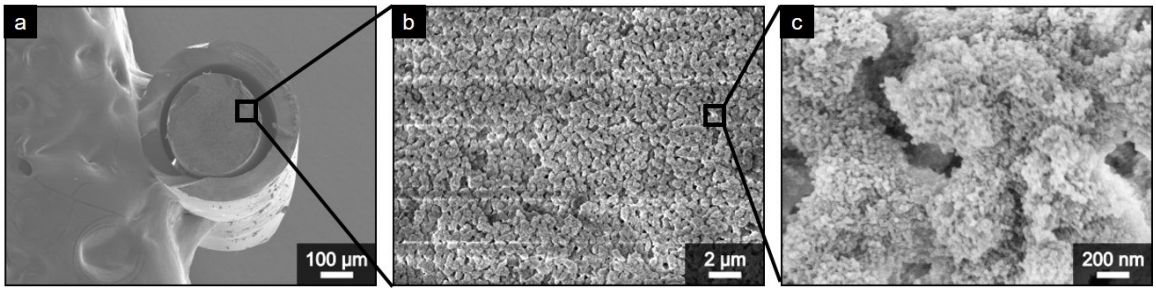

Figure B.5. SEM micrograph of monoliths prepared in capillaries. (a) Top view of monolith in capillary. (b,c) High magnification images of monolith.

B.3 References

1) Brett, C. M. A.; Brett, A. M. O. *Electrochemistry Principles, Methods, and Applications*; Oxford University Press: New York, NY, **1993**.

2) Mousavi, M. P. S.; Saba, S. A.; Anderson, E. L.; Hillmyer, M. A.; Bühlmann, P. Avoiding Errors in Electrochemical Measurements: Effect of Frit Material on the Performance of Reference Electrodes with Porous Frit Junctions. *Anal. Chem.* **2016**, *88*, 8706–8713.

3) Mousavi, M. P. S.; Bühlmann, P. Reference Electrodes with Salt Bridges Contained in Nanoporous Glass: An Underappreciated Source of Error. *Anal. Chem.* **2013**, *85*, 8895–8901.

4) He, D.; Ulbricht, M. Tailored "Grafting-From" Functionalization of Microfiltration Membrane Surface Photo-Initiated by Immobilized Iniferter. *Macromol. Chem. Phys.* **2009**, *210*, 1149–1158.

5) Seo, M.; Murphy, C. J.; Hillmyer, M. A. One-Step Synthesis of Cross-Linked Block Polymer Precursor to a Nanoporous Thermoset. *ACS Macro Lett.* **2013**, *2*, 617–620.

6) Svec, F.; Lv, Y. Advances and Recent Trends in the Field of Monolithic Columns for Chromatography. *Anal. Chem.* **2015**, *87*, 250–273.

7) Peterson, D. S.; Rohr, T.; Svec, F.; Fréchet, J. M. J. Dual-Function Microanalytical Device by In Situ Photolithographic Grafting of Porous Polymer Monolith: Integrating Solid-Phase Extraction and Enzymatic Digestion for Peptide Mass Mapping. *Anal. Chem.* **2003**, *75*, 5328–5335.

8) Peters, E. C.; Svec, F.; Fréchet, J. M. J. Preparation of Large-Diameter "Molded" Porous Polymer Monoliths and the Control of Pore Structure Homogeneity. *Chem. Mater.* **1997**, *9*, 1898–1902.

Appendix C. Outlook

To date, the majority of the property studies on PIMS monoliths have been on monoliths prepared in sealed glass vials. Translating these materials to polymerizations conducted in molds for technological applications has not yet been fully developed. Three main challenges have been limiting thus far: monomer volatility, reaction mixture viscosity, and reaction mixture miscibility. The first, monomer volatility, requires that the polymerization be conducted in a sealed vessel. While there is some compositional tolerance for monomer evaporation, if the monomers evaporate appreciably before polymerization a nanostructured monolith will not be formed. The second, reaction mixture viscosity can limit the ability to fill a mold with the precursor solution if the solution does not flow at room temperature. The third, reaction mixture miscibility, is limiting because many of the PIMS reaction mixtures that have been well-studied and have interesting properties when prepared in glass vials, do not form homogenous solutions at room temperature. This accelerates monomer evaporation during mold filling with a heated solution, or can make it impossible to fill a mold and retain solution homogeneity.

The commercial availability, well-established polymerization kinetics, and high T_g of S and DVB make them natural choices for the matrix block of nanoporous polymer monoliths, however to further expand the versatility of PIMS and address remaining processing challenges, the copolymerization of alternative, especially non-styrenic, monomers is a promising route. This could include the investigation of higher boiling

point monomers, and but also monomers with faster polymerization kinetics. Faster polymerizations are not only more technologically relevant but may also permit nanostructure formation prior to evaporation and may ease the requirement of a sealed polymerization vessel, or allow for lower reaction temperatures. For applications requiring large thin nanostructured disks, the incorporation of a tough rubbery domain into the matrix, not just on the pore walls, could provide opportunities that have thus far been inaccessible with brittle P(S-*co*-DVB). For the preparation of reference electrodes, monoliths with pore sizes closer to 20 – 40 nm would be advantageous to minimizing polymer-ion interactions and solution mixing.